Petrological and geochronological constraints on lower crust exhumation during Paleoproterozoic (Eburnean) orogeny, NW Ghana, West African craton

S Block, J Ganne, L Baratoux, Armin Zeh, Luis A Parra-Avila, M Jessell, L Ailleres, L Siebenaller

Petrological and geochronological constraints on lower crust exhumation during Paleoproterozoic (Eburnean) orogeny, NW Ghana, West African craton.

S. Block[1*], J. Ganne[1], L. Baratoux[1, 2], A. Zeh[3], L. A. Parra-Avila[4], M. Jessell[4], L. Ailleres[5], L. Siebenaller[1]

[1] Geosciences Environnement Toulouse, Observatoire Midi Pyrénées, IRD, 14 ave E. Belin, 31400, Toulouse, France.

[2] IFAN, Cheikh Anta Diop, Dakar, Senegal

[3] Institut für Geowissenschaften, Altenhöfer Allee 1, D-60438 Frankfurt am Main, Germany.

[4] Center for Exploration Targeting, The University of Western Australia, 35 Stirling Highway, Crawley, Perth, Western Australia 6009

[5] Monash University, School of Geosciences, Wellington Road, Clayton, Vic 3800, Australia

*Corresponding autor: sylvain.block@gmail.com

Note: This document is the author version of an article published in Journal of Metamorphic Geology, vol 33, issue 5, pp 463-494, June 2015 (DOI: 10.1111/jmg.12129)

ABSTRACT

We present new petrological and geochronological data on high-grade ortho- and paragneisses from north-western Ghana, forming part of the Paleoproterozoic (2.25-2.00 Ga) West African Craton. The study area is located in the interference zone between N-S and NE-SW trending craton-scale shear zones, formed during the Eburnean orogeny (2.15-2.00 Ga). High-grade metamorphic domains are separated from low-grade greenstone belts by high-strain zones, including early thrusts, extensional detachments and late-stage strike-slip shear zones. Paragneisses sporadically preserve high-pressure, low-temperature (HP-LT) relics, formed at the transition between the blueschist facies and the epidote-amphibolite sub-facies (10.0-14.0 kbar, 520-600°C), and represent a low (~15°C km^{-1}) apparent geothermal gradient. Migmatites record metamorphic conditions at the amphibolite-granulite facies transition. They reveal a clockwise pressure-temperature-time (*P–T–t*) path characterised by melting at pressures over 10.0 kbar, followed by decompression and heating to peak temperatures of 750°C at 5.0-8.0 kbar, which fit a 30°C km^{-1} apparent geotherm. A regional amphibolite-facies metamorphic overprint is recorded by rocks that followed a clockwise *P–T–t* path, characterised by peak metamorphic conditions of 7.0-10.0 kbar at 550-680°C, which match a 20-25°C km^{-1} apparent geotherm. These *P–T* conditions were reached after prograde burial and heating for some rock units, and after decompression and heating for others. The

timing of anatexis and of the amphibolite-facies metamorphic overprint is constrained by *in-situ* U-Pb dating of monazite crystallisation at 2138±7 and 2130±7 Ma respectively. The new dataset challenges the interpretation that metamorphic breaks in the West African Craton are due to diachronous Birimian "basins" overlying a gneissic basement. It suggests that the lower crust was exhumed along reverse, normal and transcurrent shear zones and juxtaposed against shallow crustal slices during the Eburnean orogeny. The craton in NW Ghana is made of distinct fragments with contrasting tectono-metamorphic histories. The range of metamorphic conditions and the sharp lateral metamorphic gradients are inconsistent with "hot orogeny" models proposed for many Precambrian provinces. These findings shed new light on the geodynamic setting of craton assembly and stabilisation in the Paleoproterozoic. It is suggested that the metamorphic record of the West African Craton is characteristic of Paleoproterozoic plate tectonics and illustrates a transition between Archean and Phanerozoic orogens.

Keywords: Paleoproterozoic, West African Craton, Exhumation, Anatectic dome, Collision

INTRODUCTION

Precambrian accretionary orogens provided significant contribution to the Earth's crustal growth due to high juvenile crust production rates, and high degrees of preservation of the newly formed crust through assembly against older cratonic nuclei (e.g. Condie, 1998; Cawood *et al.*, 2009). The Precambrian crust was mainly generated by successive pulses of juvenile magmas during a prolonged tectono-magmatic evolution, as is reflected by a wide range of overlapping geochronological data (e.g. Karlstrom *et al.*, 2001; Väisänen *et al.*, 2001; Zeh *et al.*, 2013 and references therein). The final stages of the evolution of Precambrian accretionary orogens are characterised by tectonic accretion of various units to form stable cratons. Maturing and cratonization of the crust is reflected by changing tectonic styles (e.g. Vanderhaeghe *et al.*, 1998), an increasing contribution of crustal reworking during magmatic activity (e.g. Martin *et al.*, 2005; Laurent *et al.*, 2011, 2014) and distinctive metamorphic overprints (e.g. Pitra *et al.*, 2010).

Precambrian accretionary orogens commonly include large proportions of fertile juvenile crust, and show high apparent geothermal gradients. Consequently, the lithosphere was rheologically weak and a partially molten orogenic lower crust was maintained for relatively long periods. According to some authors, the hot and weak crust accommodated regional shortening by homogeneous, distributed thickening and flow of partially molten rocks (Cagnard *et al.*, 2006; Chardon *et al.*, 2008, 2009). Precambrian accretionary orogens often comprise vast domains revealing isobaric metamorphic

conditions, with isotherms running parallel to the exposed surface, except for temperature anomalies linked to pluton emplacement (e.g. Debat *et al.*, 2003; Vidal *et al.*, 2009). The relative scarcity of strong lateral metamorphic gradients is assumed to result from homogeneous uplift of the entire metamorphic terrane, as opposed to a structurally controlled differential exhumation (Percival *et al.*, 1992; Percival & Skulski, 2000; Cagnard *et al.*, 2007; Gapais *et al.*, 2008; 2009). However, spatial variations in geothermal gradients and contrasting metamorphic grades between domains of similar ages have been reported in some Precambrian orogens (Stevens & Moyen, 2007, Ganne *et al.*, 2012, Block *et al.*, 2013). These findings indicate that the thermal regime can change in space and time during the evolution of ancient orogens, that exhumation localised by high-strain zones may be viable, and suggest the existence of non-unique tectonic settings.

The secular evolution of the global metamorphic record is reviewed by Brown (2007, 2009). Major changes are documented in metamorphic belts between the Neoarchean and the Paleoproterozoic eons. Most Archean metamorphic terranes display "ordinary" metamorphic *P–T* conditions and geothermal gradients (Komiya *et al.*, 2002). Contrastingly, Paleoproterozoic belts, including many collisional belts formed at 2.10-1.80 Ga during the inferred Paleoproterozoic supercontinent assembly (Zhao *et al*., 2002), are characterised by paired Eclogite – High-Pressure Granulite and Ultra-High Temperature metamorphism. This dual metamorphic record is interpreted as the hallmark of a "plate tectonics" geodynamic setting (Brown, 2007, 2009). The Paleoproterozoic West African Craton is considered as one of the youngest 'Archean-type' continental fragments. It is a vast (3.10^6 km^2) juvenile continental domain extracted from the mantle between 2.50 and 2.20 Ga Ga (Abouchami *et al.*, 1990; Boher *et al*., 1992; Gasquet *et al*., 2003, Peucat *et al*., 2005), and subsequently accreted against an older Archean nucleus during the 2.15-2.07 Ga Eburnean orogeny (Bonhomme, 1962; Milési *et al.*, 1989; 1992; Feybesse, 1990; Ledru *et al.*, 1991; Hirdes *et al.*, 1996; Allibone *et al.*, 2002; Feybesse *et al.*, 2006; Pouclet *et al.*, 2006; Vidal *et al.*, 2009). Consequently, the Eburnean rock record is key to explore the geodynamic changes across the Archean-Proterozoic transition.

The present understanding of the Eburnean metamorphism is limited by the lack of integration with geochronological and tectonic data. One of the scientific problems hampering our knowledge of the evolution of the West African Craton resides in the interpretation of the relationship between low-grade Birimian greenstone belts (Junner, 1940) and high-grade gneissic terranes dominated by TTG (tonalites-trondhjemites-granodiorites) suites. Are they coeval terranes metamorphosed in different tectonic settings before being assembled, or are greenstone belts discordant supracrustal rocks deposited on an older gneissic basement? Answering this question has strong implications on the geodynamic processes controlling the maturation and stabilisation of cratons after the Archean-Proterozoic transition. In order to do so, we present combined field, petrological and geochronological datasets of spatially associated low-, medium- and high-grade metamorphic rocks of north-western Ghana, in the south-eastern West African

Craton. The datasets are used to explore the mechanisms driving the exhumation and the tectonic assembly of the distinct metamorphic domains during the Eburnean orogeny.

GEOLOGICAL BACKGROUND

The Leo-Man rise forms the southern part of the West African Craton (Fig. 1). It consists of an Archean nucleus, the Kénéma-Man domain, which is flanked to the East by the Paleoproterozoic Baoulé-Mossi domain. The latter comprises Birimian greenstone belts, which are bounded by shear zones and alternate with granite-gneiss terranes. The greenstone belts comprise elongated sequences of volcanic and volcano-sedimentary rocks, shales, greywackes and chemical sedimentary rocks. The volcanic rocks range from basalts to rhyolites and have bimodal tholeiitic and calc-alkaline affinities (e.g. Leube *et al.*, 1990, Baratoux *et al.*, 2011). Across the craton, large volumes of volcanic rocks were emplaced between 2.30 and 2.20 Ga and volcanic activity locally continued until *c*. 2.10 Ga (Hirdes *et al.*, 1996; Kouamelan *et al.*, 1996; Doumbia *et al.*, 1998; Feybesse *et al.*, 2006). In the granite-gneiss terranes, intense plutonic activity generated juvenile TTG suites between 2.25 and 2.10 Ga, while magmatism gradually evolved towards more differentiated terms (e.g. potassic granites) until *c.* 2.07 Ga (e.g. Arnould, 1961; Egal *et al.*, 2002; Lompo, 2009). Following magmatic accretion of the juvenile crust between 2.25 and 2.15 Ga, the Paleoproterozoic crust was deformed during the 2.15-2.07 Ga Eburnean orogenic cycle (Bonhomme, 1962; Milési *et al.*, 1989; 1992; Feybesse, 1990; Ledru *et al.*, 1991; Hirdes *et al.*, 1996; Allibone *et al.*, 2002; Feybesse *et al.*, 2006; Pouclet *et al.*, 2006; Vidal *et al.*, 2009). Tarkwaian sedimentary rocks (conglomerates, phyllites and quartzites) form discordant basins on Birimian formations, and are interpreted to represent syn-orogenic to late-stage basins (Davis *et al.*, 1994, Perrouty *et al.*, 2012).

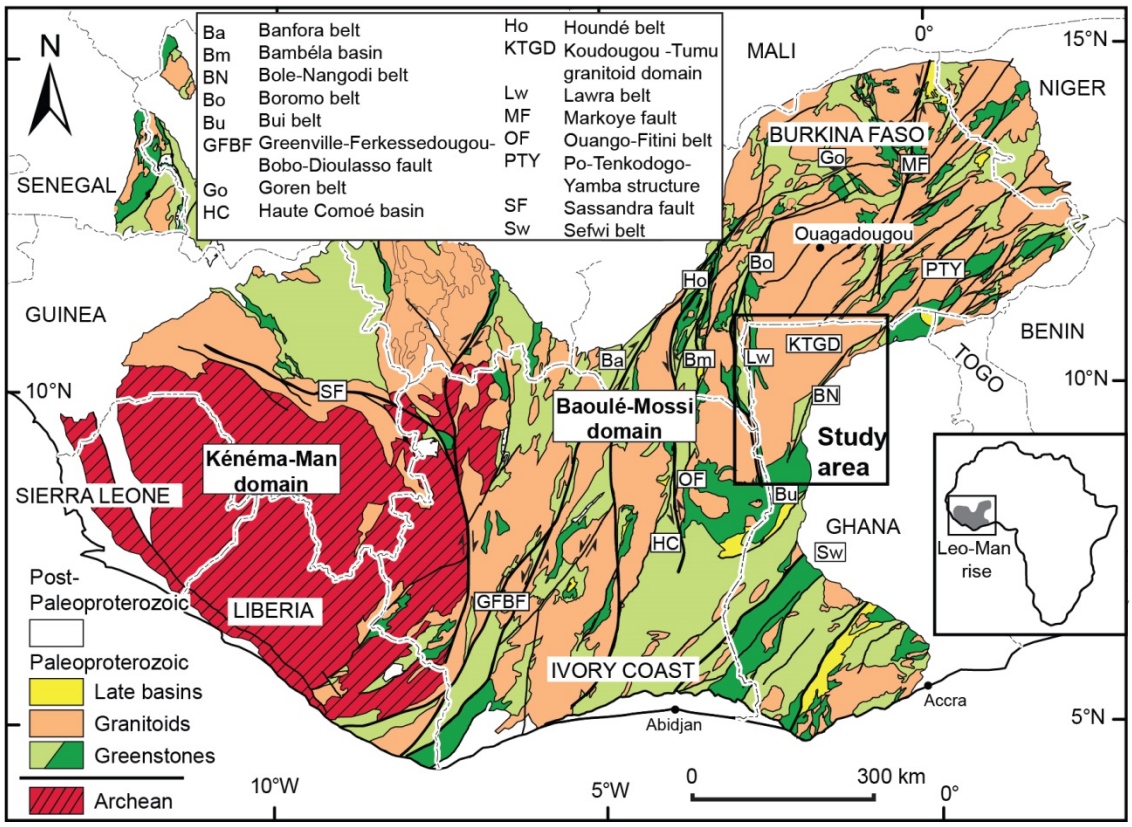

Fig. 1. *Simplified geological map of the Leo-Man rise (modified after the BRGM SIGAfrique map, Milési et al., 2004). Light green areas are made of intermediate to acidic volcano-sedimentary or volcano-clastic rocks, and the dark green areas represent mafic volcanic rocks.*

Based on geochemical data, some authors interpret the juvenile Paleoproterozoic West African Craton to have evolved from an oceanic plateau (Abouchami *et al.*, 1990; Boher *et al.*, 1992; Pouclet *et al.*, 1996, Lompo, 2009), while others argue it formed by the accretion of several volcanic arcs (e.g. Vidal & Alric, 1994; Attoh *et al.*, 2006; Dampare *et al.*, 2008). Tectonic accretion is proposed to have been dominated by gravity-driven "Archean-style" vertical tectonics by one school of thought (e.g. Pons *et al.*, 1995 in Niger; Vidal *et al.*, 2009 in Côte d'Ivoire), while lateral tectonics with thrust-related crustal thickening, equivalent to processes at work in modern orogens, is invoked by other authors (Milési *et al.*, 1989, 1992; Feybesse *et al.*, 2006 in Ghana).

Systematic spatial variations in metamorphic conditions across the Paleoproterozoic craton were recognised by various authors as early as Roques (1948) and Arnould (1961), who described large domains of exposed migmatitic gneisses juxtaposed with low-grade volcano-sedimentary units in north-eastern Côte d'Ivoire and southern Burkina Faso. High-T supra-solidus metamorphic conditions are also reported from formations in southern Ghana (Opare-Addo *et al.*, 1993, Feybesse *et al.*, 2006) and Côte d'Ivoire (Caby *et al.*, 2000). Ganne *et al.*, (2012) showed that rocks from greenstone belts in Senegal, Burkina Faso and Niger experienced different peak metamorphic conditions in the greenschist and

amphibolite facies, and at the greenschist-blueschist facies transition. Most volcano-sedimentary sequences are metamorphosed at sub-greenschist and greenschist-facies conditions (e.g. Kribek *et al.*, 2008). Amphibolite-facies metamorphic conditions are found in small volcano-sedimentary slivers within larger greenschist-facies belts. They are interpreted to result from contact metamorphic overprints (e.g. Vidal & Alric, 1994; Debat *et al.*, 2003; Gasquet *et al.*, 2003) and doming due to granite emplacement (Pons *et al.*, 1995; Soumaila & Garba, 2006). Other authors identified regional amphibolite-facies metamorphism unrelated to pluton emplacement (Liégeois *et al.*, 1991 in S Mali; Caby *et al.*, 2000 in NE Côte d'Ivoire; John *et al.*, 1999; Klemd *et al.*, 2002 and Galipp *et al.*, 2003, in Ghana). High-P granulites (Triboulet & Feybesse, 1998; Pitra *et al.*, 2010) and low-P granulites (Caby *et al.*, 2000; Pitra *et al.*, 2010) are described from the boundary between the Archean Kénéma-Man and Paleoproterozoic Baoulé Mossi domains. Most metamorphic rocks from the craton record conditions which fit a moderate to hot apparent geothermal gradient (>25°C km^{-1}) However, metamorphic rocks recording cold (~15°C km^{-1}) apparent geothermal gradients (Ganne *et al.*, 2012) are reported from eastern Burkina Faso.

Historically, the high-grade metamorphic domains were interpreted as the basement below the Birimain volcano-sedimentary formations. A polycyclic orogenic evolution was suggested based on field relationships reflecting poly-phased structural-metamorphic fabrics (Arnould, 1961; Bard & Lemoine, 1976; Ledru *et al.*, 1991). Following this model, the gneissic basement supposedly pre-dating the Birimian series underwent high-grade metamorphism during an early orogenic event (Tempier, 1986; Lemoine *et al.*, 1990; Tshibubudze *et al.*, 2009; Hein, 2010) which is termed "Eoeburnean" (De Kock *et al.*, 2011; 2012, Baratoux *et al.*, 2011; Perrouty *et al.*, 2012). After the deposition of Birimian sediments, the Paleoproterozoic domains were tectonically assembled against the Archean nucleus during the Eburnean orogeny (Kouamelan *et al.*, 1997), in a predominantly transcurrent tectonic regime (e.g. Feybesse, 1990; Ledru *et al.*, 1991; Jessel *et al.*, 2012). This polycyclic model is further supported by the recognition of deformed, low-grade upper Birimian volcano-sedimentary basins unconformably overlying basal Birimian rocks (e.g. Milési *et al.*, 1989; Ledru *et al.*, 1991; Vidal & Alric, 1994; Pouclet *et al.*, 1996; Perrouty *et al.*, 2012). In contrast to the polycyclic model, some authors (e.g. Leube *et al.*, 1990, Eisenlohr & Hirdes, 1992, Hirdes *et al.*, 1996, Gasquet *et al.*, 2003) argue for a single orogenic cycle. In this view, volcano-sedimentary basins are considered to be contemporaneous equivalents of volcanic belts and to illustrate lateral facies variations (Leube *et al.*, 1990; Eisenlohr & Hirdes, 1992; Hirdes *et al.*, 1996). The monocyclic model implies that terranes of contrasting metamorphic grade are coeval, and that low-grade metamorphic units represent supracrustal equivalents of high-grade migmatitic gneisses. Consequently, variations in the metamorphic conditions of coeval terranes would result from differential exhumation.

A limited number of geochronological data across the West African Craton point to a prolonged period of metamorphic overprint, which lasted *c.* 70 Ma. It spans from 2153±13 Ma given by a Sm-Nd garnet-whole rock isochron age (Boher *et al.*, 1992) to a 2105-2080 Ma period, defined by U-Pb and Pb-

Pb crystallisation ages of zircon, monazite and titanite (Hirdes *et al.*, 1996; Kouamelan *et al.*, 1996; Oberthür *et al.*, 1998; Feybesse *et al.*, 2006; De Kock *et al.*, 2011). Reworking of the Archean nucleus between 2080 and 2030 Ma (Kouamelan *et al.*, 1996, 1997) is supported by geochronological data obtained by different radiometric methods, including U-Pb zircon and monazite EPMA dating. However, due to the limited number of age data from only a few outcrops throughout the West African Craton, it remains unclear whether the metamorphic overprint was continuous during ~70 Ma or occurred during several discrete events. Thus, the available age data are of little help to discriminate between the poly- and monocyclic orogenic models.

GEOLOGY OF NORTH-WESTERN GHANA

Tectono-metamorphic domains

The geology of north-western Ghana is characterised by low- to high-grade tectono-metamorphic domains which are bounded by shear zones. Low-grade shales, volcano-sedimentary rocks, lavas such as dacites, andesites and basalts are found in the N-S Wa-Lawra belt (Fig. 2), which is the south-eastern continuation of the Boromo greenstone belt exposed in Burkina Faso (Baratoux *et al.*, 2011; Metelka *et al.*, 2011). Similar low-grade lithologies are found in the E-W trending Julie belt, which also comprises silicic volcano-sedimentary rocks, quartzites and arkoses. The Maluwe domain is a low-grade tectono-metamorphic terrane elongated SW-NE along ~250 km, which tapers off towards the NE to a thin sliver (Fig. 2). It is dominated by greywacke and shales which are intercalated with volcanoclastic rocks and felsic to intermediate lavas, deposited between 2197 and 2125 Ma (De Kock *et al.*, 2011). It also comprises chemical sedimentary rocks (Mn-rich cherts), along with gabbros and pyroxenites. The Nangodi belt (Melcher & Stumpfl, 1994), in the north-eastern part of the study area, is formed by a succession of shales, greywacke and Mn-rich cherts alternating with MORB-type basalts overlain by calc-alkaline andesitic to rhyolitic lava flows.

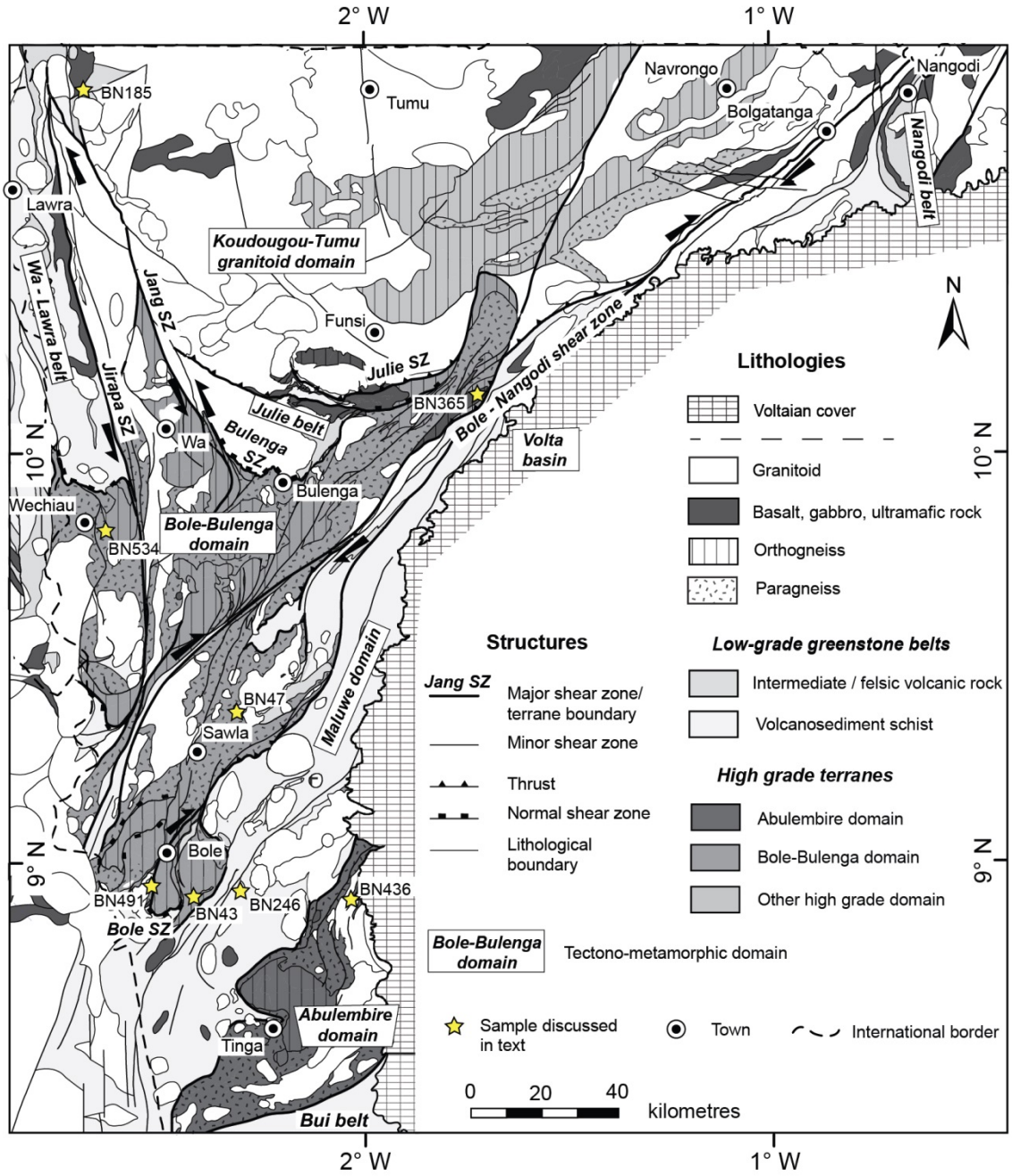

Fig. 2. *Litho-structural map of the study area. SZ = shear zone. Fault kinematics are indicated when they are unambiguous.*

High-grade orthogneisses, paragneisses and metabasites form most of the Bole-Bulenga domain, which is ~150 by 20-80 km long and elongated in a NNE direction. The paragneisses are derived from pelites, greywacke and volcano-sedimentary rocks. TTG and monzogranite orthogneisses with crystallisation ages between 2195 and 2135 Ma intrude them. The lithologies of the Bole-Bulenga domain are frequently migmatitic. To the south of the study area, the Abulembire domain shares many lithological and metamorphic similarities with the Bole-Bulenga domain. It is essentially made of paragneisses, sometimes migmatitic, intruded by TTG and granite orthogneisses, which were emplaced

between 2200 and 2125 Ma (Agyei Duodu *et al.*, 2009; De Kock *et al.*, 2011). The Abulembire domain is limited to the south by the Tarkwaian-type detrital sediments of the Bui belt (Zitsmann *et al.*, 1997).

The high-grade terranes and low-grade volcano-sedimentary belts are bounded by granitoid domains, such as the Koudougou-Tumu granitoid domain (Fig. 2). They comprise TTG orthogneisses, gabbros, granodiorite and granite plutons with crystallisation ages ranging between 2170 and 2127 Ma (Agyei Duodu *et al.*, 2009), and late-stage intrusive potassic porphyric granites, with crystallisation ages ranging between 2128 and 2086 Ma (Taylor *et al.*, 1992; Agyei Duodu *et al.*, 2009). The Paleoproterozoic rocks are overlain in central Ghana by the Neoproterozoic sedimentary rocks of the Volta basin (Affaton *et al.*, 1980).

Tectonic contacts separating the domains.

The contacts between the low-grade and high-grade domains are tectonic, and are formed by ductile high-strain zones. The Julie shear zone (SZ) is N-dipping and forms the transition between the Koudougou-Tumu granitoid domain, to the north, and the Julie belt, to the south (Fig. 2). Within the shear zone, the foliation in schists and gneisses dips 50-70° N and carries a stretching lineation plunging down-dip, towards higher-grade rocks. The Julie SZ is interpreted as a thrust, consistent with N-S directed shortening. The Bulenga SZ is a N-dipping shear zone which separates the Julie belt, to the north, from the high-grade Bole-Bulenga domain, to the south. The transition between the two domains is formed by a high-strain migmatitic orthogneiss. The gneissic banding has a moderate dip (40-50°) to the N and bears a mineral stretching lineation consistently plunging NNE, towards decreasing metamorphic grades. Similarly, the Bole SZ separates the southern Bole-Bulenga domain from the Maluwe basin (Fig. 2). It contains a high-strain orthogneiss. The gneissic banding dips 50-70° to the south, with the stretching lineation plunging down-dip, towards lower grade rocks. Therefore, the tectonic contacts forming the northern and southern limits of the high-grade Bole-Bulenga domains are interpreted as extensional shear zones, consistent with N-S directed extension.

These tectonic contacts are overprinted by later deformation and terminate on younger structures, which formed during NW-SE to E-W directed shortening. The Julie and Bulenga SZ both terminate to the west on the NNW-striking Jang sinistral strike-slip shear zone, along the north-eastern margin of the Bole-Bulenga domain. The Bole SZ is folded and transposed parallel to a NNE direction, where it is re-activated as a dextral strike-slip shear zone. The N-S Jirapa shear zone separates the Wa-Lawra belt from the Koudougou-Tumu granitoid domain. At its southern extension, the Jirapa SZ transects the Bole-Bulenga domain and merges with the NE-SW Bole-Nangodi SZ (Fig. 2), which extends for over 300 km into Burkina Faso (Naba *et al.*, 2004). Metamorphic breaks across the Bole-Nangodi SZ suggest that it is an early thrust re-activated during later deformation as a dextral strike-slip shear zone.

Sample	Lat	Lon	Lithology	Peak metamorphic assemblage
BN43	8.9289	-2.4320	Pelitic migmatitic paragneiss	Grt + Bt + Sill + Pl + Kf + L + Qz
BN47	9.3733	-2.3180	Pelitic paragneiss	Bt + Grt + Ky + Ms + Pl + Ilm + Qz
BN185	10.8798	-2.6954	Volcano-sedimentary schist	Chl + Ms + Pl + Cal + Qz
BN246	8.9305	-2.3082	Pelitic micaschist	Chl + Ms + Qz
BN365	10.1339	-1.7384	Migmatitic amphibolite	Hbl + Grt + Pl + Cpx + Ilm + L + Qz
BN436	8.9090	-2.0391	Mafic granofels	Grt + Ged + Ky + Pl + Rt + Qz
BN491	8.9275	-2.5326	Pelitic paragneiss	Bt + Grt + St + Pl + Ms + Ilm +Qz
BN534	9.8166	-2.6401	Pelitic migmatitic paragneiss	Bt + Grt + Ky + Pl + Ilm + L + Qz

Table 1. *Description and location of the investigated samples.*

PETROGRAPHY AND MINERAL CHEMISTRY

Eight rock samples from the Wa-Lawra belt, the Maluwe, Bole-Bulenga and Abulembire domains were investigated for this study (Table 1). Sampling of the principal metamorphic terranes of north-western Ghana aimed to establish the variability of metamorphic conditions at regional scale. Other samples were specifically picked along transects across tectonic contacts in order to evaluate metamorphic breaks. For five of these samples, petrographic and mineral descriptions, bulk rock and representative mineral compositions (Tables 2 & 3) are presented in the main text. The three remaining samples are presented as supporting information in Appendix S1. Mineral abbreviations are after Whitney & Evans (2010) except for melt (=L).

High-grade rocks

Sample BN 43 (Garnet – kyanite-bearing migmatitic gneiss)

Sample BN43 is a migmatitic paragneiss from the southern Bole-Bulenga domain. It was collected at the margin of a foliated granodiorite pluton that consists of a transitional zone evolving from subsolidus amphibolite-facies rocks to supra-solidus high-grade metamorphic rocks. The sample is from an outcrop of stromatic migmatites, which displays foliation-parallel leucosomes connected to granitic dykes oblique to the foliation, suggesting melt transport through the rock. Petrographic relationships are used to define a succession of five metamorphic assemblages identified here as (A) to (E) (Fig. 3). Paleosomes are composed of oriented biotite1, plagioclase, quartz and globular garnet1, which together belong to an early metamorphic assemblage (A) (Fig 3a). Garnet1 has a modal proportion of ~2-3% in paleosomes (Fig. 4a,b). It is zoned from core to rim with compositions Alm 72-73 => 73-75, Prp 13-14 => 15-16, Grs 5 => 4 and Sps 8 => 4 (Fig. 6a). The plagioclase in contact with garnet1 in the paleosome has An (= 100 x Ca/(Ca+Na)) 24-26. Neosomes contain kyanite porphyroblasts (Fig. 3b) up to 1 cm long,

set in leucocratic quartz-rich domains (Fig. 3e). Kyanite contains inclusions of plagioclase (An21-25) and white mica (Ms1; Fig. 3b), of which two phases are found. One has a dominant muscovite fraction ((Ms = 100 x K/(Na+K+Ca)) between 63 and 79, with Si = 3.21-3.09 a.p.f.u. and Al^{vi} ~1.95-1.88 a.p.f.u (based on 11 oxygens), while another has a high paragonite fraction (Pg = 100 x Na/(Na+K+Ca)) of 87-88, with Si = 2.95-3.08 a.p.f.u. and Al^{vi} = 2.00 a.p.f.u (11O).

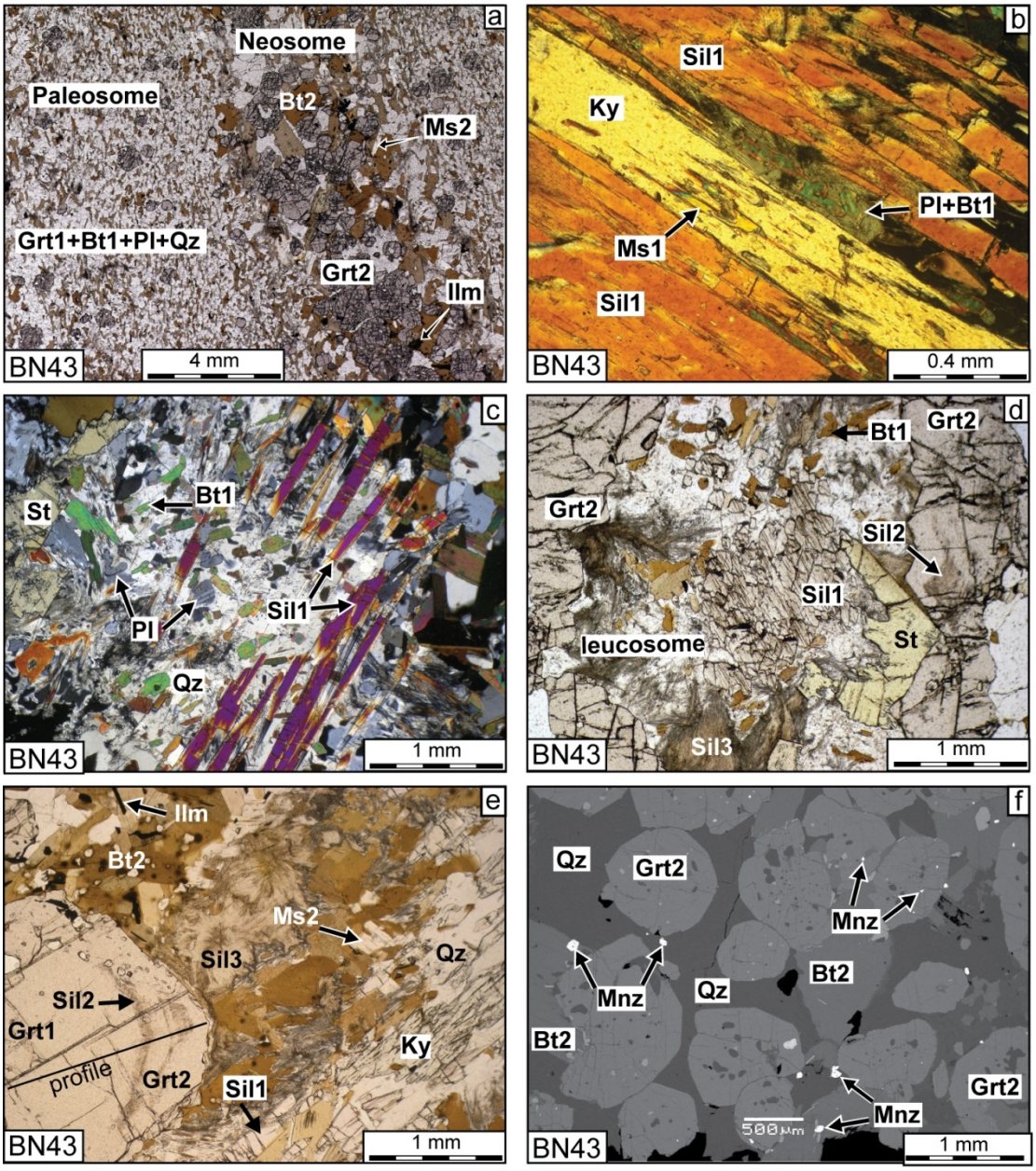

Fig. 3. *Photomicrographs (a-e) and REM image (f) of metapelite sample BN43. (a) Fine-grained paleosome comprising globular garnet1 and aligned biotite1 + plagioclase + quartz. Coarse grained neosome displays rounded garnet2 in leucocratic Qz-Pl rich domains overgrown by biotite2 and muscovite2. (b) Kyanite containing muscovite inclusions (Ms1) and overgrown by prismatic sillimanite porphyroblasts (Sil1) in a neosome. (c) Elongated crystals of prismatic sillimanite (Sil1) is a quartz-rich*

domain containig corroded grains of plagioclase and biotite1. (d) Garnet2 forms atoll-shaped aggregates around a leucocratic domain containing sillimanite1, and contains fibrolite inclusions (Sil2). Biotite1 is resorbed in the leucosome. Late-stage fibrolite (Sil3) and staurolite develop at the expense of garnet2. (e) Garnet porphyroblast showing a concentric inclusion rim of fibrolite (Sil2) at the transition between garnet1 and garnet2. The profile refers to Fig. 6a. Kyanite and prismatic sillimanite1 are set in a quartz-rich leucosome. Fibrolite, ilmenite and biotite2 flakes are found at the contact between leucosome and matrix. (f) Back-scattered electron image taken from the coarse-grained neosome visible in (a). Monazite grains are restricted to the neosome, and are commonly found enclosed in garnet2 and biotite2.

The first assemblage (A) occurs as minerals preserved in paleosomes and included in kyanite: Grt1 + Bt1 + Pl + Ms1 + Pg + Qz. It is typical of amphibolite-facies metamorphism. Kyanite is interpreted as a peritectic phase produced by the progressive breakdown of muscovite:

Ms1 + Pl + Qz => Ky + melt (L) ± Bt ± Kfs (R1)

Following Patiño Douce & Harris (1998), (R1) may be modelled as follows: 22Ms + 7Pl + 8 Qz => 25 L + 5Ky + 5Kfs + 2Bt. In this sample, R1 illustrates the transition from assemblage (A) to (B): Grt1 + Bt1 + Ky + Pl + Qz + L, which is transitional between the amphibolite and the high-pressure granulite facies. Corroded plagioclase in leucosomes (Fig. 3c) is An24-28, which partially overlaps with compositions of matrix grains. Euhedral kyanite is unresorbed and is overgrown by prismatic sillimanite (Sil1; Fig. 3b,c,e). This relationship illustrates an increase in the modal proportion of aluminosilicate (from 2.4 to 4.1%, Fig. 4a,b) between assemblages (B) and (C): Grt1 + Bt1 + Sil1 + Pl + Qz + L, formed at the amphibolite – low-P granulite facies transition.

Garnet 2 mainly occurs in coarse-grained neosomes (Fig. 3a,f). It displays a minor prograde zoning from centre to rim of Alm 75 => 79, Prp 17 => 19, Sps 4 => 2 and Grs 4 => 2 (Fig. 6a). Retrograde re-equilibration on margins is documented by decreasing #Mg (Mg/(Mg+Fe)) from 0.17 to 0.10. Garnet2 is sometimes globular (subhedral) or forms atolls overgrowing garnet1 and aluminosilicate-bearing leucosomes (Figs. 3d & 4a,b). In leucocratic segregates, garnet2 growth represents a modal proportion increases from 2.3 to 7.7% (Fig 4a,b). Fibrolite selvedge in garnet2 and between garnet1 and 2 (Sil2; Fig. 3d,e) demonstrate that garnet2 formed in the sillimanite stability field. Corroded biotite1 within neosomes (Fig. 3c,d) suggests that garnet2 is a peritectic phase produced by the progressive dehydration-melting of biotite (e.g. Le Breton & Thompson, 1988):

Bt1 + Sil1 + Pl + Qz => Grt2 ± Kfs + L (R2),

which has a pressure-dependent stoichiometry (Patiño Douce & Beard, 1995). This reaction results in the formation of assemblage (D): Grt2 + Bt1 + Sil2 + Pl + Qz + L at the amphibolite – low-P granulite facies transition, but at greater T compared to (C). Potassic feldspar is not observed as a product of reactions (R1) nor (R2), as is frequently the case during water-undersaturated melting of metapelites (Carrington & Watt, 1995). Monazite is restricted to neosomes and is occasionally included in garnet2 (Fig. 3f). This observation indicates that monazite crystallised before or simultaneously with assemblage (D).

Sample	wt %										
	SiO_2	TiO_2	Al_2O_3	FeO	MnO	MgO	Na_2O	K_2O	CaO	H_2O	Total
Average unmolten paragneiss (N=21)	63.4	0.71	18.4	6.57	0.08	2.46	2.86	2.50	1.95	1.13	100.0
BN43	50.7	1.22	23.3	10.3	0.11	4.43	2.69	3.34	1.50	exc.	97.5
BN436	43.8	2.08	26.3	15.0	0.18	5.88	1.05	0.14	3.54	exc.	98.0
BN436 (fractionated)	46.6	2.67	28.2	10.3	0.00	6.28	1.34	0.18	4.24	exc.	99.9
BN47	58.3	0.86	21.5	8.53	0.09	2.71	1.03	2.29	0.83	exc.	96.2
BN365	52.27	0.88	13.8	10.8	0.20	7.32	2.23	0.28	10.7	1.49	100.0
BN534	67.7	0.65	15.9	6.37	0.08	2.21	2.67	1.82	2.29	exc.	99.6
BN491	65.5	0.69	16.1	7.84	0.09	2.95	0.96	0.90	2.57	exc.	97.6

Table 2. *Chemical compositions (oxide wt%) of samples used for P-T pseudosection calculation. Exc. = excess. Compositions with constrained water content are normalised to 100.*

Large (up to 5mm long) euhedral biotite crystals (Bt2) form selvedge microstructures around leucocratic domains (Fig. 3a, e). They have compositions of #Mg = 0.51-0.56, Ti^{vi} = 0.11-0.07 a.p.f.u. and Al^{vi} = 0.40-0.80 a.p.f.u.), similar to biotite1. Neosomes are overgrown by fibrolite aggregates (Sil3, Fig. 3d, e). Biotite selvedge microstructures may be interpreted both as products of the muscovite dehydration reaction or as a retrograde phase developed at the expense of atoll-shaped garnet2 and melt (e.g. Brown, 2002). Observations of atoll-shaped garnet2 replacement by biotite selvedge at the interface between leucosomes and paleosomes suggest that this texture is due to retrogression. It reflects the following partial back-reaction:

Grt2 + L => Bt2 + Sil3 + Pl + Qz (R-2),

which also explains formation of fibrolite aggregates. White mica (Ms2) overgrows other phases in leucosomes (Fig. 3a, e) and has a Ms composition with a Pg content of 18-23, with Si = 3.00-3.08 a.p.f.u. and Al^{vi} ~1.92-2.01 a.p.f.u (11 O). It is a "late-stage" phase produced by secondary hydration, probably as hydrous fluids exsolved from the crystallising melt (Brown, 2002), when the rock crossed back over the solidus. Staurolite also is a late phase overgrowing previous microstructures (Fig. 3c,d). Its #Mg varies from 0.14 to 0.24. Euhedral ilmenite grains are in contact with staurolite and recrystallized biotite. These

phases indicate the rock witnessed a H_2O-rich fluid input at subsolidus conditions that locally formed the amphibolite-facies assemblage (E): Grt2 + Bt2 + St + Ilm + Pl + Qz.

Sample BN47 (Garnet – kyanite - staurolite schist)

Sample BN47 is from a paragneiss of the Bole-Bulenga domain. It displays a penetrative metamorphic foliation which comprises oriented white mica, biotite, plagioclase and quartz. The foliation is parallel to a transposed sedimentary layering that controls at the cm scale the distribution and modal proportion of garnet, staurolite and kyanite porphyroblasts. Petrographic relationships are used to define a succession of four metamorphic assemblages (A) to (D) (Fig. 4). Garnet forms millimetric euhedral grains with cores (Grt1, white dashed line in Fig. 4e) of Prp4-6, Alm70-72, Grs14-16 and Sps7-8 (Fig. 6a), which contain rare quartz and chlorite inclusions. The first assemblage (A) is represented by Grt1 + Chl + Qz, with modal proportion of garnet being ~1% (Fig. 4c,d), and is consistent with low-T amphibolite-facies conditions. Garnet rims (Grt2) display abundant small (~10 µm) quartz inclusions. They have a composition of Prp10-13, Alm77-80, Grs4-8 and Sps1-4, and form 8-9 vol% of the rock. Core to rim zoning is characteristic of garnet growth during prograde metamorphism. Poikilitic staurolite (St1), with a #Mg of 0.15-0.17, contains quartz and ilmenite inclusion trails oblique to the metamorphic banding (Fig. 4e), and is in equilibrium contact with garnet2. These phases identify the amphibolite-facies assemblage (B) Grt2 + St1 + Ilm + Qz. Kyanite forms centimetric elongated porphyroblasts aligned parallel to the fabric in the matrix, or rotated due to low intensity shearing. It is in equilibrium contact with Bt + Pl + Ilm + Ms + Grt2. Matrix biotite has compositions of #Mg = 45-52 with Ti^{vi} varying from 0.09 to 0.12 a.p.f.u. Plagioclase displays significant inter-grain compositional variations, ranging from An 20 to 45. White mica has a muscovite composition with a Pg 18-23, Si = 3.04-3.09 a.p.f.u and Al^{vi} =1.92 a.p.f.u (11 O). These phases define assemblage (C) Grt2 + Ky + Bt + Pl + Ilm + Qz ± Ms, which corresponds to the upper-amphibolite facies. Monazite forms elongated grains parallel to the metamorphic banding in the matrix and is also found enclosed in kyanite porphyroblasts (Fig. 4f). Hence, it crystallised before or during the formation of assemblage (C).

Sample	BN 43								BN 47							BN 436									
Mineral	Grt1	Grt2	St	Pg	Bt1	Bt2	Ms2	Pl	Grt1	Grt2	St1	St2	Bt	Ms	Pl	Grt2	Grt1	St2	St1	Pg1	Chl2	Chl1	Ged	Pl2	Pl3
position	core	rim	retrog.	Ky incl.	corroded	selvedge	retrog.	matrix	rim	core	porphyroblast		matrix	matrix	matrix	rim	core	retrogr.	Grt incl.	Grt incl.	retrog.	Grt incl.	matrix	matrix	Grt incl.
SiO_2	36.7	36.4	28.1	45.7	36.1	35.6	46.1	61.9	38.0	37.2	28.2	27.5	35.5	45.5	62.4	37.7	37.0	28.6	28.3	44.9	27.3	24.8	46.5	51.2	57.1
TiO_2	0.05	b.d.l	0.48	0.02	2.22	1.95	0.46	b.d.l	b.d.l	0.02	0.62	0.72	2.08	0.32	0.07	0.13	0.02	0.59	0.82	b.d.l	b.d.l	0.02	0.14	0.07	b.d.l
Al_2O_3	21.2	21.2	53.2	39.9	19.2	18.9	35.7	23.6	20.7	21.3	54.2	53.3	19.5	36.35	23.7	21.7	21.4	55.4	54.4	42.0	24.0	22.8	14.7	31.6	28.0
Fetot as FeO	33.3	35.8	13.8	0.25	17.4	16.8	0.93	0.10	36.0	31.6	14.0	14.4	19.0	0.95	0.08	30.9	35.0	9.99	11.9	0.77	14.5	27.9	19.0	b.d.l	0.14
MnO	3.07	1.12	b.d.l	0.02	b.d.l	0.01	0.09	0.05	0.99	3.46	0.02	0.05	b.d.l	0.05	b.d.l	0.49	0.92	0.01	0.08	0.01	0.01	0.05	0.06	b.d.l	0.04
MgO	4.22	4.65	1.22	0.05	11.2	11.5	0.56	b.d.l	2.95	1.30	1.52	0.99	9.85	0.21	b.d.l	6.70	4.74	1.35	0.49	b.d.l	21.9	11.7	15.9	b.d.l	b.d.l
CaO	1.28	1.10	0.03	0.68	0.04	0.05	0.03	5.04	1.61	5.86	b.d.l	0.04	0.06	0.04	4.90	2.27	1.15	0.01	b.d.l	2.84	0.04	b.d.l	0.50	14.2	9.72
Na_2O			b.d.l	6.60	0.28	0.09	1.67	8.76			b.d.l	0.01	0.04	1.51	9.19			0.02	0.17	6.14	b.d.l	b.d.l	1.01	3.69	6.38
K_2O				0.95	9.10	8.79	8.58	0.06					8.98	8.98	0.06					0.39	0.01	b.d.l	b.d.l	0.04	0.03
Cr_2O_3	b.d.l	0.03	0.06	0.01	0.06	0.13	0.14	b.d.l	0.03	0.02	b.d.l	0.07	0.03	b.d.l	b.d.l	0.05	0.09	0.05	0.17	0.05	b.d.l	b.d.l	0.01	b.d.l	b.d.l
ZnO			0.48		b.d.l	b.d.l	b.d.l	b.d.l			0.15	0.25	b.d.l	b.d.l		b.d.l	b.d.l	0.86	1.51		b.d.l	b.d.l	b.d.l	b.d.l	b.d.l
Total	99.8	100.3	97.4	94.2	95.6	94.0	94.4	99.5	100.2	100.8	98.7	97.4	95.0	93.9	100.4	99.8	100.4	96.9	97.9	97.2	87.7	87.3	97.8	100.9	101.4
Oxygen	12	12	46	22	22	22	22	32	12	12	46	46	22	22	32	12	12	46	46	22	28	28	23	32	32
Si	5.91	5.85	7.84	5.92	5.41	5.41	6.15	11.0	6.10	5.96	7.75	7.71	5.39	6.10	11.0	5.93	5.91	7.87	7.83	5.68	5.39	5.31	6.66	9.25	10.1
Al^{IV}	0.09	0.15	0.16	2.08	2.59	2.59	1.85	4.96	0.00	0.04	0.25	0.29	2.61	1.90	4.93	0.07	0.09	0.13	0.17	2.32	2.61	2.69	1.34	6.72	5.85
Al^{VI}	3.93	3.86	17.3	4.00	0.80	0.80	3.76		3.90	3.99	17.3	17.3	0.87	3.84		3.94	3.94	17.8	17.6	3.93	2.97	3.06	1.15		
Fe^{3+}	0.22	0.42	0.54	0.00	0.00	0.00	0.03	0.01	0.00	0.05	0.55	0.53	0.00	0.00	0.01	0.14	0.21	0.02	0.22	0.02				0.00	0.02
Ti	0.01	0.00	0.10	0.00	0.25	0.22	0.05	0.00	0.00	0.00	0.13	0.15	0.24	0.03	0.01	0.02	0.00	0.12	0.17	0.00	b.d.l	0.00	0.02	0.01	0.00
Cr	0.00	0.00	0.01	0.00	0.01	0.02	0.01		0.00	0.00	0.00	0.02	0.00	0.00		0.01	0.01	0.01	0.04	0.01	b.d.l	b.d.l	0.00		
Mg	1.01	1.11	0.51	0.01	2.49	2.62	0.11	0.00	0.70	0.31	0.62	0.41	2.23	0.04	0.00	1.57	1.13	0.55	0.20	0.00	6.44	3.75	3.41	0.00	0.00
Fe^{2+}	4.49	4.82	2.68	0.03	2.18	2.13	0.10	0.00	4.83	4.23	2.68	2.84	2.41	0.11	0.00	4.06	4.67	2.28	2.54	0.08	2.39	5.00	2.28	0.00	0.00
Mn^{2+}	0.42	0.15	0.00	0.00	0.00	0.00	0.01	0.01	0.13	0.47	0.00	0.01	0.00	0.01	0.00	0.07	0.12	0.00	0.02	0.00	0.00	0.01	0.01	0.00	0.01
Ca	0.22	0.19	0.01	0.09	0.01	0.01	0.00	0.96	0.28	1.01	0.00	0.01	0.01	0.01	0.93	0.38	0.20	0.00	0.00	0.38	0.01	b.d.l	0.08	2.75	1.85
Na	0.00	0.00	0.00	1.65	0.08	0.03	0.43	3.02	0.00	0.00	0.00	0.00	0.01	0.39	3.15			0.01	0.09	1.51	b.d.l	b.d.l	0.28	1.29	2.19
K			0.00	0.16	1.74	1.71	1.46	0.01					1.74	1.54	0.01					0.06	0.00	0.00		0.01	0.01
Zn			0.10	0.00	0.00	0.00	0.00				0.03	0.05	0.00	0.00				0.17	0.31	0.00	0.00	0.00			
xPrp	0.17	0.19							0.12	0.05						0.26	0.18							0.32	0.54
xAlm	0.72	0.75							0.81	0.70						0.67	0.76							0.68	0.46
xSps	0.07	0.03							0.02	0.08						0.01	0.02							0.89	0.90
xGrs	0.05	0.03							0.05	0.17						0.06	0.03								
xMg	0.18	0.19	0.16	0.27	0.53	0.55			0.13	0.07	0.16	0.11	0.48			0.28	0.19	0.20	0.07		0.73	0.43	0.60		
xOr								0.00							0.00									0.00	0.00
xAb								0.75							0.77									0.32	0.54
xAn								0.24							0.23									0.68	0.46

Table 3. *Representative chemical compositions of minerals forming metamorphic assemblages used to constrain P-T conditions and P-T paths from pseudosections. b.d.l. = below detection limit.*

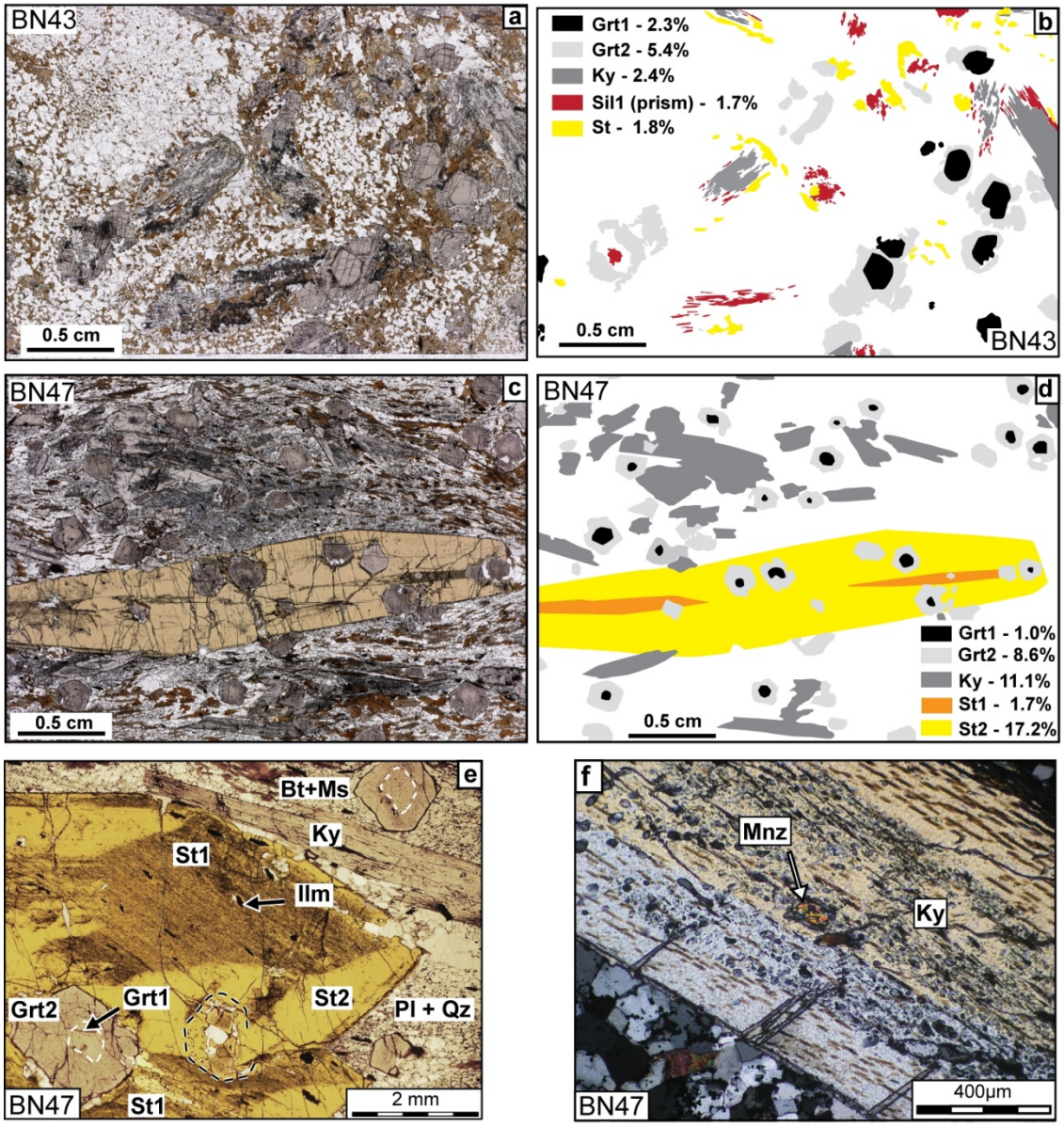

Fig. 4. *Modal proportion of metamorphic porphyroblasts deduced from thin section image analysis for samples BN43 (a, b) and BN47 (c, d). (e-f) Photomicrograph of metapelite sample BN47. (e) Subhedral garnet displays inclusion-poor cores (white dashed contour) and is included in staurolite. Poikiloblastic staurolite1 contains oriented quartz and ilmenite inclusions. Garnet and staurolite1 are overgrown by post-kinematic euhedral staurolite2. The latter partly replaces garnet (black dashed contour) and overprints the metamorphic banding. (f) Monazite grain included in kyanite in sample BN47.*

Assemblage (C) is overgrown by post-kinematic inclusion-poor staurolite (St2), which has a #Mg 0.12-0.15. The modal proportion of staurolite2 is ~ 17% (Fig. 4c, d), i.e. 10 times greater than that of the staurolite1. Garnet included in staurolite2 is sometimes partly resorbed and replaced by staurolite (black

dashed line, Fig 4e). This reflects the transition from the stability field of kyanite to that of staurolite across the balanced reaction:

0.17 Grt + 1.86 Ky => 0.25 St2 + 1.00 Qz (R1),

resulting in the formation of lower amphibolite-facies assemblage (D) : Grt2 + St2 + Bt + Pl + Ilm + Qz.

Sample BN436 (Garnet – kyanite – gedrite granofels)

Sample BN436 comes from a boudin of competent rock in high-grade meta-sedimentary rocks of the Abulembire domain. It is characterised by a low-Si, high-Al and Mg bulk rock composition (Table1), and a high garnet modal proportion (~50%). Rock-forming minerals do not display any preferential orientation. The rock comprises garnet, kyanite and gedrite porphyroblasts, and a mesocratic matrix which includes staurolite, chlorite, paragonite, plagioclase, rutile and quartz (Fig. 5). Petrographic relationships identify four successive metamorphic assemblages (A) to (D). Garnet porphyroblasts have a radius of up to 1 cm, and display a zoning pattern typical of prograde metamorphism (Fig. 6a). From core (Grt1) to rim (Grt2), composition changes are Prp 17-20 => 26-32, Grs 3-6 => 6-8, Alm 76-78 => 61-65 and Sps 2 => 0.5-1. Garnet1 preserves multi-mineral inclusions belonging to early metamorphic assemblages. Rare epidote and rutile grains are found together in contact with radial chlorite aggregates (#Mg = 0.39-0.51) in garnet1 (Fig. 5a). This suggests the formation of a first greenschist- to amphibolite-facies metamorphic assemblage (A) Grt1 + Chl1 + Ep + Rt1 + Qz. Rutile inclusions are sometimes rimmed by ilmenite, suggesting a transition from the stability field of rutile to that of ilmenite. Another set of coexisting inclusions provides evidence for a second amphibolite-facies assemblage that includes Grt1 + Chl1 + St1 + Pg1 + Pl1 + Ilm + Qz (B) (Fig. 5b). Plagioclase1 from assemblage (B) is strongly sericitised. White mica has a muscovite composition with Pg 0.77-0.83, Si = 2.84-3.02 a.p.f.u. and Al^{vi} = 1.95 a.p.f.u (11 O), while St has #Mg of 0.07-0.10.

Garnet outer cores (Grt2) contain kyanite, biotite and plagioclase2 (An45-47) inclusions. Garnet2 is in contact with matrix kyanite, gedrite and plagioclase3 (Fig. 5c,d). Gedrite displays small variations in #Mg between 0.58 and 0.61, Al^{iv} from 1.3 to 1.7 a.p.f.u., and Al^{vi} between 1.1 and 1.4 a.p.f.u. $(Na+K)_A$ is 0.21-0.31 a.p.f.u. and $(Na+Ca)_B$ is 0.12-0.17 a.p.f.u. Biotite grains have a #Mg ~0.54, and plagioclase3 is An 57-71. Ilmenite is absent from the matrix, suggesting that it does not belong to the peak metamorphic assemblage. Rutile2 is present in garnet outer core, in gedrite, and is common in the matrix. These relationships indicate the crossing of the following pressure-dependent reaction (Bohlen & Liotta, 1986):

Pl2 + Ilm + Qz => Grt2 + Rt2 (R1),

and the formation of the peak assemblage (C): Grt2 + Ky + Ged + Pl3 + Rt2 + Qz ± Bt, in the upper-amphibolite-facies. Using the compositions in Table 3, (R1) can be balanced in the CFMASHTi system as

0.28 An + 1.16 Ilm + 1.00 Qz = 0.55 Grt2 + 2.35 Rt2. Monazite is only preserved as single grain inclusions in garnet (Fig. 5e), suggesting that it crystallised before the formation of assemblage (C).

The peak assemblage is overgrown by fibrous chlorite2 (#Mg = 0.70-0.74) and euhedral staurolite2 (#Mg = 0.16-0.23), while gedrite is pseudomorphosed by intergrown paragonite2 and chlorite3 (Fig. 5c,d). This reflects secondary hydration and the local formation of a late metamorphic (greenschist- to amphibolite-facies) assemblage, which includes Grt2 + Pg2 + Chl2 + St2 + Qz (D).

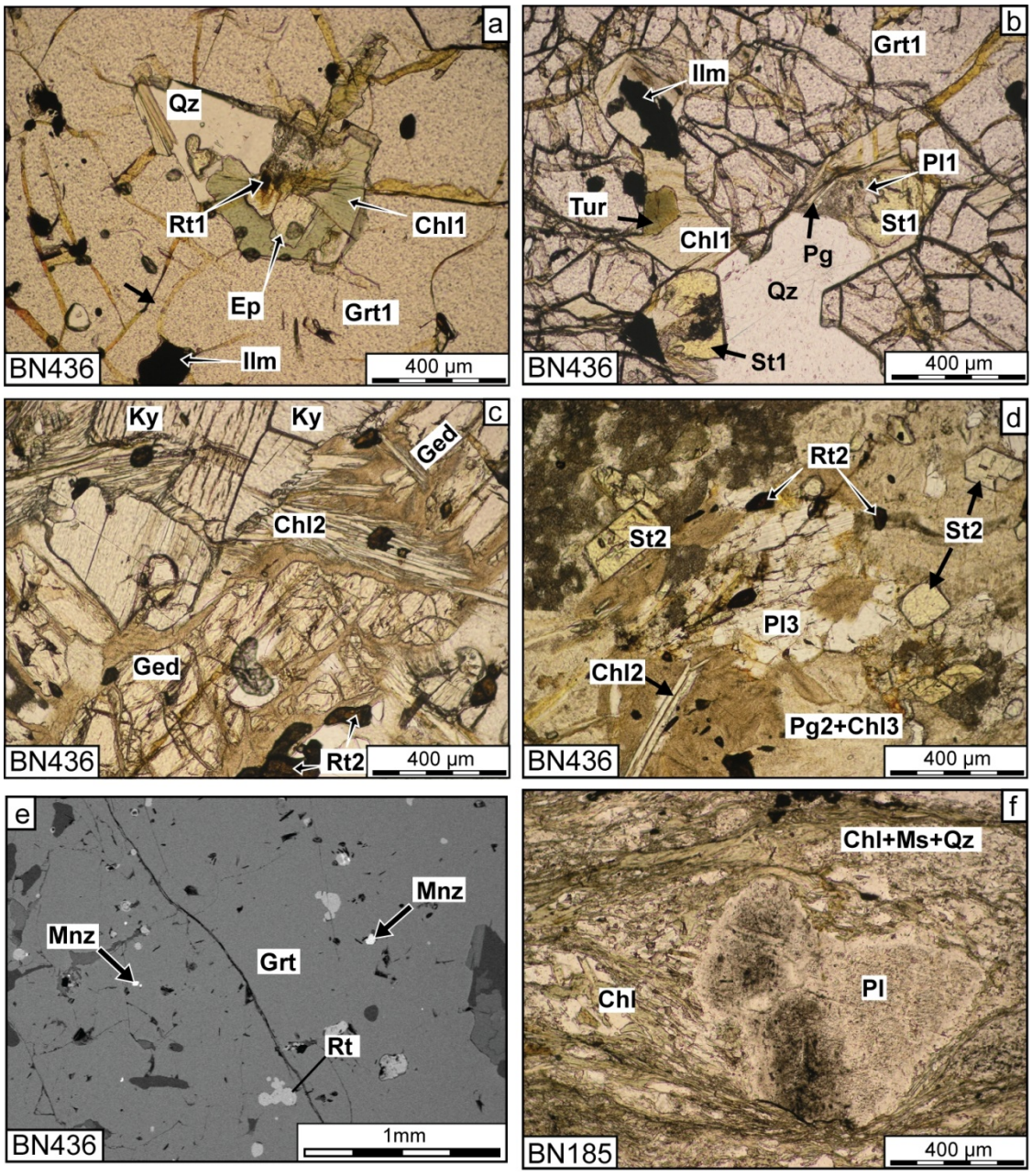

Fig. 5. *Photomicrographs and back-scattered electron image of samples BN436 (a-e) and BN185 (f). (a) Pluri-mineral inclusion in garnet porphyroblast core (Grt1), including chlorite1, epidote, rutile1 and quartz. (b) Pluri-mineral inclusion in garnet1 including paragonite1, plagioclase1, staurolite1, ilmenite,*

quartz, turmaline and chlorite with a radial growth pattern. (c) Kyanite, gedrite and rutile2 in contact in the matrix belong to the peak metamorphic assemblage. (d) Retrograde phases in the matrix include staurolite, fibrous chlorite2 and intergrown chlorite3 + paragonite2. They develop in replacement of an assemblage that includes plagioclase3, gedrite and kyanite. Note the abundance of rutile2 included in these phases and in their pseudomorphs. (e) Monazite and rutile inclusions in a garnet porpyroblast of sample in BN436. (f) Chlorite-muscovite-quartz alternation defines foliation and develops in pressure shadow zones of plagioclase porphyroclasts in volcano-sedimentary schist BN185.

Chlorite-mica schists

Sample BN185 (volcano-sedimentary rock)

Sample BN185 is an Al-rich silicic volcano-sedimentary rock intercalated in a sequence of volcanic and volcanoclastic rocks, and originates from the north-western Wa-Lawra belt. It develops a schistosity, contains plagioclase porphyroclasts and displays alternating quartz-rich and chlorite-muscovite-rich layers. Calcite occasionally forms aggregates elongated parallel to the schistose fabric. Chlorite and white mica show strong intra-grain and inter-grain chemical variations. Chlorite #Mg varies between 0.42-0.52, although most values cluster in the range of 0.47-0.50. White mica has a strong muscovite fraction, Ms (= 100x K/(K+Na+Ca)) varies from 89 to 99 (Table S2). Chemical compositions of chlorite and white mica from sample BN185 are presented in Fig. 6b. Chlorite compositions plot near to the clinochlore + daphnite end-member (Appendix S3). They vary from a more ferro-magnesian composition of Clin+Daph65 Am30 Sud5 to a more silicic composition of about Clin+Daph60 Am15 Sud35. Three compositional groups (A-C) are defined base on chlorite Si content (Fig. 6b). White mica compositions are close to the muscovite end-member, but they vary between Ms75 Prl25 Cel0 and Ms75Prl5Cel20 (Fig. 6). Three compositional groups (A-C) are defined based on white mica K content.

Sample BN246 (Micaschist)

Sample BN246 is a micaschist sampled in the southern Maluwe domain, near a high-strain zone mineralised in gold, at the contact between meta-sedimentary rocks and an elongated granodiorite body. It displays an assemblage of intergrown quartz-chlorite-muscovite, and a marked mineral orientation parallel to the schistosity. White mica is the least abundant of the three phases. It has variable compositions ranging from Ms74 to Ms95 (Table S2), Si = 3.10-3.40 a.p.f.u. and Al^{vi} =1.80-1.95 a.p.f.u (11 O). Chlorite #Mg is within 0.31-0.36, Si = 2.64-2.75 a.p.f.u., Al^{vi} = 1.46-1.52 (14 O). The sample contains abundant pyrite and is crosscut by pyrite-calcite veins.

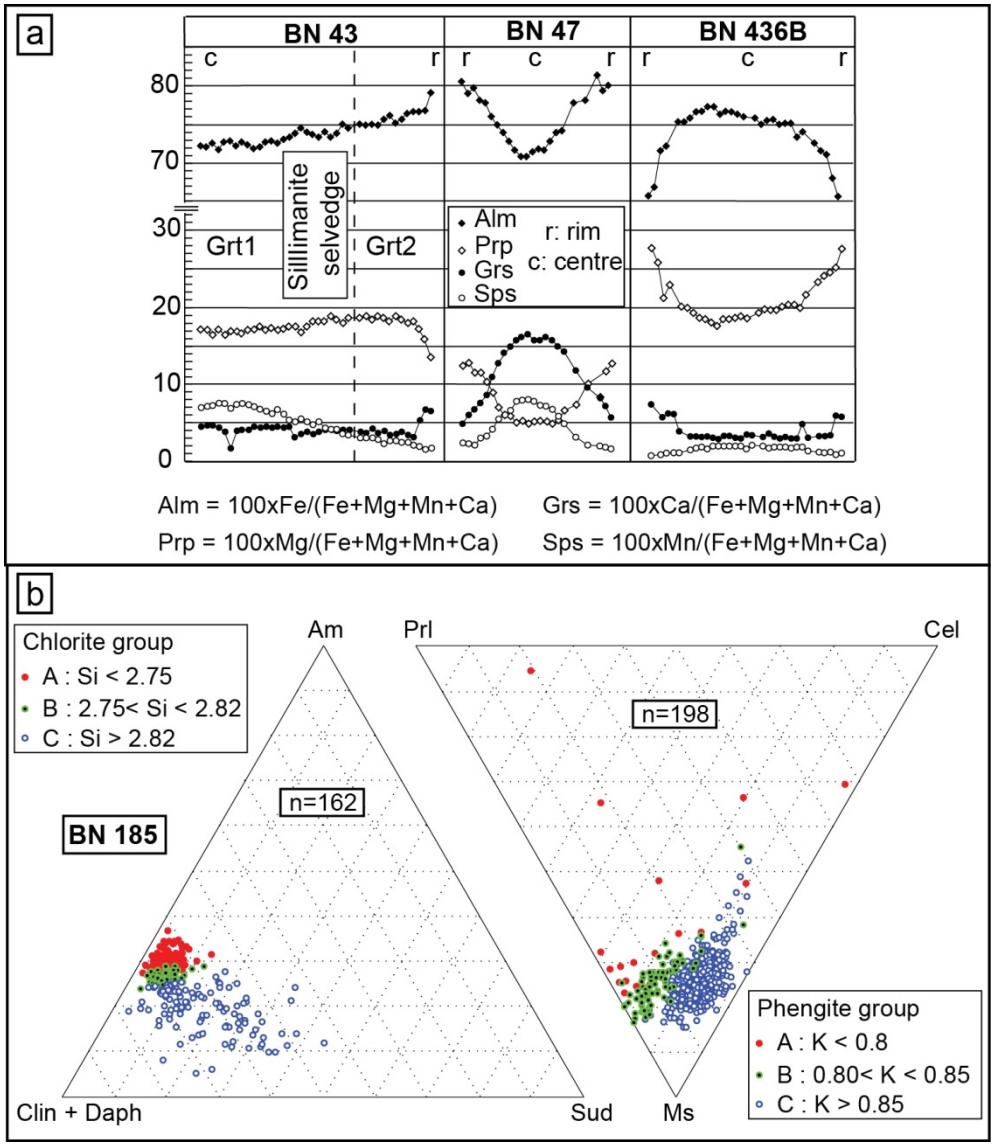

Fig. 6. *(a) Chemical composition variations along radial profiles across garnet porphyroblasts of samples BN43, BN47 and BN436. The location of the profile for BN43 is shown in Fig. 3e. (b) Ternary diagrams showing the end-member proportions of chlorite and white mica from sample BN185 used for multi-equilibria calculations. Values are in a.p.f.u. Colours illustrate mineral groups defined by compositional criteria.*

Complementary samples

Among the three complementary samples presented in Appendix S1 and Fig. S1, two have compositions suggesting greywacke or pelitic protoliths (BN534, BN491), and one is derived from a gabbro or a basalt (BN365). Peak metamorphic assemblages in samples BN534 and BN 365 are Grt + Bt + Ky + Rt + Pl + Qz + L and Grt + Hbl + Cpx + Ilm + Pl + Qz + L respectively, and correspond to the amphibolite – high pressure granulite facies transition. The peak metamorphic assemblage in sample BN491 is Grt + Bt + Ky + Ms + Ilm + Pl + Qz and formed in the amphibolite facies.

Pair	**1**		**2**		**3**		**4**		**5**		**6**		**7**		**8**		**9**		**10**		**11**		**12**	
Mineral	Chl	Wm	Chl	Wm	Chl	Wm	Chl	Wm	Chl	Wm	Chl	Wm	Chl	Wm	Chl	Wm	Chl	Wm	Chl	Wm	Chl	Wm	Chl	Wm
Analysis	C4-42	G1_2_16	C4-74	C1-G1_7_2	C4-122	C1-G1_18_2	C4-18	C1-G1_5_2	C2-G2_11_3	C1-G1_18_5	C4-54	C1-G1_14_3	C2-G2_6_1	C3-102	C4-117	C3-11	C4-15	C3-102	G1_5_12	C1-G1_25_1	G1_6_19	C3-11	G1_5_20	C3-3
Si	2.85	3.33	2.86	3.36	2.81	3.26	2.78	3.21	2.77	3.24	2.77	3.31	2.75	3.30	2.74	3.21	2.73	3.30	2.71	3.25	2.69	3.21	2.68	3.25
Ti	0.01	-	0.03	-	0.01	0.01	-	0.01	-	0.01	0.01	0.01	0.00	0.01	-	0.01	-	0.01	-	-	0.02	0.01	-	-
Al^{IV}	1.15	0.67	1.14	0.64	1.19	0.74	1.22	0.79	1.23	0.76	1.23	0.69	1.25	0.70	1.26	0.79	1.27	0.70	1.29	0.75	1.31	0.79	1.32	0.75
Al^{VI}	1.37	1.67	1.32	1.65	1.35	1.68	1.35	1.59	1.30	1.65	1.27	1.66	1.34	1.67	1.34	1.60	1.34	1.67	1.42	1.63	1.35	1.60	1.40	1.63
Al	2.52	2.34	2.46	2.29	2.54	2.42	2.57	2.39	2.53	2.41	2.50	2.35	2.59	2.37	2.59	2.40	2.62	2.37	2.71	2.38	2.66	2.40	2.71	2.37
Fe^{2+}	2.42	0.14	2.36	0.13	2.25	0.15	2.32	0.25	2.37	0.18	2.37	0.17	2.34	0.18	2.36	0.26	2.34	0.18	2.34	0.23	2.32	0.26	2.36	0.24
Mn^{2+}	0.01	-	0.01	-	0.03	-	0.02	-	0.02	-	0.02	-	0.01	-	0.01	-	0.03	-	0.02	-	0.02	-	0.02	-
Mg	2.04	0.20	2.14	0.23	2.26	0.17	2.22	0.26	2.25	0.22	2.28	0.20	2.25	0.22	2.22	0.25	2.24	0.22	2.13	0.24	2.22	0.25	2.16	0.24
Na	-	0.01	-	0.02	-	0.03	-	0.01	-	0.01	-	0.02	-	0.04	-	0.04	-	0.04	-	0.04	-	0.04	-	0.01
Ca	0.01	-	0.01	-	0.01	0.01	-	-	0.01	-	-	-	-	-	-	-	-	-	0.01	0.00	-	-	-	-
K	0.01	0.90	0.01	0.89	-	0.89	-	0.88	-	0.86	-	0.85	-	0.79	-	0.81	-	0.79	-	0.84	-	0.81	-	0.82
Cr	-	0.01	0.01	0.01	0.01	0.02	-	0.02	-	0.03	0.01	0.02	0.01	-	0.01	0.02	0.01	-	0.01	0.01	0.01	0.02	0.01	0.03
X Am	0.17		0.16		0.22		0.25		0.25		0.24		0.26		0.13		0.30		0.32		0.32		0.34	
X Clin-Daph	0.71		0.74		0.69		0.69		0.71		0.73		0.69		0.34		0.66		0.61		0.64		0.61	
X Sud	0.12		0.11		0.09		0.07		0.04		0.03		0.05		0.02		0.04		0.07		0.04		0.04	
X Cel		0.26		0.29		0.22		0.13		0.16		0.21		0.16		0.08		0.16		0.14		0.08		0.11
X Ms		0.62		0.58		0.65		0.63		0.63		0.60		0.56		0.59		0.56		0.59		0.59		0.60
X Prl		0.09		0.08		0.06		0.10		0.11		0.12		0.16		0.14		0.16		0.12		0.14		0.16
Group	C	C	C	C	B	C	B	C	B	C	B	B	B	B	A	B	A	A	A	B	A	B	A	B
P (bar)	**915**		**1999**		**739**		**1136**		**2538**		**4195**		**4925**		**3357**		**6343**		**5789**		**8004**		**10636**	
T (°C)	**222**		**228**		**243**		**266**		**287**		**294**		**310**		**311**		**354**		**381**		**423**		**449**	
dG (J)	1787.2		1867.9		1724.5		2247.4		1455.3		1342.3		1410.0		1621.5		1847.7		2262.2		2036.1		2266.0	

Table 4. *Results of Quartz-Chlorite-Phengite-H_2O multi-equilibria calculations. Chemical compositions of representative white mica and chlorite mineral pairs which met equilibrium conditions are presented. Equilibrium is considered to be achieved for dG < 2400 J (appendix S3).*

METHODS

P–T conditions and *P–T* paths

The metamorphic conditions and *P–T* paths were constrained by using *P–T* pseudosections (De Capitani & Brown, 1987; Powell *et al.*, 1998; Zeh, 2001; Connolly & Petrini, 2002; Johnson *et al.*, 2008; Millonig *et al.*, 2010) and geothermobarometry with a multi-equilibria method. Mineral compositions were measured using a Cameca SX50 Microprobe at the GET lab in Toulouse, France. P-T pseudosections were constructed using the Perplex software (Connolly, 2005). Pseudosections used to constrain the prograde evolution of migmatite samples were constructed by using an average composition of subsolidus paragneiss (Table 2, Appendix S2). Garnet porphyroblast fractionation was taken into account when its mode was found to be significant (> 1vol%). Methodological details relevant for individual samples are described in Appendix S2, along with the chosen solution models. In addition, the multi-equilibria method (e.g. Berman, 1991) was employed to set further constraints on the *P–T* evolution of low-grade, greenschist- to amphibolite-facies metamorphic rocks. This method is appropriate to constain *P–T* conditions and *P–T* paths of rocks characterised by high variance assemblages (e.g. Vidal *et al.*, 2006 and references therein). Studies on natural metapelite samples have shown that minerals from different microstructural domains (foliations, shear bands, etc) of a single thin section can represent different local equilibria, and therefore reflect different *P–T* conditions (e.g., Vidal *et al.*, 2001, 2006; Parra, 2002; De Andrade *et al.*, 2006; Yamato *et al.*, 2007a; Ganne *et al.*, 2012). The compositions of minerals used for *P–T* calculations are presented in Table S2, and calculation details are given in Appendix S3.

Geochronology

A first set of analyses was performed *in-situ* on polished thin sections of samples BN43, BN47 and BN436, using laser ablation – inductively coupled plasma – sector field – mass spectrometry (LA-ICP(SF)-MS) at Goethe University Frankfurt (Appendix S4). Prior to LA-ICP(SF)-MS, the internal structure of each monazite grain was characterised by raster electron microscopy (REM) at Geosciences Environnement Toulouse using a JEOL SM-6360 OLV Scanning Electron Microscope. A second set of analyses was carried out *in-situ* on polished thin sections of samples BN47 and BN43, using Sensitive High Resolution Ion MicroProbe (SHRIMP II) at the John de Laeter Centre for Isotope Research (JLC), Curtin University, Perth, Australia (Appendix S4). Monazite crystals from sample BN436 were only dated using LA-ICP-MS at GUF.

RESULTS

P–T conditions and *P–T* paths

Sample BN43 (Garnet – kyanite-bearing migmatitic gneiss)

P–T pseudosections for migmatite sample BN43 are presented in Fig. 7, with assemblages and reactions identified in 7d. Subsolidus amphibolite-facies conditions of 6.5-9.5 kbar, 600-670°C are deduced from the compositions of garnet1 (Prp13-17, Grs3-5) and plagioclase located in paleosomes (An 24-26) (Fig. 7b). These conditions overlap with the calculated stability conditions of the metamorphic assemblage Bt + Grt + Pl + Ms + Pg + Rt + Qz between 8.5-9.5 kbar, 650-670°C. This assemblage is identical to assemblage (A) except for rutile, which was not observed and may have totally reacted out. The composition of plagioclase preserved in kyanite (An21-25) is consistent with crossing (R1) at 10.0-11.0 kbar (Fig. 7c,d). The formation of assemblage (B) Grt1 + Bt1 + Ky + Pl + Qz + L requires decompression below 9.0 kbar at 680-750°C. We deduce the shape of the *P–T* path based on constraints drawn from the following observations:

(1) Aluminosilicate mode increases in the stability field of sillimanite.

(2) Garnet2 formation by reaction (R2) represents an increase in garnet mode in the stability field of sillimanite.

Modelling results show that aluminosilicate mode decreases with increasing T (Fig. 7c), hence (1) requires decompression without heating from the stability field of assemblage (B) to that of assemblage (C) Grt1 + Bt1 + Sil1 + Pl + Qz + L, below 7.0-9.0 kbar. Garnet mode increases with increasing T, therefore (2) implies a temperature increase under conditions corresponding to the stability of assemblage (C) (Fig. 7b). Garnet2 crystallisation (which defines assemblage (D)) post-dates or is coeval with monazite crystallisation in neosomes, and corresponds to peak temperature conditions of ~750°C. If H_2O saturation conditions are met on the wet solidus at 10 kbar, melt is generated in sufficient amount at peak T (>5 vol%, Fig. 7d) for it to segregate (e.g. Arzi, 1978; Sawyer, 1994; Brown *et al.*, 1995), inducing open system behaviour (Appendix S2). The absence of cordierite constrains pressure along the retrograde path to be above 5 kbar. This is consistent with the composition of biotite2 (#Mg = 0.51-0.56). Calculation results show that assemblage (E) Grt2 + Bt2 + St + Ilm + Pl + Qz, formed between 4.5-8.0 kbar and <640 °C (Fig. 7d).

Sample BN43 records a clockwise *P–T* path. Prograde burial and heating from amphibolite-facies conditions of about 9.0 kbar, 650°C across the solidus to transitional amphibolite – high-P granulite facies conditions of 10.0-11.0 kbar, 700°C is documented by the evolution from assemblage (A) to (B). Metamorphic conditions at peak P fit a 15-20°C km^{-1} apparent geothermal gradient (calculated for an average density $\rho = 2750$ $kg.m^{-3}$). High-P (>10 kbar) melting is followed by near isothermal decompression to 5.0-8.0 kbar, into the stability field of assemblage (C). The rock then records heating to form assemblage D at the amphibolite – low-P granulite facies transition. Recorded peak conditions of about 750°C fit a hot 30-35°C km^{-1} apparent geotherm. Assemblage (E) testifies of a retrograde metamorphism in the lower amphibolite facies.

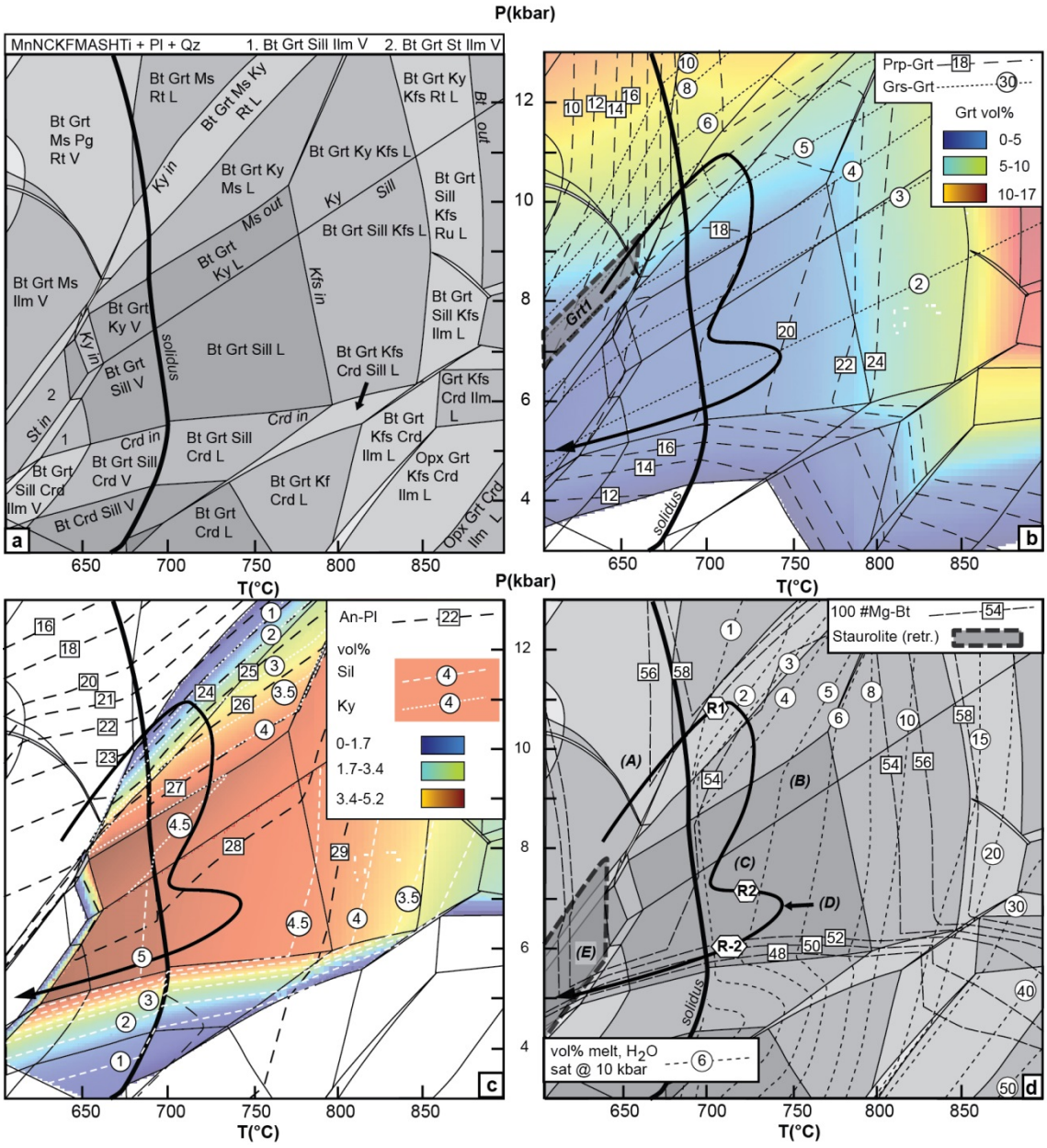

Fig. 7. *MnNCKFMASHTi P-T pseudosections presenting phase equilibria for sample BN43. (a-d) Stable assemblages calculated from an average paragneiss composition (Table 2, Appendix S2). (b) Calculated garnet Prp and Grs content (black dashed lines, numbers in boxes and dotted lines, numbers in circles, respectively) and Grt mode (colour gradient). (c) Calculated Pl An content (black dashed lines, numbers in boxes), and modal proportion of aluminosilicates. (d) Calculated melt fraction (dashed lines, numbers in circles). The shaded domain shows the stability field of retrograde staurolite in assemblage (E), calculated by using whole rock composition of sample BN43, which is suitable to study metamorphic phase relationships during the retrograde evolution of the sample (Appendix S2). Letters (A) to (E) refer to assemblages, and (R1) and (R2) refer to metamorphic reactions identified in the main text. A possible P-T path consistent with observed petrological relationships is shown.*

Sample BN47 (Garnet – kyanite - staurolite schist)

Results of *P–T* pseudosection construction are presented in Fig. 8, with assemblages and reactions identified in 8d. Comparing modelled and measured garnet compositions provides constraints for a prograde evolution at the blueschist – amphibolite facies transition, with increasing T and decreasing P from the nucleation of garnet core (Grt1) at 11-14 kbar, 520-560°C to growth of garnet rim (Grt2) at 9.0-13.0 kbar, 570-600°C (Fig. 8b). The conditions of garnet1 formation correspond to the calculated stability field of the assemblage Chl + Ms + Cld + Pg + Grt1 + Rt. However, assemblage (A) is not fully characterised and only chlorite inclusions are preserved in garnet1. The absence of chloritoid and paragonite may be due to their complete consumption by prograde metamorphic reactions. Garnet2 is predicted to be in equilibrium with staurolite1 (#Mg = 0.15-0.17) at around 11.0 kbar, 600°C (Fig. 8c). These conditions correspond to the stability field of Grt + St + Chl + Ms + Pg + Rt, while assemblage (B) consists of Grt2 + St1 + Ilm + Qz. The discrepancies between the observed and calculated assemblage may be due to the complete consumption of chlorite and white micas, and to the retrogression of rutile to ilmenite during subsequent metamorphic evolution.

Further information on the shape of the *P–T* path may be drawn from the observation that garnet2 is in equilibrium contact with kyanite. Garnet composition and zoning patterns suggest that garnet mode did not increase between assemblage (B) and assemblage (C) Grt2 + Ky + Bt + Pl + Ilm + Qz ± Ms. Figure 8b shows that such an evolution first requires decompression without any temperature increase, into the ilmenite stability field (in agreement with the observation of ilmenite in staurolite1), at < 9.5 kbar >550 °C, followed by near isobaric heating to at least 650°C at 8.0-9.0 kbar, in the amphibolite facies. Monazite is interpreted to have crystallised close to peak temperature conditions. The rock then crossed reaction R1 and developed assemblage (D): Grt2 + St2 + Bt + Pl + Ilm + Qz at 4.0-7.0 kbar, 600-650°C. The modal proportion of staurolite is expected to increase from 2-4 to 16-19 vol% between (B) and (D) (Fig. 8c), in agreement with observations.

Results from *P–T* modelling reveal a clockwise *P–T* path for sample BN47. Garnet cores represent HP-LT metamorphic relics formed near to the transition between the blueschist facies and the epidote amphibolite sub-facies, along a cold ~15°C km^{-1} apparent geothermal gradient. Following near isothermal decompression and near isobaric heating, peak temperature was reached in the amphibolite-facies at conditions that reflect a moderate, ~25°C km^{-1} apparent geotherm.

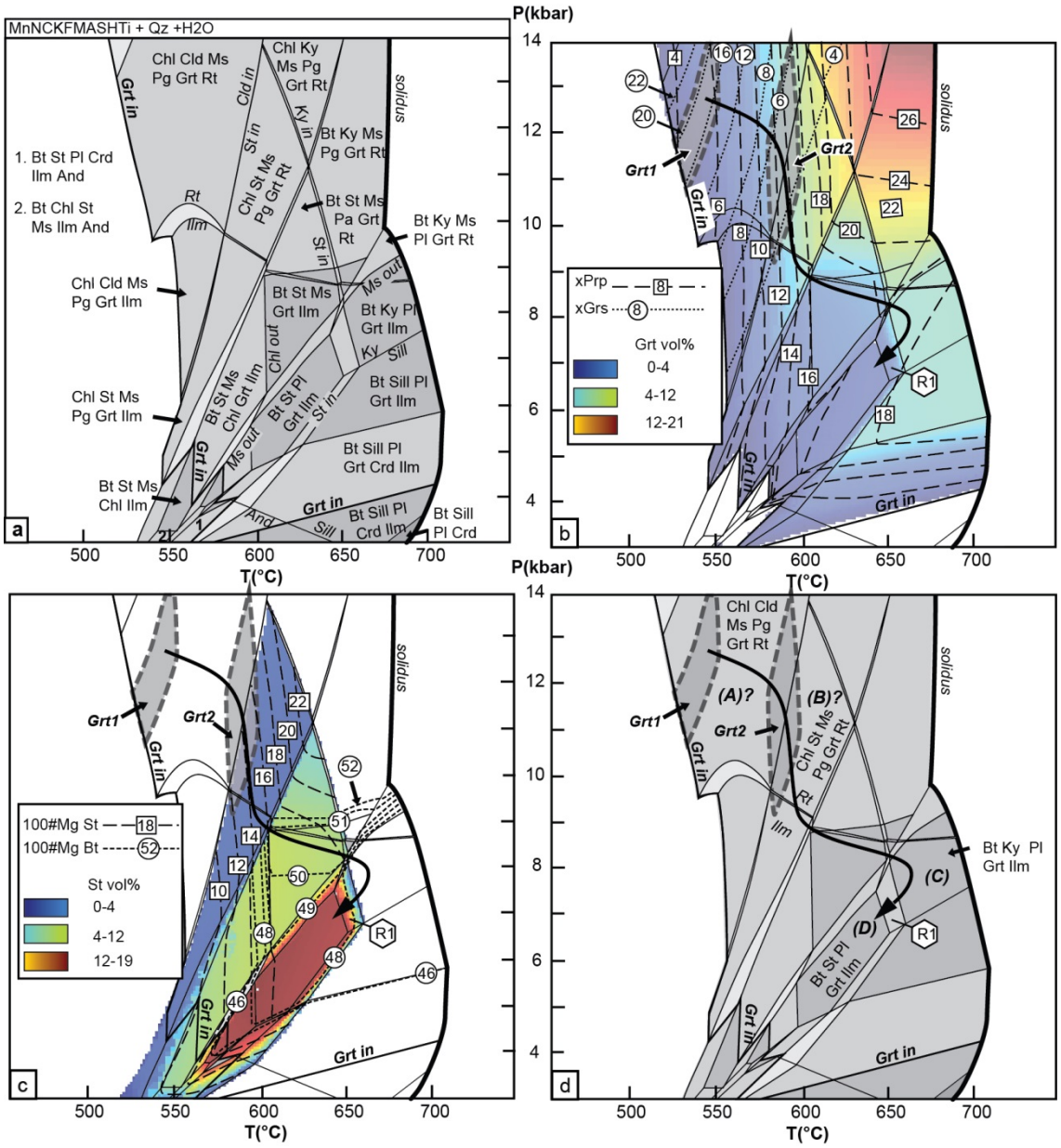

Fig. 8. *MnNCKFMASHTi P-T pseudosections illustrating phase equilbria for metagreywacke sample BN47. (a) Calculated stable assemblages. (b) Calculated garnet Prp and Grs content (black dashed lines, numbers in boxes and dotted lines, numbers in circles, respectively) and garnet mode. The shaded domain represents the P-T fields of garnet1 and garnet2 formation. (c) Calculated biotite and staurolite #Mg (dotted line, number in circles, and dashed line, number in boxes respectively) and staurolite modal proportion. (d) (A-D) and (R1) refer to metamorphic assemblages and reactions identified in the main text. A P-T path consistent with petrological relationships is drawn.*

Sample BN436 (Garnet – kyanite – gedrite granofels)

The coexistence of garnet in equilibrium with rutile and epidote (modelled here as zoisite in the absence of Fe^{3+}, Appendix S2) in assemblage (A) Grt1 + Chl1 + Ep + Rt1 + Qz, implies that the sample crossed the

Grt in reaction at pressures above 7.0 kbar, ~520°C (invariant point ***i***, Fig. 9b). The calculated assemblage Grt + Chl + Zo + Pg + Cld + Rt + Qz is the closest match to assemblage (A), but Cld was not observed, possibly due to complete consumption by prograde metamorphic reactions. The compositions of garnet1 and staurolite1 (Prp 17-20, Grs3-6; and #Mg< 0.10 respectively; dark shaded areas in Fig. 9b) suggest that assemblage (B): Grt1 + Chl1 + St1 + Pl1 + Pg1 + Ilm + Qz, formed at amphibolite-facies conditions of 4.0-6.5 kbar, 550-600°C. Petrological relationships and calculated isopleths therefore provide evidence for a prograde evolution from 7.0-8.0 kbar, ~520°C to 4.0-6.5 kbar, 550-600°C.

Following the formation of assemblage (B), the rock crossed reaction (R1), out of the stability domain of ilmenite (light shaded area in Fig. 9b) into that of rutile. This requires a pressure increase above 7.0 kbar. The formation of plagioclase2 (An50) included in garnet outer cores (Fig. 9b) followed by that of the peak metamorphic assemblage (C): Grt2 + Ged + Ky + Pl3 + Rt2 + Qz ± Bt (light shaded area, Fig. 9d) imply further burial and heating. Peak conditions of 6.5-8.5 kbar, 650-700°C in the upper-amphibolite facies are deduced from the comparison of calculated and measured compositions of garnet2, gedrite and plagioclase3 (Fig. 9c,d). The pseudosection provides a satisfactory explanation for the observed crystallisation sequence of Ti-phases : Rt1 > Ilm > Rt2. Monazite preserved in garnet porphyroblasts crystallised along the prograde path at < 640°C, before the formation of assemblage (C). The absence of cordierite or sillimanite suggests that the rock underwent limited decompression during the retrograde metamorphic overprint. Cooling to <530°C is reflected by the crystallisation of minerals belonging to assemblage (D) Grt2 + Pg2 + Chl2 + St2 + Qz.

Sample BN436 records a complex metamorphic evolution. The early metamorphic assemblage (A) records lower-amphibolite-facies conditions that fit an apparent geotherm of ~20°C km^{-1}. The sample then followed a clockwise *P–T* path that includes a first decompression-heating segment between the stability fields of assemblages (A) and (B), followed by a second burial-heating segment into the field of assemblage (C). Peak *P–T* conditions are reached in the upper-amphibolite facies and correspond to a moderate to warm, ~30°C km^{-1} apparent geothermal gradient. In the absence of post-peak decompression, a tight *P–T* loop is suggested.

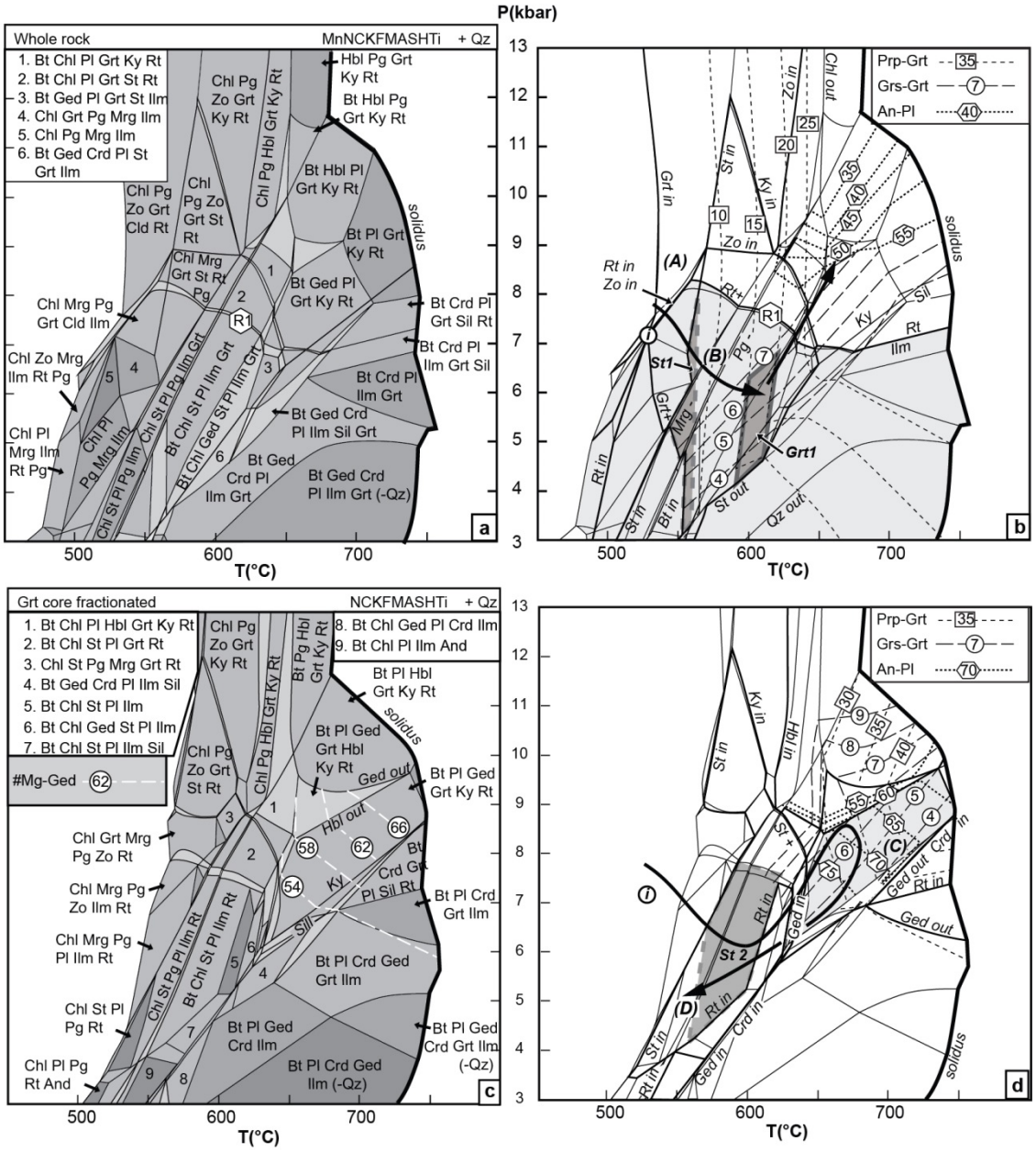

Fig. 9. *P-T pseudosections displaying phase equilibria for sample BN436. (a-b): pseudosections showing metamorphic phase relationships suitable to determine the prograde metamorphic evolution of the sample in the MnNCKFMASHTi system. (c-d) pseudosections presenting phase relationships after garnet fractionation (Table 2, Appendix S2) in the NCKFMASHTi system, suitable for the peak and retrograde metamorphic evolution. (a) Calculated stable assemblages. (b) Light shaded domain represents the ilmenite stability field. Dark shaded areas with dashed and full contours respectively show the conditions of staurolite1 and garnet1 formation. (c) Calculated stable assemblages. (d) Light shaded domain corresponding to the observed peak metamorphic assemblage. Dark shaded box with dashed contour shows formation conditions of staurolite2. Invariant point* ***i*** *represents a minimal P constraint for the coexistence of garnet with zoisite and rutile. Isopleths of garnet Prp and Grs content, and of plagioclase An content are shown, along with a possible P-T path consistent with observations. (A-D) and (R1) refer to metamorphic assemblages and reactions identified in the main text.*

Sample BN185 (volcano-sedimentary schist)

Table 4 shows compositions of white mica and chlorite pairs that formed together at equilibrium, and provides the corresponding equilibrium conditions determined by using the multi-equilibria calculation method presented in Appendix S3. Three compositionally different chlorite-phengite couples, equilibrated in different *P–T* ranges were identified. Low-Si (Si < 2.75 a.p.f.u) chlorite and low-K white mica (K < 0.80) equilibrated at > 300°C and up to 10 kbar (group A). Moderate-Si (2.75 < Si < 2.82) chlorite and moderate-K (0.80 < 0.85) white mica formed between 250 and 300 °C, below 5 kbar (group B). High-Si (Si > 2.82) chlorite and high-K (K > 0.85) white mica equilibrated at < 250°C, below 4 kbar (group C). They together define a near-continuous trend in *P–T* space from ~10 kbar, 450°C, to 1 kbar, 220°C (Fig. 10). Peak metamorphic conditions correspond to an apparent geothermal gradient of ~15°C km^{-1}, at the transition between the greenschist and blueschist facies. The sample was then exhumed along a decompression-cooling path.

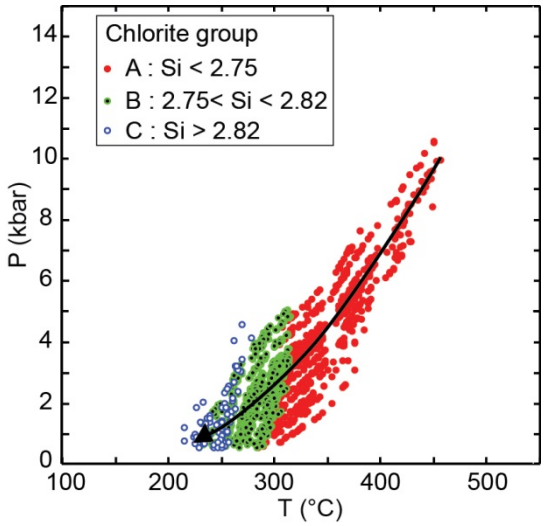

Fig. 10. *P-T diagram presenting the chemical composition of chlorite vs. P-T equilibrium conditions. The black arrow shows a P-T path consistent with multi-equilibria calculations. Each point on the P-T diagram represents equilibrium conditions for one chlorite composition, equilibrated with one white mica composition (Table 4) using the multi-equilibria method described in Appendix S2.*

Sample BN246 (Micaschist)

The overlap of *P–T* conditions obtained independently from the Chl-Qz-H_2O and Ph-Qz-H_2O equilibria provide conditions of possible equilibrium (Appendix S3). For sample BN246, they define an area in *P–T* space ranging from 310-380°C at 2.0 kbar to 420-480°C at 9.5 kbar (Figs. 12 & 13).

Complementary samples

The *P–T* conditions determined for samples BN365, BN491 and BN534 are presented in Appendix S1, Figs. S2 & S3; and are displayed in Figs. 12 & 13. Samples BN365 and BN534 record a supra-solidus evolution at the amphibolite – high-P granulite facies transition, at peak conditions at 10.0-12.0 kbar, 700-800°C; and 9.5-11.5kbar, 680-750°C, respectively. Sample BN491 records prograde burial and heating up to peak amphibolite-facies conditions of 7.5-9.5 kbar, 610-650°C, and a retrograde overprint at 4.0-7.0 kbar, 550-610°C. All samples reveal a clockwise *P–T* evolution.

Geochronology

Sample BN43 (Garnet – kyanite-bearing migmatitic gneiss)

A total of 22 U-Th-Pb LA-ICP-MS spot analyses were carried out on 12 monazite grains from sample BN43. This includes 8 analyses on 4 grains located in leucosomes, 9 analyses on 4 grains located in biotite selvedge, and 5 analyses on 3 grains enclosed in peritectic garnet (Table 5). Some monazite grains are unzoned, while in other grains core zones have a slightly different luminescence (Fig. 11f). These patches were too small to be selectively targeted for ablation. Ten concordant analyses from grains in every textural setting yielded a U-Pb Concordia age of 2137.1±7.6 Ma ($MSWD_{C+E}$ = 0.25, $Probability_{C+E}$=0.99, C+E = concordance and equivalence; Fig. 11a). This result is supported by 17 U-Th-Pb SHRIMP analyses performed on 10 monazite grains located in peritectic garnet2, in neosomes and in the matrix (Table S3). Among them, 9 concordant analyses on 5 monazite grains situated in every textural setting provided an identical within errors Concordia age of 2141.2±6.4 Ma, ($MSWD_{C+E}$=1.3, $Prob._{C+E}$=0.19; Fig. 11b). However, three LA-ICP-MS spots performed on a single grain (grain n°1, Table 5, Fig. 11a) reveal a significantly older imprecise upper intercept age of *c*. 2211±62 Ma (MSWD=0.65, Probability=0.42). The *c*. 2140 Ma Concordia age is interpreted to date melting in sample BN43, during metamorphism at the amphibolite-granulite facies transition, prior to or during garnet2 growth. The *c*. 2210 Ma age may reflect an inherited component in the volcano-sedimentary protolith of the rock.

Sample BN47 (Garnet – kyanite - staurolite schist)

Seventeen U-Th-Pb LA-ICP-MS spot analyses were carried out on four unzoned monazite grains from sample BN47. Among them, 5 analyses were performed on a grain included in a staurolite porphyroblast, 9 on two grains elongated parallel to the metamorphic banding in the matrix (Fig. 11g), and 3 on a grain included in matrix biotite (Table 5). All LA-ICP-MS analyses but one yielded identical $^{207}Pb/^{206}Pb$ ages within errors of *c*. 2130 Ma (weighted mean $^{207}Pb/^{206}Pb$ age = 2127 ±7 Ma; MSWD=1.5, n=16), and eleven of them give a U-Pb Concordia age of 2127.0±7.4 Ma ($MSWD_{C+E}$=0.67, $Prob._{C+E}$=0.87; Fig. 11c). The Concordia age is identical to an upper intercept age of 2130.2±6.4 Ma (MSWD=1.3, Prob.=0.2) obtained

Results of U-Pb LA-ICP-MS dating of monazite carried out in GUF

analysis	grain n°	location	U[b] (ppm)	Pb[b] (ppm)	Th[b] / U	^{206}Pbc[c] (%)	^{206}Pb[d] / ^{238}U	±2s (%)	^{207}Pb[d] / ^{235}U	±2s (%)	^{207}Pb[d] / ^{206}Pb	±2s (%)	rho[e]	^{206}Pb / ^{238}U	±2s (Ma)	^{207}Pb / ^{235}U	±2s (Ma)	^{207}Pb / ^{206}Pb	±2s (Ma)	conc.[f] (%)
sample BN47																				
a06	mnz1	elongated in matrix	7392	4100	1.49	b.d.	0.35400	2.9	6.548	3.2	0.1342	1.4	0.89	1954	49	2052	29	2153	25	91
a07	mnz1		7430	4400	1.54	0.09	0.38980	3.2	7.07	3.6	0.1316	1.5	0.91	2122	59	2120	32	2119	26	100
a08	mnz1		7769	4800	1.71	0.04	0.39140	2.7	7.212	3.1	0.1336	1.4	0.88	2130	49	2138	28	2146	25	99
a09	mnz1	elongated in matrix	10224	5600	1.59	b.d.	0.34930	3.2	6.333	3.4	0.1315	1.1	0.95	1931	54	2023	30	2118	19	91
a10	mnz1		8445	5300	1.84	0.05	0.38880	2.8	7.082	3.2	0.1321	1.6	0.86	2117	50	2122	29	2126	29	100
a11	mnz2	st inclusion	4994	4400	3.32	0.05	0.41810	5.6	7.518	5.8	0.1304	1.5	0.97	2252	107	2175	53	2104	26	107
a12	mnz2	st inclusion	8531	6900	3.13	b.d.	0.39150	2.9	7.2	3.1	0.1334	1.1	0.93	2130	52	2137	28	2143	20	99
a13	mnz2	st inclusion	3554	3100	3.60	b.d.	0.35070	3.3	6.412	3.9	0.1326	2.1	0.83	1938	55	2034	35	2133	38	91
a14	mnz2	st inclusion	7540	6400	3.52	0.02	0.37680	2.9	6.936	3.3	0.1335	1.6	0.88	2061	52	2103	30	2144	28	96
a15	mnz2	st inclusion	5429	4900	3.99	0.18	0.39130	2.8	7.114	3.2	0.1318	1.5	0.88	2129	51	2126	29	2123	26	100
a16	mnz3	in matrix bt	7220	6700	4.13	0.03	0.39500	2.7	7.283	3.0	0.1337	1.3	0.91	2146	49	2147	27	2147	22	100
a17	mnz3	in matrix bt	6876	6400	4.31	0.10	0.38230	2.7	6.755	3.0	0.1281	1.3	0.90	2087	49	2080	27	2073	23	101
a18	mnz3	in matrix bt	6734	5700	3.66	0.07	0.39300	3.0	7.147	3.1	0.1319	0.9	0.96	2137	54	2130	28	2124	15	101
a19	mnz4	elongated in matrix	7490	6600	3.78	0.03	0.39070	2.9	7.063	3.1	0.1311	1.0	0.95	2126	53	2119	28	2113	17	101
a20	mnz4		7696	7100	4.12	0.05	0.39100	3.0	7.133	3.1	0.1323	1.0	0.95	2128	54	2128	28	2129	18	100
a22	mnz4	elongated in matrix	8009	7600	4.23	0.17	0.38740	2.9	7.055	3.1	0.1321	1.1	0.94	2111	52	2118	28	2126	18	99
a23	mnz4		7674	7000	4.10	0.05	0.38990	2.5	7.068	2.8	0.1315	1.1	0.92	2122	46	2120	25	2118	19	100
sample BN43																				
a08	mnz1	leucosome	4965	5500	6.24	0.02	0.35700	3.3	6.819	3.9	0.1385	2.0	0.86	1968	56	2088	35	2209	35	89
a09	mnz1	leucosome	6482	5800	4.73	0.01	0.34140	2.4	6.593	2.8	0.1401	1.5	0.84	1893	39	2058	25	2228	26	85
a10	mnz1	leucosome	5427	4800	4.59	0.03	0.30580	4.2	5.883	5.0	0.1395	2.6	0.85	1720	64	1959	44	2221	46	77
a11	mnz2	in bt selvedge	2059	5800	20.25	0.04	0.39920	3.5	7.361	4.0	0.1338	1.9	0.88	2165	65	2156	36	2148	34	101
a12	mnz2	in bt selvedge	5540	6500	6.67	0.01	0.37500	2.4	6.912	2.7	0.1337	1.2	0.90	2053	42	2100	24	2147	20	96
a13	mnz2	in bt selvedge	1309	6100	34.97	0.13	0.36500	2.3	6.729	2.8	0.1337	1.7	0.79	2006	39	2076	25	2147	30	93
a14	mnz2	in bt selvedge	2146	5200	18.03	b.d.	0.39320	2.2	7.186	2.6	0.1326	1.3	0.86	2137	41	2135	23	2132	23	100
a15	mnz3	in bt selvedge	3467	3200	4.25	0.01	0.39460	2.4	7.216	3.0	0.1326	1.7	0.82	2144	44	2138	27	2133	30	101
a16	mnz4	grt inclusion	1451	1700	6.16	0.02	0.39780	3.9	7.383	5.0	0.1346	3.1	0.79	2159	73	2159	46	2159	54	100
a17	mnz4	grt inclusion	6722	7500	6.37	0.06	0.38410	1.9	6.987	2.2	0.1319	1.1	0.86	2095	34	2110	20	2124	20	99
a19	mnz5	leucosome	2849	3200	5.93	0.07	0.39150	2.2	7.151	2.6	0.1325	1.3	0.87	2130	40	2130	23	2131	23	100
a21	mnz6	in bt selvedge	5627	6600	7.04	0.05	0.37130	2.0	6.743	2.3	0.1317	1.0	0.89	2036	35	2078	20	2121	18	96
a22	mnz6	in bt selvedge	1580	4200	18.60	0.07	0.38840	2.2	7.085	2.6	0.1323	1.4	0.85	2115	40	2122	24	2129	24	99
a28	mnz7	in bt selvedge	3767	6900	12.72	0.04	0.39210	1.9	7.168	2.3	0.1326	1.3	0.82	2133	35	2133	21	2133	23	100
a29	mnz7	in bt selvedge	1700	3700	15.53	0.04	0.39550	1.9	7.292	2.5	0.1337	1.5	0.78	2148	35	2148	22	2147	27	100
a31	mnz8	grt inclusion	5570	6900	7.96	0.02	0.36690	2.1	6.732	2.3	0.1331	1.1	0.89	2015	36	2077	21	2139	18	94
a32	mnz9	leucosome	3653	4000	6.31	b.d.	0.39480	2.7	7.253	3.4	0.1332	2.2	0.78	2145	49	2143	31	2141	38	100
a33	mnz9	leucosome	3379	3900	6.72	0.06	0.39480	2.1	7.24	2.5	0.133	1.5	0.82	2145	38	2141	23	2138	26	100
a34	mnz10	leucosome	1230	1300	5.65	0.17	0.39290	4.0	7.216	4.6	0.1332	2.2	0.87	2136	73	2138	42	2141	39	100

a38	mnz11	leucosome	3304	4000	6.79	0.06	0.39400	2.1	7.207	2.7	0.1327	1.8	0.76	2141	38	2137	25	2134	31	100
a39	mnz12	grt inclusion	941	950	5.23	0.06	0.37730	4.5	6.824	4.9	0.1312	1.9	0.92	2064	80	2089	44	2114	34	98
a41	mnz12	grt inclusion	2857	3400	7.18	0.04	0.39280	2.3	7.194	2.9	0.1328	1.8	0.79	2136	42	2136	26	2136	31	100

analysis	grain n°	location	U^{b} (ppm)	Pb^{b} (ppm)	Th^{b} / U	$^{206}Pbc^{c}$ (%)	$^{206}Pb^{d}$ / ^{238}U	±2s (%)	$^{207}Pb^{d}$ / ^{235}U	±2s (%)	$^{207}Pb^{d}$ / ^{206}Pb	±2s (%)	rho[e]	^{206}Pb / ^{238}U	±2s (Ma)	^{207}Pb / ^{235}U	±2s (Ma)	^{207}Pb / ^{206}Pb	±2s (Ma)	conc.[f] (%)
sample BN436		grt inclusion																		
a44	mnz1		984	5600	41.63	0.02	0.39190	3.0	7.148	3.5	0.1323	1.9	0.84	2131	54	2130	32	2129	33	100
a49	mnz2		531	1200	15.01	b.d.	0.27460	14.7	5.224	16.9	0.138	8.4	0.87	1564	207	1856	155	2202	146	71
a50	mnz3		2227	4400	13.44	0.03	0.39080	2.0	7.08	2.4	0.1314	1.3	0.83	2127	36	2122	22	2117	23	100
a51	mnz4		565	4700	64.15	b.d.	0.39470	1.8	7.214	2.5	0.1325	1.6	0.75	2145	34	2138	22	2132	29	101
a52	mnz4		1030	4700	33.45	b.d.	0.38420	2.4	6.936	2.8	0.1309	1.5	0.85	2096	43	2103	25	2111	26	99
a53	mnz4		716	5100	54.85	0.33	0.39100	2.8	7.14	3.2	0.1324	1.6	0.87	2127	51	2129	29	2131	28	100
a54	mnz5		745	4800	50.30	0.58	0.39180	2.0	7.166	2.5	0.1327	1.5	0.79	2131	36	2132	23	2133	27	100
a55	mnz5		745	4800	48.88	2.75	0.35000	4.8	6.244	5.4	0.1294	2.4	0.89	1935	81	2011	48	2089	42	93
a56	mnz5		648	4800	57.15	0.16	0.39240	2.2	7.183	2.5	0.1328	1.3	0.86	2134	39	2134	23	2135	22	100
a57	mnz5		684	4500	50.41	b.d.	0.39240	2.2	7.124	2.7	0.1317	1.5	0.82	2134	40	2127	24	2120	27	101
a58	mnz5		1067	5200	37.07	b.d.	0.39310	2.0	7.161	2.3	0.1321	1.1	0.89	2137	37	2132	21	2127	18	100
a59	mnz6		840	5000	44.35	0.11	0.39190	2.1	7.145	2.4	0.1322	1.3	0.85	2132	37	2130	22	2128	22	100
a60	mnz6		775	4200	41.68	0.01	0.39180	2.1	7.155	2.7	0.1325	1.6	0.79	2131	39	2131	24	2131	29	100
a61	mnz7		1021	3700	24.93	0.05	0.39240	3.5	7.16	3.9	0.1323	1.8	0.88	2134	63	2132	36	2129	32	100
a62	mnz7		1146	3100	18.80	b.d.	0.39220	2.8	7.2	3.1	0.1332	1.3	0.91	2133	51	2137	28	2140	23	100
a63	mnz8		980	1500	9.50	0.28	0.36770	5.2	6.416	6.1	0.1266	3.3	0.84	2018	90	2034	55	2051	59	98
a64	mnz9		1032	2600	18.41	b.d.	0.39500	2.1	7.215	2.4	0.1325	1.2	0.87	2146	38	2138	22	2131	21	101
a65	mnz10		790	3000	26.46	b.d.	0.39300	3.0	7.133	3.6	0.1316	1.9	0.85	2137	55	2128	32	2120	33	101
a66	mnz10		843	3300	28.02	b.d.	0.39510	2.4	7.211	3.1	0.1324	2.0	0.76	2146	43	2138	28	2130	35	101
a67	mnz11		806	4600	41.54	0.11	0.39560	2.5	7.261	2.9	0.1331	1.5	0.86	2149	45	2144	26	2140	26	100
a68	mnz11		541	4600	62.79	0.06	0.39520	2.5	7.22	3.1	0.1325	1.9	0.80	2147	46	2139	28	2131	33	101

[a]Within run background-corrected mean ^{207}Pb signal in cps (counts per second).

[b] U and Pb content and Th/U ratio were calculated relative to GJ-1 reference zircon.

[c] percentage of the common Pb on the ^{206}Pb. b.d. = below dectection limit.

[d] corrected for background, within-run Pb/U fractionation (in case of $^{206}Pb/^{238}U$) and common Pb using Stacy and Kramers (1975) model Pb composition and subsequently normalised to GJ-1 (ID-TIMS value/measured value); $^{207}Pb/^{235}U$ calculated using $^{207}Pb/^{206}Pb/(^{238}U/^{206}Pb*1/137.88)$

[e] rho is the $^{206}Pb/^{238}U/^{207}Pb/^{235}U$ error correlation coefficient.

[f] degree of concordance = $^{206}Pb/^{238}U$ age / $^{207}Pb/^{206}Pb$ age x 100

Table 5. *U–Pb isotopic data obtained by LA–ICP(SF)–MS analyses at Goethe University Frankfurt, Germany.*

by SHRIMP on 18 monazite grains (Table S3; Fig. 11d) enclosed in kyanite porphyroblasts or found in the matrix. The *c*. 2130 Ma age is interpreted to date the peak of the amphibolite-facies metamorphic overprint, which is reflected by assemblage (C) in sample BN47.

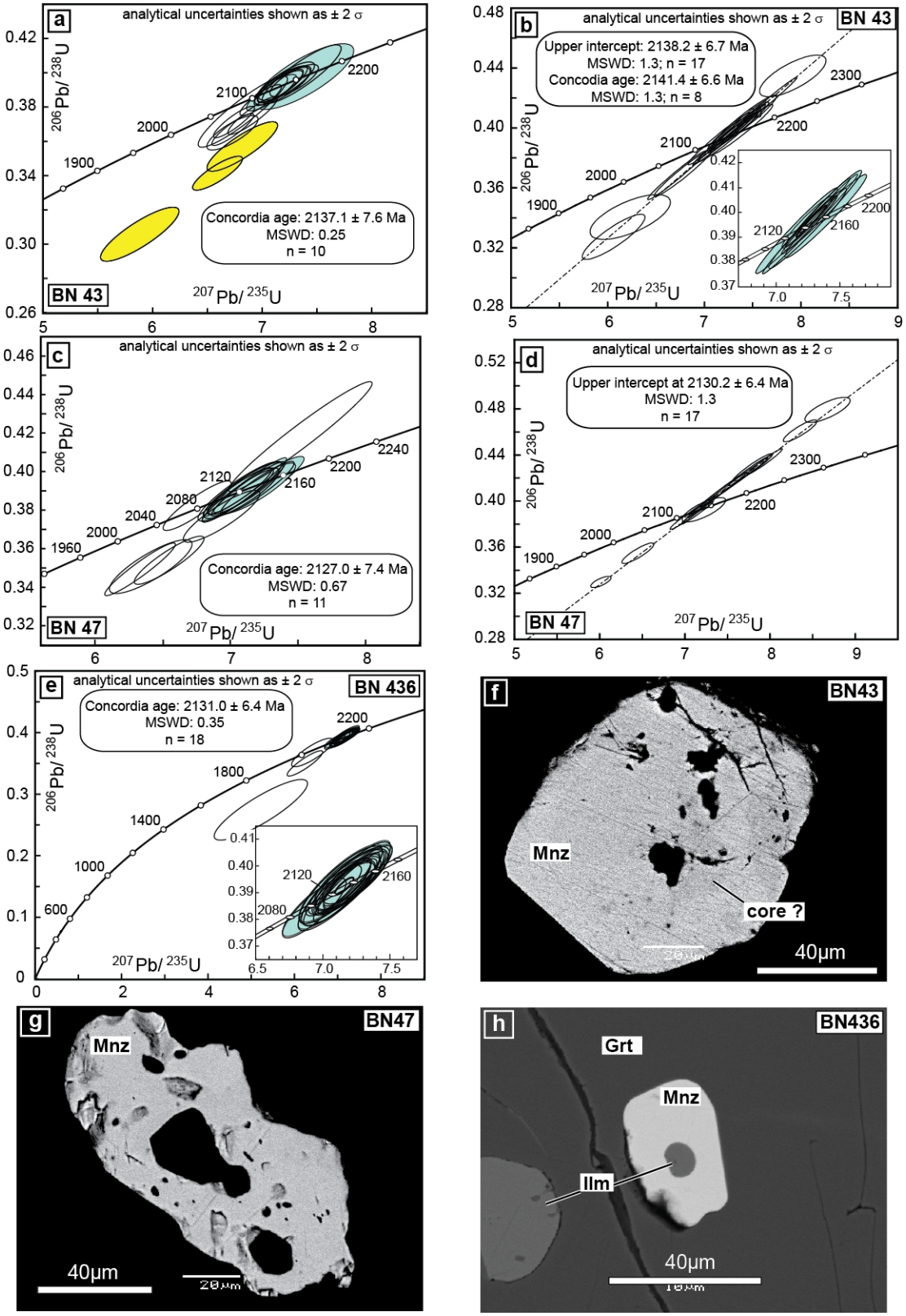

Fig. 11. *(a-e): Results of U-Pb dating of monazite of samples BN43, BN47 and BN436, presented in Concordia diagrams. Errors include decay constant uncertainties. (a, c, e): Results of U-Pb dating by LA-ICP-(SF)-MS. (b, d): Results of U-Pb dating by SHRIMP method. Shaded ellipses represent concordant analyses used for Concordia age calculation. Yellow ellipses in (a) show results of spot analyses from an inherited grain that yielded an older age. (f-h): Back-scattered electron images. (f) Monazite grain in a neosome in sample BN43. It displays very slight luminescence variations between bright rims and a darker core zone. (g) Monazite grain devoid of zoning and containing quartz inclusions, elongated parallel to the fabric in the matrix of sample BN47. (h) Unzoned monazite grain included in garnet and containing an ilmenite inclusion in sample BN436.*

Sample BN436 (Garnet – kyanite – gedrite granofels)

Twenty-one U-Th-Pb laser spot analyses were carried out on 11 monazite grains devoid of any chemical zoning and located in garnet porphyroblats of sample BN436. Eighteen of these analyses yielded a U-Pb Concordia age of 2131.0±6.4 Ma ($MSWD_{C+E}$ = 0.35, $Probability_{C+E}$=0.99, Fig. 11e). The presence of ilmenite inclusions in monazite suggests that monazite formed at the same time as assemblage (C) (Fig. 11h). This age is therefore interpreted to date prograde metamorphism in sample BN436.

DISCUSSION

Metamorphic synthesis

Figure 12 presents a simplified spatial distribution of metamorphic facies, based on field mapping, along with *P–T* conditions and *P–T* paths of the studied samples. The variability of metamorphic conditions across the area is interpreted as documenting four distinct sets of conditions and *P–T* paths (Figs. 12 & 13).

1. An early metamorphic phase developed under a relatively cool (15°C km^{-1}) setting, close to the greenschist-blueschist facies boundary at 8.0-10.0 kbar and 400-500°C (BN185; Fig. 12a); or (BN47; Fig.12c) at 11.0-14.0 kbar, 520-560°C at the transition between the blueschist facies and the epidote-amphibolite sub-facies.

2. Melting at the granulite-amphibolite facies transition is developed in the Bole-Bulenga domain at 8.0-12.0 kbar, with peak temperatures of 700-800°C reached close to the peak pressure (BN534, BN365; Fig. 12b,f), or following a period of isothermal decompression (BN43; Fig. 12d).

3. A regional scale amphibolite facies overprint in the Bole-Bulenga and Abulembire domains of the older HP-LT relicts and granulites. Coeval peak pressures and temperatures of 6.0-9.0 kbar and 550-680°C were obtained under an apparent thermal gradient of 30°C km^{-1} (BN491 & BN436; Fig. 12e,h). This event followed an exhumation phase that is suggested by isothermal decompression paths in rocks metamorphosed at higher pressure (BN47; Fig. 12c).

4. Greenschist facies developed in the Maluwe domain (BN246; Fig. 12g) reaching 2.0-9.5 kbar and 310-480°C.

In high-grade metamorphic domains, the *P–T* paths of the samples merge at 5.0-8.0 kbar, 550-650°C (Fig. 13), which corresponds to conditions of the amphibolite-facies metamorphic overprint. This evolution documents a change in the thermal regime of the crust. It may be interpreted as the result of thermal re-equilibration of the various high-grade units which were tectonically assembled in the lower crust (England & Thompson, 1984) along a ~30°C km^{-1} apparent geotherm (Fig. 13). However, the amphibolite-facies regional metamorphic overprint is not documented in sample BN185. The overprint may have been spatially limited to the Bole-Bulenga and Abulembire domains, allowing the preservation of the early metamorphic evolution characterised by a cold apparent geotherm elsewhere. Alternatively, both cool and warm metamorphic settings may be coeval and represent distinct geodynamic settings.

In any case, the metamorphic record of the Paleoproterozoic craton of north-western Ghana shows that low-grade and high-grade rocks are juxtaposed (Fig 12 & 13). The coexistence of diverse *P–T* paths and *P–T* conditions at regional scale implies that rock units forming the Eburnean crust witnessed evolutions in contrasting thermal environments before the final amalgamation and stabilisation of this part of the craton.

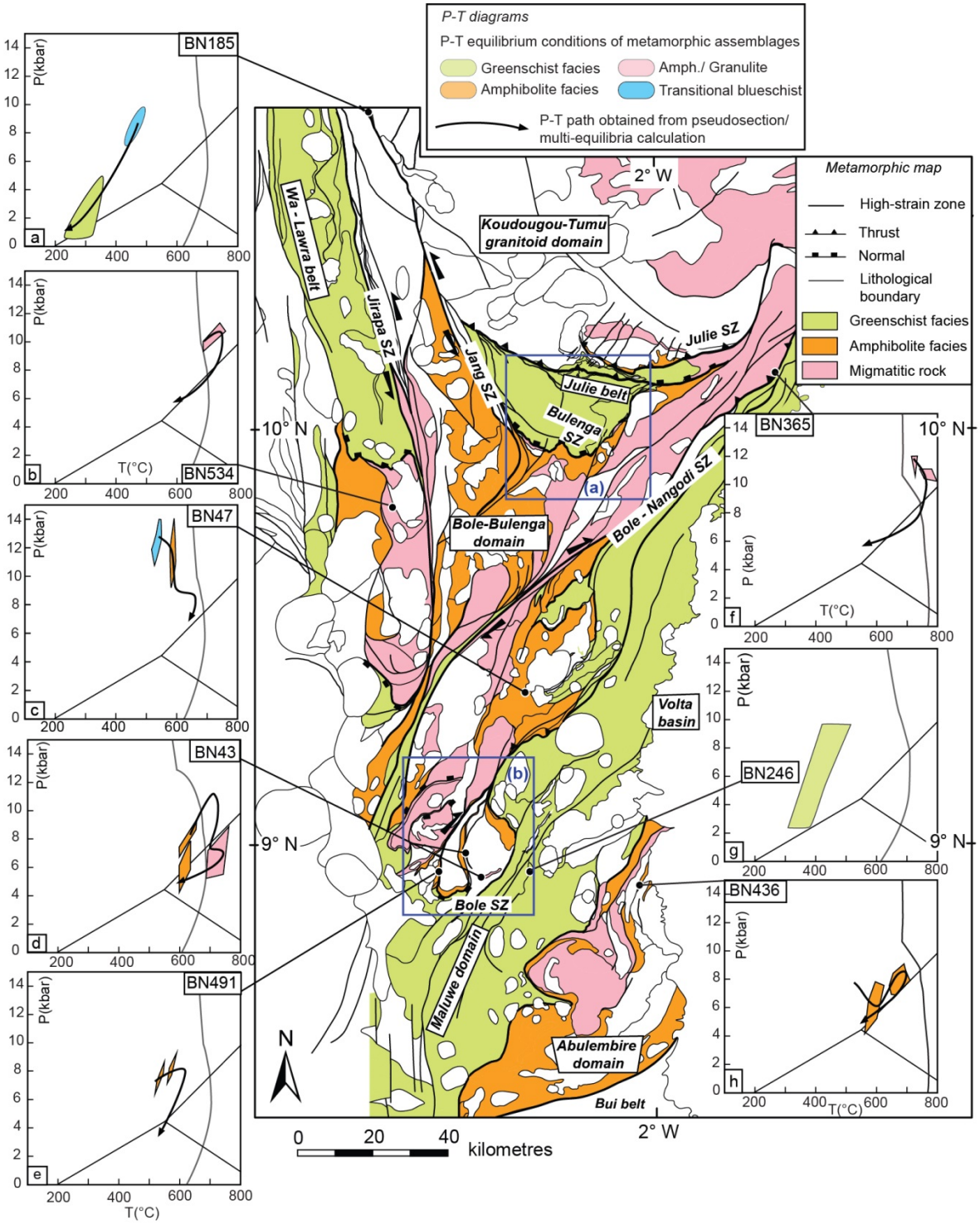

Fig. 12. *Metamorphic map of north-western Ghana showing the position of studied samples, the corresponding schematic P-T diagrams, and the spatial distribution of metamorphic facies. Blue boxes (a) and (b) refer to detailed maps in Fig. 14. Colored fields in P-T diagrams are deduced from P-T pseudosections or multi-equilibria calculations. They represent equilibrium conditions for the formation of specific minerals or assemblages which serve as constraints to P-T paths.*

Regional evolution

Partial melting and metamorphism at the amphibolite-granulite facies transition or in the upper-amphibolite facies are recorded in gneisses of both the Abulembire and Bole-Bulenga domains, between 2145 and 2120 Ma. This suggests that they belonged to the same crustal slice at that time. It was not possible to date the early metamorphic phase that formed the HP-LT relics in a relatively cool (~15°C km^{-1}) environment. These rocks could have followed a continuous evolution from blueschist-facies to high-T amphibolite facies with increasing T and decreasing P during a single burial-exhumation cycle. Conversely, based on our data, we cannot exclude that HP-LT metamorphism and anatexis represent two discrete metamorphic events.

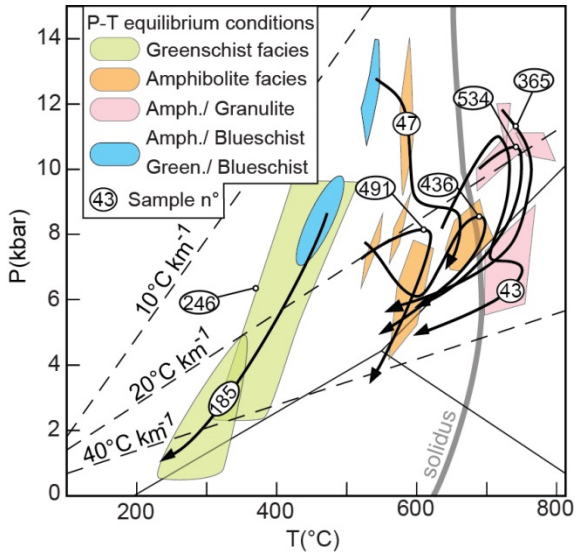

Fig. 13. *Synthesis of P-T conditions and P-T paths deduced from the investigated samples. Individual samples are labelled and are identified from Fig. 12. They reveal a wide range of metamorphic facies and apparent geothermal gradients.*

Agyei Duodu et al. (2009) obtained a crystallisation age of 2196±1 Ma from rhyolitic pyroclastites from the low-grade Maluwe domain. It is identical within errors to the crystallisation ages of orthogneisses intrusive the high-grade paragneisses of the Bole-Bulenga domain (De Kock *et al.*, 2011). This constraint indicates that the rocks in both high-grade and low-grade domains formed prior to the orogeny that generated high-grade metamorphism. We infer from this that the metamorphic breaks across the study area are the result of the tectonic juxtaposition of coeval units, which represent different slices of the same orogen. Furthermore, De Kock *et al.*, (2011) obtained crystallisation ages of 2131±4 Ma from lapilli tuff interbedded with greywacke in the Maluwe domain, indicating synchronous volcanic activity and crustal anatexy. Consequently, we consider that the term "basin" is inadequate to qualify the Maluwe tectono-metamorphic domain, as there is no basin-basement relationship between the Maluwe and Bole-Bulenga rocks. The Maluwe domain rather represents a shallow crustal slice of the Eburnean orogen, which did not witness much burial. A similar conclusion could be drawn for the low-grade units of the Wa-Lawra belt, based on the maximum deposition ages of 2139±2 Ma obtained for volcano-sedimentary rocks located to the West

of the Jirapa shear zone (Agyei Duodu *et al.,* 2009). The 2145-2120 Ma age for high-grade, near-peak T metamorphism overlaps with the crystallisation age of intrusive TTGs and monzogranites in the Bole-Bulenga and Maluwe domains. The granitoids crystallised between 2120 and 2115 Ma are volumetrically significant (De Kock *et al.,* 2011. 2012), but no migmatites with similar metamorphic ages have been found. This suggests that partial melting possibly propagated in the lower crust after 2120 Ma, with the migmatite front migrating downwards from the current-day exposed surface.

Our results show that the study area displays different crustal levels, belonging to the same Paleoproterozoic orogenic crust, metamorphosed in a wide range of thermal environments ranging from the greenschist facies to the amphibolite-granulite facies transition, before being tectonically juxtaposed. These conclusions do not support the polycyclic orogenic model for this portion of the West African Craton. They are also at odds with the vast isobaric domains and high dT/dP thermal regimes reported from Precambrian accretionary belts (Sandiford, 1989, Percival & Skulski, 2000), which are considered to be typical of "hot" orogens (Cagnard *et al.,* 2006, Gapais *et al.,* 2009).

Burial and exhumation

This study reveals that supracrustal rocks were buried in the lower crust, at up to 13.0 kbar, and along a ~15°C km^{-1} apparent geotherms. This pressure corresponds to a ~45 km depth, which represents a minimum thickness for the crust at that time. In modern orogens, such thermal conditions are met in accretionary prisms and during the early stages of crustal thickening, before thermal relaxation of the thickened crust (e.g. Stöckhert & Gerya, 2005, Yamato *et al.,* 2007b). Burial of rocks metamorphosed under these conditions is attributed to thrusting and crustal thickening, while exhumation is proposed to be driven by boundary tectonic forces and prism corner flow (e.g. Burov & Yamato, 2008). In north-western Ghana, early thrust zones (D1) brought in contact different metamorphic units and have some control on the present-day distribution of metamorphic grades (Fig. 12). We propose that D1 thrusting can account for the documented crustal thickening and burial of superficial rocks. Heterogeneous crustal thickening induced by thrusting is expected to cause localised uplift and erosion, which may significantly contribute to remove the overburden above lower-crustal rocks (e.g. England & Molnar, 1990; Platt, 1993). This is in agreement with the limited occurrence of syn-tectonic sedimentary basins containing immature polymictic sedimentary rocks, which suggests that erosion played a role in exhumation.

Following peak P conditions, clockwise *P–T* paths of the investigated high-grade metamorphic rocks frequently display alternating segments with a negative dP/dT, and segments of near-isothermal decompression. Increasing T during decompression requires a low exhumation rate relative to the thermal relaxation rate of the thickened crust (England & Thompson, 1984). Contrastingly, near isothermal decompression reflects a deflection of isotherms towards the surface and rapid exhumation due to tectonically-driven removal of the overburden (e.g. Duchêne et al.,

1997). In modern orogenic belts, partially molten lower-crustal rocks are frequently exhumed in anatectic migmatite domes (Rey *et al.*, 2001; Vanderhaeghe & Teyssier, 2001; Whitney *et al.*, 2004; Vanderhaeghe *et al.*, 2009) where they record supra-solidus isothermal decompression (e.g. Rey *et al.*, 2009). These structures develop during the extensional gravitational collapse of over-thickened orogens, and provide an efficient tectonic mechanism to remove the overburden on top of lower-crustal rocks.

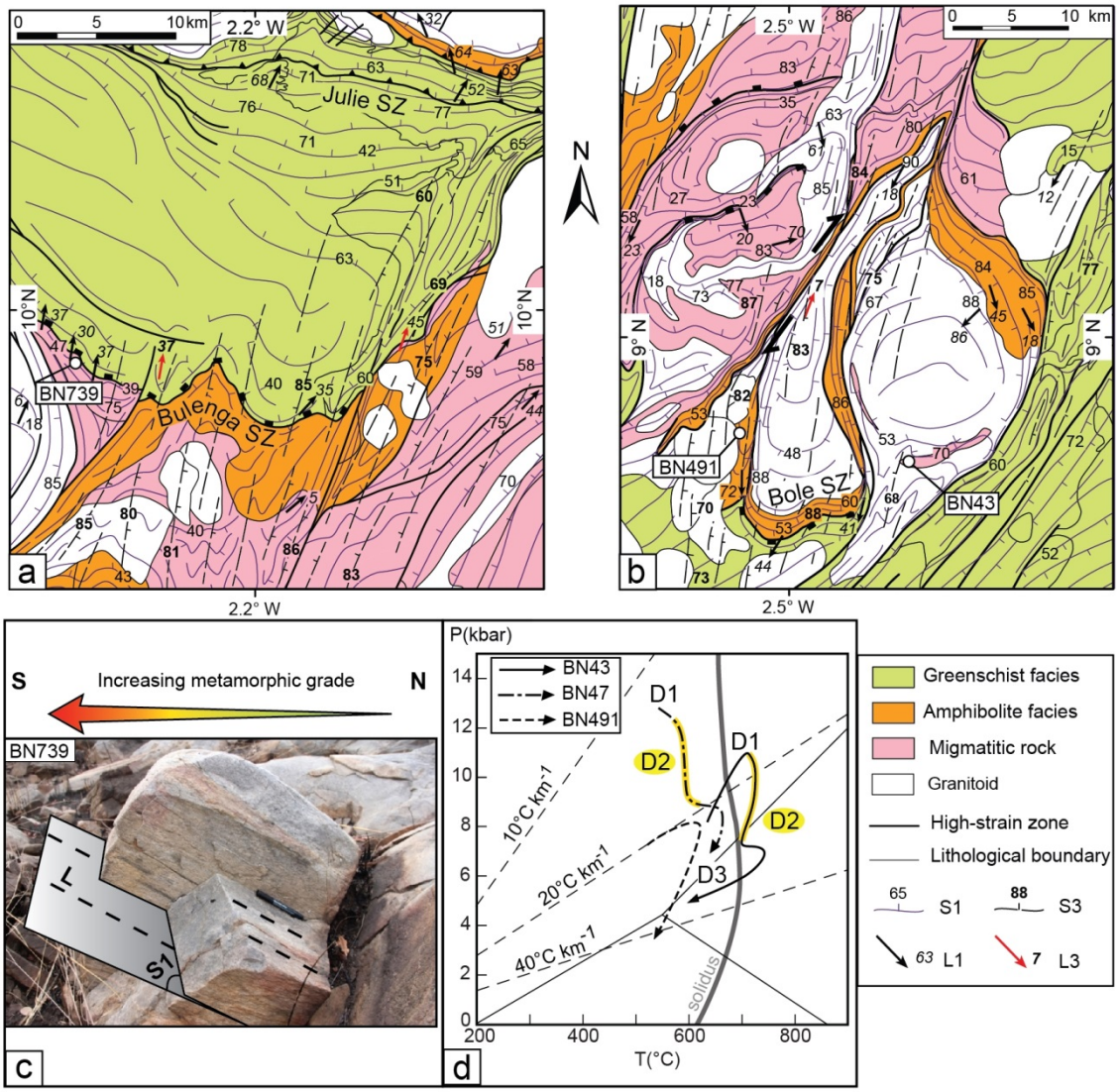

Fig. 14. *(a, b) Structural-metamorphic maps of the northern and southern terminations of the Bole-Bulenga domain, delimited by the Bulenga and Bole shear zones respectively (Fig. 12). Small spacing between S1 foliation trajectory lines illustrates high strain intensity. (c) Outcrop from the Bulenga extensional shear zone displaying a shallow-dipping high-strain fabric and down-dip mineral stretching lineations, plunging towards decreasing metamorphic grade. (d) P-T diagram illustrating various P-T paths obtained from rocks of the Bole-Bulenga domain. Segments attributed to exhumation during extensional deformation D2 are highlighted.*

In north-western Ghana, high-grade, partially molten rocks are bounded by the the Bole and Bulenga extensional shear zones (Fig. 14a,b). These structures are parallel to the trajectories of the early ubiquitous foliation S1 which, in the gneisses, carries high-grade mineral assemblages. The shear zones contain high strain rocks and form metamorphic breaks at the transition between migmatitic gneisses and low-grade metamorphic rocks (Fig. 14c). Such structures are coeval with metamorphism and localised deformation during N-S directed stretching (D2). They exhumed the lower crust against rock units metamorphosed at shallower depths. The *P–T* paths of samples BN43 and BN47 have segments that are consistent with tectonic exhumation during extension (Fig. 14d, highlighted segments). However, sample BN491 (Fig 14d, Appendix S1), which is located across the Bole shear zone from samples BN43 and BN47, has a different *P–T* path. A decompression-cooling path follows peak pressure. This suggests that exhumation dynamics may be variable. Extension is probably significant, but it is not the only process responsible for the exhumation of the lower crust.

The thrusts and the extensional shear zones are strongly overprinted by subsequent deformation (D3), consistent with east-west directed shortening (Fig. 14a,b). Pre-existent tectonic contacts, metamorphic gradients and isograds are folded and transposed into sub-vertical shear zones striking N to NE. Early fabrics (S1 and S2) are overprinted by a sub-vertical, penetrative schistose cleavage striking to the north (S3). Strong metamorphic gradients are observed across D3 shear zones and large (km-scale) folds. We argue that post-extension (D2) exhumation of high-grade rocks below 6 kbar occurred during D3, in a crust dominated by a compressional to transpressional deformation during E-W bulk shortening.

Implications for Precambrian accretionary orogens.

The Paleoproterozoic craton of NW Ghana displays a close association of high-grade metamorphic domains, comprising rocks metamorphosed at the amphibolite-granulite facies transition, juxtaposed with coeval low-grade upper crustal slices. The variability of metamorphic conditions cannot be reconciled with a stable, steady-state, spatially and temporally homogeneous thermal regime. Furthermore, *P–T* paths displaying decompression at constant or increasing temperature cannot be interpreted as the result of homogeneous slow exhumation of vast units in a large and flat orogen (Gapais *et al.*, 2009). The metamorphic record is more consistent with high exhumation rates, structurally-driven horizontal and vertical movements and differential exhumation in the crust, generating major lateral baric metamorphic gradients. Coupled metamorphic and structural data support the view that extensional detachments developed in a thickened, partially molten orogenic crust and contributed to the exhumation of high-grade rocks. Evidence for this crustal mechanical behaviour has not been reported from the Paleoproterozoic West African Craton so far, and evidence for extensional detachments are lacking in Precambrian accretionary orogens in general.

The coexistence of metamorphic terranes recording diverse geothermal gradients implies the existence of regional-scale heterogeneities in the thermal evolution of maturing crusts. Similar to modern orogens, the source of such thermo-mechanical variations may lie in the large-scale architecture of the Eburnean orogen (Hyndman *et al.,* 2005; Moresi *et al.,* 2014), which remains an active research topic. The metamorphic diversity and heterogeneity of ancient orogens is increasingly recognised. Relics of high-P metamorphism are reported from the Minto Block, Canada, which was previously considered to be a very large and homogeneous high-T, low-P granulite province (Percival & Skulski, 2000). Eclogites – high-pressure granulites reported from various Paleoproterozoic orogenic belts (e.g. Möller *et al.,* 1995; Anderson *et al.,* 2012) reflect a broadening range of tectono-metamorphic environments at this period (Brown *et al.,* 2007). Harley (1992) shows that the metamorphic record of Proterozoic granulites requires multiple geodynamic settings. It further demonstrates that significant variation in peak metamorphic pressure and in *P–T* paths are found within individual provinces. The complex metamorphic evolution of the Superior province has been interpreted as the result of the diachronous accretion of thermally heterogeneous crustal fragments (Easton, 2000). Similarly, the existence of non-unique settings for Archean crustal growth and craton-building has been proposed by various authors, based on structural-metamorphic constraints (e.g. in the Yilgarn craton, Goscombe *et al.*, 2009) or on geochemical and petrological arguments (e.g. Moyen *et al.,* 2011, Bedard *et al.,* 2013). The secular change of the Earth's thermal regime is well documented by the metamorphic record. The coexistence of distinct thermal environments is proposed to reflect the onset of some kind of plate tectonics (Brown, 2007, 2009 and references therein) during or after the Neoarchean. In this sense, we suggest that the metamorphic record of the West African Craton is representative of the geodynamic settings at work in a Paleoproterozoic "proto-plate tectonic regime".

CONCLUSION

We recognise contrasting metamorphic patterns from juxtaposed terranes in an interference zone between two craton-scale ductile shear zones, in the Paleoproterozoic West African craton, in NW Ghana. The range of metamorphic data illustrates heterogeneous thermal conditions in the juvenile crust at an early stage of its tectono-metamorphic evolution, prior to final accretion and thermal re-equilibration. Strong lateral metamorphic gradients are interpreted to result of the exhumation of the lower crust; and of the tectonic assembly of distinct crustal slices, which underwent coeval evolutions at different depths. Extensional detachments localised deformation in a thickened, partially molten crust and contributed to the exhumation of high-grade rocks. The diversity of geothermal environments at the scale of the study area is consistent with the spatial variations in metamorphic conditions recorded across the southern West African Craton. The Paleoproterozoic craton in north-western Ghana provides an exceptionally clear window on the lower crust of the Eburnean orogen, and in this sense, it is key to the understanding of Eburnean geodynamics.

We interpret the metamorphic record of NW Ghana as being the product of a monocyclic orogenic evolution that brought in contact the exhumed lower-crust with middle and upper crustal units. This view represents a working hypothesis that deserves testing in other regions of the West African Craton, in order to re-interpret the significance of metamorphism during the Eburnean orogeny. In any case, we emphasise that the "hot orogeny" model, proposed to account for homogeneous, near isobaric metamorphic conditions across large domains recording low-dP/dT apparent geothermal gradients, is not the only model for Paleoproterozoic accretionary orogens.

ACKNOWLEDGEMENTS

We gratefully acknowledge AMIRA International and the industry sponsors, including AusAid and the ARC Linkage Project LP110100667, for their support of the WAXI project (P934A). We acknowledge the facilities, and scientific and technical assistance of the Australian Microscopy & Microanalysis Research Facility at the Centre for Microscopy, Characterization & Analysis of UWA, a facility funded by the University, State and Commonwealth Governments. We thank Erwann Lebrun and the staff of the John De Laeter Centre for Isotope Research, hosted at Curtin University of Technology. Dominique Chardon is warmly thanked for sharing advice and constructive discussions, which contributed to greatly improve the quality of the manuscript. Allen Kennedy is thanked for providing expertise concerning SHRIMP dating. We thank Philippe de Parseval and Sophie Gouy for their assistance for micro-analysis acquisition. We recognise the logistical support and datasets provided by the Geological Survey Department of Ghana, as well as the chauffeurs from the IRD in Ouagadougou (Salifou Yougbaré, Boukary Ouedraogo and Matthieu Kaboré) and from the GSD of Ghana (Kwasi Duah).

REFERENCES

Abouchami, W., Boher, M., Michard, A. & Albarede, F., 1990. A major 2.1 Ga event of mafic magmatism in West Africa; an early stage of crustal accretion. *Journal of Geophysical Research*, B, Solid Earth and Planets **95**, 17, 605–617, 629.

Affaton, P., Sougy, J. & Trompette, R., 1980. The tectono-stratigraphic relationships between the upper Precambrian and lower Paleozoic Volta Basin and the pan-african Dahomeyide orogenic belt (West Africa). *American Journal of Science*, **280**, 3, 224-248.

Agyei Duodu, J., Loh, G.K., Boamah, K.O., Baba, M., Hirdes, W., Toloczyki, M. & Davis, D.W., 2009. Geological map of Ghana 1:1 000 000. Geological Survey Department of Ghana (GSD).

Allibone, A., McCuaig, T.C., Harris, D., Etheridge, M., Munroe, S. & Byrne, D., 2002. Structural controls on gold mineralization at the Ashanti Gold Deposit, Obuasi, Ghana. *Society of Economic Geologists (Special Publication)* **9**, 65–93.

Anderson, J. R., Payne, J. L., Kelsey, D. E., Hand, M., Collins, A. S. & Santosh, M., 2012. High-pressure granulites at the dawn of the Proterozoic. *Geology*, **40**, 5, 431-434.

Arnould, M., 1961. Etude géologique des migmatites et des granites précambriens du nord-est de la Côte d'Ivoire et de la Haute-Volta méridionale. Mémoires du BRGM, 176pp.

Arzi, A. A., 1978. Critical phenomena in the rheology of partially melted rocks. *Tectonophysics*, **44**, 1, 173-184.

Attoh, K., Evans, M. J. & Bickford, M. E., 2006. Geochemistry of an ultramafic-rodingite rock association in the Paleoproterozoic Dixcove greenstone belt, southwestern Ghana. *Journal of African Earth Sciences*, **45**, 333-346.

Baratoux, L., Metelka, V., Naba, S., Jessell, W.M., Gregoire, M. & Ganne, J., 2011. Juvenile paleoproterozoic crust evolution during the Eburnean orogeny (−2.2-2.0 Ga), western Burkina Faso. *Precambrian Research*, **191**, 18–45.

Bard, J.P. & Lemoine, S., 1976. Phase tectoniques superposes dans les métasédiments précambriens du domaine côtier occidental de la Côte-d'Ivoire. *Precambrian Research*, **3**, 209-229.

Berman, RG., 1991. Thermobarometry using multi-equilibrium calculations: a new technique, with petrological applications. *Canadian Mineralogist*, **29**, 833-855.

Block, S., Moyen, J. F., Zeh, A., Poujol, M., Jaguin, J. & Paquette, J.-L., 2013. The Murchison greenstone belt, South Africa: accreted slivers with contrasting metamorphic conditions. *Precambrian Research*, **227**, 77-98.

Brown, M., 2009. Metamorphic patterns in orogenic systems and the geological record. In: Cawood PA, Kroner A (eds) Earth accretionary systems in space and time. *The Geological Society, London, Special Publications*, **318**, 37–74

Brown, M., 2007. Metamorphic conditions in orogenic belts: a record of secular change. *International Geology Review*, **49**, 193–234

Brown, M., 2002. Retrograde processes in migmatites and granulites revisited. *Journal of Metamorphic Geology*, **20**, 25-40.

Brown, M., Averkin, Y.A., McLellan, E.L. & Sawyer, E.W., 1995. Melt segregation in migmatites. *Journal of Geophysical Research: Solid Earth*, **100**, B8, 15 655–15 679.

Boher, M., Abouchami, W., Michard, A., Albarède, F. & Arndt, N. T., 1992. Crustal growth in West Africa at 2.1 Ga. *Journal of Geophysical Research: Solid Earth*, **97**, B1, 345-369.

Bohlen, S.R., & Liotta, J.J., 1986. A barometer for garnet amphibolites and garnet granulites. *Journal of Petrology*, **27**, 1025-1034.

Bonhomme, M., 1962. Contribution à l'étude geochronologique de la plate-forme de l'Ouest Africain. Annals de la Faculte des Sciences de Université de Clermont- Ferrand. *Geologie Minerale*, **5**, 62.

Burov, E. & Yamato, P., 2008. Continental plate collision P–T–t–z conditions and unstable vs. stable plate dynamics: Insights from thermo-mechanical modelling. *Lithos*, **103**, 178-204.

Caby, R., Delor, C. & Agoh, O., 2000. Lithology, structure and metamorphism of the Birimian formations in the Odienné area (Ivory Coast): the major role played by plutonic diapirism and strike-slip faulting at the border of the Man Craton. *Journal of African Earth Sciences*, **30**, 351-374.

Cagnard, F., Gapais, D. & Barbey, P., 2007. Collision tectonics involving juvenile crust: the example of the southern Finnish Svecofennides. *Precambrian Research*, **154**, 125-141.

Cagnard, F., Durrieu, N., Gapais, D., Brun, J. P. & Ehlers, C., 2006. Crustal thickening and lateral flow during compression of hot lithospheres, with particular reference to Precambrian times. *Terra Nova*, **18**, 72-78.

Carrington, D.P. & Watt, G.R., 1995. A geochemical and experimental study of the role of K-feldspar during water-undersaturated melting of metapelites. *Chemical Geology*, **122**, 59-76.

Cawood, P. A., Kröner, A., Collins, W. J., Kusky, T. M., Mooney, W. D. & Windley, B. F., 2009. Accretionary orogens through Earth history. *Geological Society, London, Special Publications*, **318**, 1-36.

Chardon, D., Jayananda, M. & Peucat, J. J., 2011. Lateral constrictional flow of hot orogenic crust: Insights from the Neoarchean of south India, geological and geophysical implications for orogenic plateaux. *Geochemistry,* Geophysics, *Geosystems*, **12**.

Chardon, D., Gapais, D. & Cagnard, F., 2009. Flow of ultra-hot orogens: a view from the Precambrian, clues for the Phanerozoic. *Tectonophysics,* **477**, 105-118.

Condie, K. C., 1998. Episodic continental growth and supercontinents: a mantle avalanche connection? *Earth and Planetary Science Letters*, **163**, 1, 97-108.

Connolly, J. A. D., 2005. Computation of phase equilibria by linear programming : A tool for geodynamic modeling and its application to subduction zone decarbonation. *Earth and Planetary Science Letters*, **236**, 524-541.

Connolly, J.A.D. & Petrini, K., 2002. An automated strategy for calculation of phase diagram sections and retrieval of rock properties as a function of physical conditions. *Journal of Metamorphic Geology,* **20**, 697-708.

Dampare, S.B., Shibata, T., Asiedu, D.K., Osae, S. & Banoeng-Yakubo, B., 2008. Geochemistry of Paleoproterozoic metavolcanic rocks from the southern Ashanti volcanic belt Ghana: Petrogenetic and tectonic setting implications. *Precambrian Research,* **162**, 403–423.

Davis, D.W., Hirdes, W., Schaltegger, U. & Nunoo, E.A., 1994. U–Pb age constraints on deposition and provenance of Birimian and gold-bearing Tarkwaian sediments in Ghana West Africa. *Precambrian Research*, **67**, 89–107.

De Andrade, V., Vidal, O., Lewin, E., O'Brien, P. & Agard, P., 2006. Quantification of electron microprobe compositional maps of rock thin sections: an optimized method and examples. *Journal of Metamorphic Geology*, **24**, 655–668.

De Capitani, C. & Brown, T.H., 1987. The computation of chemical equilibria in complex systems containing non-ideal solutions. *Geochimica et Cosmochimica Acta,* **51**, 2639-2652.

De Kock, G.S. Theveniaut, H., Botha, P.W. & Gyapong, W., 2012. Timing the structural events in the Palaeoproterozoic Bolé–Nangodi belt terrane and adjacent Maluwe basin, West African craton, in central-west Ghana. *Journal of African Earth Sciences,* **65**, 1–24.

De Kock, G.S., Armstrong, R.A., Siegfried, H.P. & Thomas, E., 2011. Geochronology of the Birim Supergroup of the West African craton in the Wa-Bolé region of central-west Ghana: implications for the stratigraphic framework. *Journal of African Earth Sciences,* **59**, 1–40.

Debat, P., Nikiema, S., Mercier, A., Lompo, M., Beziat, D., Bourges, F., Roddaz, M., Salvi, S., Tollon, F. & Wenmenga, U. A., 2003. New metamorphic constraint for the Eburnean orogeny from Paleoproterozoic formations of the Man shield (Aribinda and Tampelga countries, Burkina Faso) : *Precambrian Research*, **123**, 47-65.

Duchêne, S., Lardeaux, J. M. & Albarède, F., 1997. Exhumation of eclogites: insights from depth-time path analysis. *Tectonophysics*, **280**, 125-140.

Easton, R. M., 2000. Metamorphism of the Canadian Shield, Ontario, Canada. I. The Superior Province. *The Canadian Mineralogist*, **38**, 287-317.

Egal, E., Thieblemont, D., Lahondere, D., Guerrot, C., Costea, C.A., Iliescu, D., Delor, C., Goujou, J.-C., Lafon, J.M. & Tegyey, M., 2002. Late Eburnean granitization and tectonics along the western and northwestern margin of the Archean Kenema- Man domain (Guinea West African Craton). *Precambrian Researc*h, **117**, 57–84.

Eisenlohr, B.N. & Hirdes, W., 1992. The structural development of the early Proterozoic Birimian and Tarkwaian rocks of southwest Ghana, West Africa. *Journal of African Earth Sciences*, **14**, 313–325.

England, P. C. & Thompson, A. B., 1984. Pressure—temperature—time paths of regional metamorphism I. Heat transfer during the evolution of regions of thickened continental crust. *Journal of Petrology*, **25**, 894-928.

England, P. & Molnar, P., 1990. Surface uplift, uplift of rocks, and exhumation of rocks. *Geology*, **18**, 1173-1177.

Feybesse, J.-L., Billa, M., Guerrit, C., Duguey, E., Lescuyer, J.-L., Milesi, J.P. & Bouchot, V., 2006. The paleoproterozoic Ghanaian province : Geodynamic model and ore controls, including regional stress modeling. *Precambrian Research*, **149**, 149-196.

Feybesse, J.L., 1990. The Bororno-Goren lower proterozoic “belt” (Burkina-Faso): an example of interference between two Eburnean transcurrent phases. *Comptes Rendus – Academie des Sciences*. Geoscience 310 (serie II), 1353–1360.

Galipp, K., Klemd, R. & Hirdes, W., 2003. Metamorphism and geochemistry of the Paleoproterozoic Birimian Sefwi volcanic belt (Ghana, West Africa). *Geologisches Jahrbuch*, **111**, 151–191.

Ganne, J., De Andrade, V., Weinberg, R., Dubacq, B., Vidal, O. and Kagambega, N., Naba, S., Baratoux, L., Jessell, M. & Allibon, J., 2012. Modern-style plate subduction preserved in the Palaeoproterozoic West African Craton : *Nature Geoscience*, **5**, 60-65.

Gapais, D., Cagnard, F., Gueydan, F., Barbey, P. & Ballevre, M., 2009. Mountain building and exhumation processes through time: inferences from nature and models. *Terra Nova*, **21**, 188-194.

Gapais, D., Pelletier, A., Ménot, R. P. & Peucat, J. J., 2008. Paleoproterozoic tectonics in the Terre Adélie Craton (East Antarctica). *Precambrian Research*, **162**, 531-539.

Gasquet, D., Barbey, P., Adou, M. & Paquette, J.L., 2003. Structure Sr-Nd isotope geochemistry and zircon U–Pb geochronology of the granitoids of the Dabakala area (Cote d'Ivoire): evidence for a 2.3 Ga crustal growth event in the Palaeoproterozoic of West Africa? *Precambrian Research*, **127**, 329–354.

Goscombe, B., Blewett, R., Czarnota, K., Maas, R. & Groenewald, B, 2009. Metamorphic evolution and integrated terrane analysis of the eastern Yilgarn Craton: rationale, methods, outcomes and interpretation. Geoscience Australia, Record 2009/23. 270pp.

Hein, K.A.A., 2010. Succession of structural events in the Goren greenstone belt (Burkina Faso): implications for West African tectonics. *Journal of African Earth Sciences*, **56**, 83–94.

Hirdes, W., Davis, D.W., Ludtke, G. & Konan, G., 1996. Two generations of Birimian (Paleoproterozoic) volcanic belts in northeastern Cote d'Ivoire (West Africa): consequences for the 'Birimian controversy. *Precambrian Research*, **80**, 173–191.

Hyndman, R. D., Currie, C. A. & Mazzotti, S. P., 2005. Subduction zone backarcs, mobile belts, and orogenic heat. *GSA Today*, **15**, 4-10.

Jessell, M. W., Amponsah, P. O., Baratoux, L., Asiedu, D. K., Loh, G. K. & Ganne, J. (2012). Crustal-scale transcurrent shearing in the Paleoproterozoic Sefwi-Sunyani-Comoé region, West Africa. *Precambrian Research*, **212**, 155-168.

John, T., Klemd, R., Hirdes, W. & Loh, G., 1999. The metamorphic evolution of the Pale-oproterozoic (Birimian) volcanic Ashanti belt (Ghana, West Africa). *Precambrian Research*, **98**, 11–30.

Johnson, T. E., White, R. W. & Powell, R., 2008. Partial melting of metagreywacke: a calculated mineral equilibria study. *Journal of Metamorphic Geology*, **26**, 8, 837-853.

Karlstrom, K. E., Åhäll, K. I., Harlan, S. S., Williams, M. L., McLelland, J. & Geissman, J. W., 2001. Long-lived (1.8–1.0 Ga) convergent orogen in southern Laurentia, its extensions to Australia and Baltica, and implications for refining Rodinia. *Precambrian Research*, **111**, 5-30.

Klemd, R., Hunken, U. & Olesch, M., 2002. Metamorphism of the country rocks hosting gold-sulfide-bearing quartz veins in the Paleoproterozoic southern Kibi- Winneba belt (SE-Ghana). *Journal of African Earth Sciences*, **35**, 199–211.

Komiya, T., Hayashi, M., Maruyama, S. & Yurimoto, H., 2002. Intermediate-P/T type Archean metamorphism of the Isua supracrustal belt: implications for secular change of geothermal gradients at subduction zones and for Archean plate tectonics. *American Journal of Science*, **302**, 806-826.

Kouamelan, A.N., Delor, C. & Peucat, J.-J., 1997. Geochronological evidence for reworking of Archaean terranes during the Early Proterozoic (2.1 Ga) in the western Côte d'Ivoire (Man Rise - West African Craton). *Precambrian Research*, **86**, 177–199.

Kouamelan, A. N., 1996. Géochronologie et Géochimie des Formations Archéennes et Protérozoïques de la Dorsale de Man en Côte d'Ivoire. Implications pour la Transition Archéen-Protéozoïque (Doctoral dissertation, Université Rennes 1).

Kretz, R., 1983. Symbols of rock-forming minerals. *American Mineralogist*, **68**, 277–279.

Kriebek, B., Sykorová, I., Machovic, V. & Laufek, F., 2008. Graphitization of organic matter and fluid-deposited graphite in Palaeoproterozoic (Birimian) black shales of the Kaya-Goren greenstone belt (Burkina Faso West Africa). *Journal of Metamorphic Geology*, **26**, 937–958.

Laurent, O., Martin, H., Doucelance, R., Moyen, J. F. & Paquette, J. L., 2011. Geochemistry and petrogenesis of high-K "sanukitoids" from the Bulai pluton, Central Limpopo Belt, South Africa: Implications for geodynamic changes at the Archaean–Proterozoic boundary. *Lithos*, **123**, 73-91.

Laurent, O., Martin, H., Moyen, J. F. & Doucelance, R., 2014. The diversity and evolution of late-Archean granitoids: Evidence for the onset of "modern-style" plate tectonics between 3.0 and 2.5 Ga. *Lithos*, **205**, 208-235.

Le Breton, N., & Thompson, A.B., 1988. Fluid-absent (dehydration) melting of biotite in metapelites in the early stages of crustal anatexis. *Contributions to Mineralogy and Petrology*, **99**, 226-237.

Ledru, P., Pons, J., Milesi, J.P., Feybesse, J.L. & Johan, V., 1991. Transcurrent tectonics and polycyclic evolution in the lower Proterozoic of Senegal-Mali. *Precambrian Research*, **50**, 337–354.

Lemoine, S., Tempier, P., Bassot, J.P., Caen-Vachette, M. & Vialette, Y., 1990. The Burkinian orogenic cycle, precursor of the Eburnian orogeny in West Africa. *Geological Journal*, **25**, 171-188.

Leube, A., Hirdes, W., Mauer, R. & Kesse, G.O., 1990. The early Proterozoic Birimian Supergroup of Ghana and some aspects of its associated gold mineralization. *Precambrian Research*, **46**, 139–165.

Liégeois, J.P., Claessens, W., Camara, D. & Klerkx, J., 1991. Short-lived Eburnian orogeny in southern Mali. Geology, tectonics, U–Pb and Rb–Sr geochronology. *Precambrian Research* **50**, 111–136.

Lompo, M., 2009. A model of subsidence of an oceanic plateau magmatic rocks in the Man-Leo Shield of the West African Craton Geodynamic evolution of the 2.25–2.0 Ga Palaeoproterozoic. In: Reddy, S.M., Mazumder, R., Evans, D.A.D. & Collins, A.S. (Eds.), *Palaeoproterozoic Supercontinents and Global Evolution*. Geological Society, London, pp. 231–254.

Martin, H., Smithies, R. H., Rapp, R., Moyen, J. F. & Champion, D., 2005. An overview of adakite, tonalite–trondhjemite–granodiorite (TTG), and sanukitoid: relationships and some implications for crustal evolution. *Lithos*, **79**, 1-24.

Melcher, F., 1995. Genesis of chemical sediments in Birimian greenstone belts: evidence from gondites and related manganese-bearing rocks from northern Ghana. *Mineralogical Magazine*, **59**, 229-251.

Melcher, F. & Stumpfl, E.F., 1994. Palaeoproterozoic Exhalite Formation in Northern Ghana; Source of Epigenetic Gold-Quartz Vein Mineralization? *Geologisches Jahrbuch*, **100**, 201-246.

Metelka, V., Baratoux, L., Naba, S. & Jessell, W.M., 2011. A geophysically constrained litho-structural analysis of the Eburnean greenstone belts and associated granitoid domains, western Burkina Faso. *Precambrian Research*, **190**, 48–69.

Milesi, J.P., Feybesse, J.L., Pinna, P., Deschamps, Y., Kampunzu, H., Muhongo, S., Lescuyer, J.L., Le Goff, E., Delor, C., Billa, M., Ralay, F. & Heinry, C., 2004. Geological map of Africa 1:10,000,000, SIGAfrique project. In: 20th Conference of African Geology, BRGM, Orleans, France, 2–7 June, http://www.sigafrique.net.

Milesi, J.-P., Ledru, P. & Feybesse, J.-L., Dommanget, A., Marcoux, E., 1992. Early Proterozoic ore deposits and tectonics of the Birimian orogenic belt West Africa. *Precambrian Research*, **58**, 305–344.

Milési, J.P., Feybesse, J.L., Ledru, P., Dommanget, A., Ouedraogo, M.F., Marcoux, E., Prost, A., Vinchon, C., Sylvain, J.P., Johan, V., Tegyey, M., Calvez, J.Y. & Lagny, Ph., 1989. Minéralisations aurifères de l'Afrique de l'ouest, leurs relations avec l'évolution litho-structurale au Protérozoïque inférieur. Carte géologique au 1/2.000.000. *Chronique de la recherche minière*, **497**, 3–98.

Millonig, L., Zeh, A., Gerdes, A., Klemd, R. & Barton, J.M., 2010. Decompressional Heating of the Mahalapye Complex (Limpopo Belt, Botswana): a Response to Palaeoproterozoic Magmatic Underplating ? *Journal of Petrology*, **51**, 3, 703-729.

Möller, A., Appel, P., Mezger, K. & Schenk, V., 1995. Evidence for a 2 Ga subduction zone: eclogites in the Usagarian belt of Tanzania, *Geology,* **23**, 1067-1070.

Moresi, L., Betts, P. G., Miller, M. S. & Cayley, R. A., 2014. Dynamics of continental accretion. *Nature*, **508**, 245-248.

Moyen, J. F., 2011. The composite Archaean grey gneisses: petrological significance, and evidence for a non-unique tectonic setting for Archaean crustal growth. *Lithos*, **123**, 21-36.

Naba, S., Lompo, M., Debat, P., Bouchez, J.L. & Beziat, D., 2004. Structure and emplacement model for late-orogenic Paleoproterozoic granitoids: the Tenkodogo-Yamba elongated pluton (Eastern Burkina Faso). *Journal of African Earth Sciences*, **38**, 41–57.

Newton, R.C., Charlu, T.V. & Kleppa, O.J., 1980. Thermochemistry of the high structural state plagioclases. *Geochemica Cosmochimica Acta*, **44**, 933-941.

Oberthür, T., Vetter, U., Davis, D.W. & Amanor, J.A., 1998. Age constraints on gold mineralization and Paleoproterozoic crustal evolution in the Ashanti belt of southern Ghana. *Precambrian Research*, **89**, 129–143.

Opare-Addo, E., Browning, P. & John, B.E., 1993. Pressure-temperature constraints on the evolution of an Early Proterozoic plutonic suite in southern Ghana, West Africa. *Journal of African Earth Sciences*, **17**, 51, 13–22.

Parra, T., Vidal, O. & Agard, P., 2002. A Thermodynamic model for Fe-Mg dioctahedral K-white micas using data from phase equilibrium experiments and natural pelitic assemblages. *Contributions to Mineralogy and Petrology*, **143**, 706-732.

Patiño Douce, A.E. & Harris, N., 1998. Experimental constraints on Himalayan anatexis. *Journal of Petrology*, **39**, 689-710.

Patisson, D.R.M., De Capitan, C. & Gaidies, F., 2011. Petrological consequences of variations in metamorphic reaction affinity. *Journal of Metamorphic Geology*, **29**, 953-977.

Percival, J. A. & Skulski, T., 2000. Tectonothermal evolution of the northern Minto Block, Superior Province, Quebec, Canada. *The Canadian Mineralogist*, **38**, 345-378.

Percival, J. A., Mortensen, J. K., Stern, R. A., Card, K. D. & Bégin, N. J., 1992. Giant granulite terranes of northeastern Superior Province: the Ashuanipi complex and Minto block. *Canadian Journal of Earth Sciences*, **29**, 2287-2308.

Perrouty, S., Aillères, L., Jessell, M. W., Baratoux, L., Bourassa, Y. & Crawford, B., 2012. Revised Eburnean geodynamic evolution of the gold-rich southern Ashanti Belt, Ghana, with new field and geophysical evidence of pre-Tarkwaian deformations. *Precambrian Research*, **204– 205**, 12– 39.

Peucat, J. J., Capdevila, R., Drareni, A., Mahdjoub, Y. & Kahoui, M., 2005. The Eglab massif in the West African Craton (Algeria), an original segment of the Eburnean orogenic belt: petrology, geochemistry and geochronology. *Precambrian Research*, **136**, 309-352.

Pitra, P., Kouamelan, A.N., Ballèvre, M. & Peucat, J-J., 2010. Palaeoproterozoic high-pressure granulite overprint of Archean continental crust : evidence for homogeneous crustal thickening (Man Rise, Ivory Coast). *Journal of Metamorphic Geology*, **28**, 41-58.

Platt, J. P., 1993. Exhumation of high-pressure rocks: A review of concepts and processes. *Terra nova*, **5**, 119-133.

Pons, J., Barbey, P., Dupuis, D. & Leger, J.M., 1995. Mechanisms of pluton emplacement and structural evolution of a 2.1 Ga juvenile continental crust: the Birimian of southwestern Niger. *Precambrian Research*, **70**, 281–301.

Pouclet, A., Vidal, M., Delor, C., Simeon, Y. & Alric, G., 1996. Le volcanisme birimien du nord-est de la Cote-d'Ivoire mise en evidence de deux phases volcanotectoniques distinctes dans l'evolution geodynamique du Paleoproterozoique. *Bulletin de la Societe Geologique de France*, **167**, 529–541.

Powell, R., Holland, T. & Worley, B., 1998. Calculating phase diagrams involving solid solutions via non-linear equations, with examples using THERMOCALC. *Journal of Metamorphic Geology*, **16**, 577-588.

Rey, P. F., Teyssier, C. & Whitney, D. L., 2009. Extension rates, crustal melting, and core complex dynamics. *Geology*, **37**, 391-394.

Rey, P. F., Vanderhaeghe, O. & Teyssier, C. 2001. Gravitational collapse of the continental crust: definitions, regimes and modes. *Tectonophysics*, **342**, 435-449

Roques, M., 1948. Le Précambrien de l'Afrique occidentale française. *Bulletin de la Societe Geologique de France*, **15**, 8-9, 528-546.

Sandiford, M., 1989. Horizontal structures in granulite terranes: A record of mountain building or mountain collapse? *Geology*, **17**, 449-452.

Sawyer, E.W., 1994. Melt segregation in the continental crust. *Geology*, **22**, 1019–1022.

Soumaila, A. & Garba, Z., 2006. Le métamorphisme des formations de la ceinture de roches vertes birimienne (paléoprotérozoïque) de Diagorou-Darbani (Liptako, Niger, Afrique de l'Ouest). *Africa Geoscience Review*, **13**, 1, 116-128.

Stevens, G. & Moyen, J. F., 2007. Metamorphism in the Barberton Granite Greenstone Terrane: A Record of Paleoarchean Accretion. *Developments in Precambrian Geology*, **15**, 669-698.

Stöckhert, B., & Gerya, T. V., 2005. Pre-collisional high pressure metamorphism and nappe tectonics at active continental margins: a numerical simulation. *Terra Nova*, **17**, 102-110.

Taylor, P.N., Moorbath, S., Leube, A. & Hirdes, W., 1992. Early Proterozoic crustal evolution in the birimian of Ghana: constraints from geochronology and isotope geochemistry. *Precambrian Research* **56**, 97–111.

Tshibubudze, A., Hein, K.A.A. & Marquis, P., 2009. The Markoye shear zone in NE Burkina Faso. *Journal of African Earth Sciences*, **55**, 245–256.

Tempier, P., 1986. Le Burkinien; cycle orogenique majeur du Proterozoique inferieur en Afrique de l'Ouest, Journée scientifique du C.I.F.E.G. CIFEG, Paris, France, pp. 17–23.

Triboulet, C. & Feybesse, J.L., 1998. Les métabasites birimiennes et archéennes de la région de Toulepleu-lty (Côte d'Ivoire): des roches portées à 8 kbar (~24 km) et 14 kbar (~42 km) au Paléoprotérozoïque. *Comptes Rendus de l'Académie des Sciences*, Sciences de la terre et des planètes, **327**, 61–66.

Väisänen, M., Mänttäri, I. & Hölttä, P., 2002. Svecofennian magmatic and metamorphic evolution in southwestern Finland as revealed by U-Pb zircon SIMS geochronology. *Precambrian research*, **116**, 111-127.

Vanderhaeghe, O., 2009. Migmatites, granites and orogeny: Flow modes of partially-molten rocks and magmas associated with melt/solid segregation in orogenic belts. *Tectonophysics*, **477**, 119-134.

Vanderhaeghe, O. & Teyssier, C., 2001. Partial melting and flow of orogens. *Tectonophysics*, **342**, 451-472.

Vanderhaeghe, O., Ledru, P., Thiéblemont, D., Egal, E., Cocherie, A., Tegyey, M. & Milési, J. P., 1998. Contrasting mechanism of crustal growth: Geodynamic evolution of the Paleoproterozoic granite–greenstone belts of French Guiana. *Precambrian Research*, **92**, 165-193.

Vidal, M., Gumiaux, C., Cagnard, F., Pouclet, A., Ouattara, G. & Pichon, M., 2009. Evolution of a Paleaoproterozoic « weak type » orogeny in the West African Craton (Ivory Coast). *Tectonophysics*, **477**, 145–159.

Vidal, M. & Alric, G., 1994. The Palaeoproterozoic (Birimian) of Haute-Comoe in the West African craton Ivory Coast: a transtensional back-arc basin. *Precambrian Research*, **65**, 207–229.

Vidal, O., DeAndrade, V., Lewin, E., Munoz, M., Parra, T. & Pascarelli, S., 2006. P–T-deformation-Fe^{3+}/Fe^{2+} mapping at the thin section scale and comparison with XANES mapping. Application to a garnet-bearing metapelite from the Sambagawa metamorphic belt (Japan). *Journal of Metamorphic Geology*, **24**, 669–683.

Vidal, O., Parra, T. & Trotet, F., 2001. A thermodynamic model for Fe-Mg aluminous chlorite using data from phase equilibrium experiments and natural pelitic assemblages in the 100-600 °C, 1-25 kbar P-T range. *American Journal of Science*, **301**, 557-592.

Whitney, D. L., Teyssier, C. & Vanderhaeghe, O., 2004. Gneiss domes and crustal flow. *Gneiss domes in orogeny*, **380**, 15.

Yamato, P., Agard, P., Goffe, B., De Andrade, V., Vidal, O. & Jolivet, L., 2007a. New, high-precision P–T estimates for Oman blueschists: implications for obduction, nappe stacking and exhumation processes. *Journal of Metamorphic Geology*, **25**, 657–682.

Yamato, P., Agard, P., Burov, E., Le Pourhiet, L., Jolivet, L. & Tiberi, C., 2007b. Burial and exhumation in a subduction wedge: Mutual constraints from thermomechanical modeling and

natural P-T-t data (Schistes Lustrés, western Alps). *Journal of Geophysical Research: Solid Earth (1978–2012)*, **112**(B7).

Zeh, A., Jaguin, J., Poujol, M., Boulvais, P., Block, S. & Paquette, J.-L., 2013. Juvenile crust formation in the northeastern Kaapvaal Craton at 2.97 Ga–Implications for Archean terrane accretion, and the source of the Pietersburg gold. *Precambrian Research*, **233**, 20–43.

Zeh, A., 2001. Inference of a detailed P–T path from P–T pseudosections using metapelitic rocks of variable composition from a single outcrop, Shackleton Range, Antarctica. *Journal of Metamorphic Geology*, **19**, 4, 329-350.

Zhao, G., Cawood, P.A., Wilde, S.A. & Sun, M., 2002. Review of global 2.1—1.8 Ga orogens. Implications for a pre-Rodinia supercontinent. *Earth-Science Reviews*, **59**, 125-162.

Zitsmann, A., Kiessling, R., Ostwald, J. & Treder, H-W., 1997. Geological, Geophysical and Geochemical Investigations in the Bui Belt Area in Ghana. *Geologisches Jahrbuch*, Reihe B, Heft 88. 269p.

Petrological and geochronological constraints on lower crust exhumation during Paleoproterozoic (Eburnean) orogeny, NW Ghana, West African craton.

Sylvain Block[1], Jerome Ganne[1], Lenka Baratoux[1], Armin Zeh[2], Luis A. Parra-Avila[3], Mark Jessell[3], Laurent Ailleres[4], Luc Siebenaller[1]

[1] Geosciences Environnement Toulouse, Observatoire Midi Pyrénées, 14 ave E. Belin, 31400, Toulouse, France.

[2] Institut für Geowissenschaften, Altenhöfer Allee 1, D-60438 Frankfurt am Main, Germany.

[3] Center for Exploration Targeting, The University of Western Australia, 35 Stirling Highway, Crawley, Perth, Western Australia 6009

[4] Monash University, School of Geosciences, Wellington Road, Clayton, Vic 3800, Australia

SUPPORTING INFORMATION

APPENDIX S1: COMPLEMENTARY SAMPLES.

Petrography and mineral chemistry

Sample BN365 (migmatitic amphibolite gneiss)

Sample BN365 is from a kilometric amphibolite sliver at the base of a sequence of migmatitic ortho- and paragneisses, in the Bole-Bulenga domain. It is separated from low-grade schists of the Maluwe domain by the Bole-Nangodi shear zone (Fig. 2). Petrographic relationships define a succession of three metamorphic assemblages (A) to (C). The amphibolites contain small volumes of unconnected leucosomes, suggesting limited melting rate and melt loss. The rock is made of a melanocratic Hbl – Pl – Cpx – Ilm – Bt – Qz matrix, and of garnet porphyroblasts (Fig. S1a,b). Garnet is unzoned and has compositions of Alm50-54, Grs28-31, Prp15-18 and Sps2-4 (Fig S1h). It contains inclusions of hornblende1, plagioclase1 and rutile. The latter is partly replaced by ilmenite or titanite (Fig. S1c). Hornblende1 is corroded and has a #Mg = 0.53-0.55, Ca/Na = 3.84-4.93, with $(Na+Ca)_B$ =1.84-1.89 a.p.f.u. and $(Na+K)_A$ = 0.42-0.53 a.p.f.u. It is in contact with plagioclase1 (An35-46). In contrast, matrix hornblende2 has a #Mg = 0.57-0.60, Ca/Na = 4.57-5.81, $(Na+Ca)_B$ =1.88-1.94 a.p.f.u. and $(Na+K)_A$ = 0.36-0.39 a.p.f.u.; and is in contact with An39-45 plagioclase2. Clinopyroxene has a diopside composition with #Mg = 0.70-0.74. Biotite is a minor retrograde phase representing less than 1vol% of the rock, with a #Mg = 0.38-0.40 and Ti^{vi} = 0.07-0.09 a.p.f.u. Melting is evidenced by quartz-plagioclase-rich leucocratic domains and by “string of beads” textures between matrix grains (Fig. S1b).

Mineral inclusions in garnet belong to assemblage (A): Grt + Hbl1 + Pl1 + Cpx + Rt + Qz + L ± Bt. Matrix minerals in contact with garnet define the peak metamorphic assemblage (B): Grt + Hbl2 + Pl2 + Cpx + Ilm + Qz + L ± Bt. Both (A) and (B) correspond to transitional assemblages between the amphibolite and high-P granulite facies. Garnet porphyroblasts are partially replaced by leucocratic domains that are dominated by plagioclase3 and contain minor hornblende3 (Fig. S1a). Grains are euhedral, display 120° grain boundaries, and have compositions similar to matrix grains. These textural relationships suggest garnet resorption at supra-solidus conditions during reaction:

Grt + Cpx + L => Pl3 + Hbl3 (R1).

Replacement of ilmenite by titanite illustrates retrogression and the local development of the amphibolite-facies assemblage (C): Grt + Hbl3 + Pl3 + Ttn + Qz ± Bt.

Sample BN534 (Garnet – kyanite-bearing migmatitic paragneiss)

Sample BN534 is a metatexite derived from a paragneiss collected in the north-western Bole-Bulenga domain, to the west of the Jirapa SZ (Fig. 2). At outcrop scale, it develops foliation-parallel leucosomes connected to crosscutting granitic veins, and displays neosomes comprising aggregates of peritectic kyanite and garnet. Petrographic relationships are used to identify three successive metamorphic assemblages (A) to (C). Garnet forms centimetric aggregates in quartz-plagioclase leucocratic domains (Fig. S1d,e). It is unzoned and has compositions of Alm75-76, Prp17-20, Grs4-6, Sps1-3, except for margins which were re-equilibrated and are Alm77, Prp15-16, Grs6, Sps2 (Fig. S1h). Plagioclase in neosomes and in the matrix has similar compositions of An27-30. Neosomes additionally comprise sheared poikiloblastic kyanite with biotite1, rutile and rare muscovite1 inclusions (Fig. S1d,e). These phases belong to a first assemblage (A): Grt + Ky + Bt1 + Ms1 + Rt + Pl + Qz + L, consistent with metamorphic conditions at the transition between the amphibolite and high-P granulite facies. Rutile and sheared muscovite are only present in garnet and (partly retrogressed) kyanite. This indicates that they were preserved because they were locked in porphyroblasts. Their absent from the matrix suggests that they reacted out to form the amphibolite-granulite transitional assemblage (B): Grt + Ky + Bt1 + Pl + Qz + L. Biotite2 occurs in the matrix or forms selvedge microstructures around neousomes (Fig. S1d). It has a #Mg = 0.54-0.59, Ti^{vi} = 0.09-0.13 a.p.f.u., that are similar to biotite1. Quartz grains crystallised in neosomes contains minor amounts of fibrolite inclusions in their centres, suggesting that the rock crossed back below the solidus under conditions of sillimanite stability (Fig. S1e). Large (up to 0.5cm) flakes of muscovite2 overgrow neosomes and replace kyanite, and rutile inclusions are replaced by ilmenite (Fig. S1d,e). They have compositions of Ms77-82, Pg18-23, with Si = 3.05-3.14 and Al^{vi} = 1.84-1.90. Staurolite porphyroblasts develop in the matrix (Fig. S1e) and have Mg# = 14-22. They belong to the amphibolite-facies assemblage (C): Grt + Bt2 + St + Ms2 + Pl + Ilm + Qz.

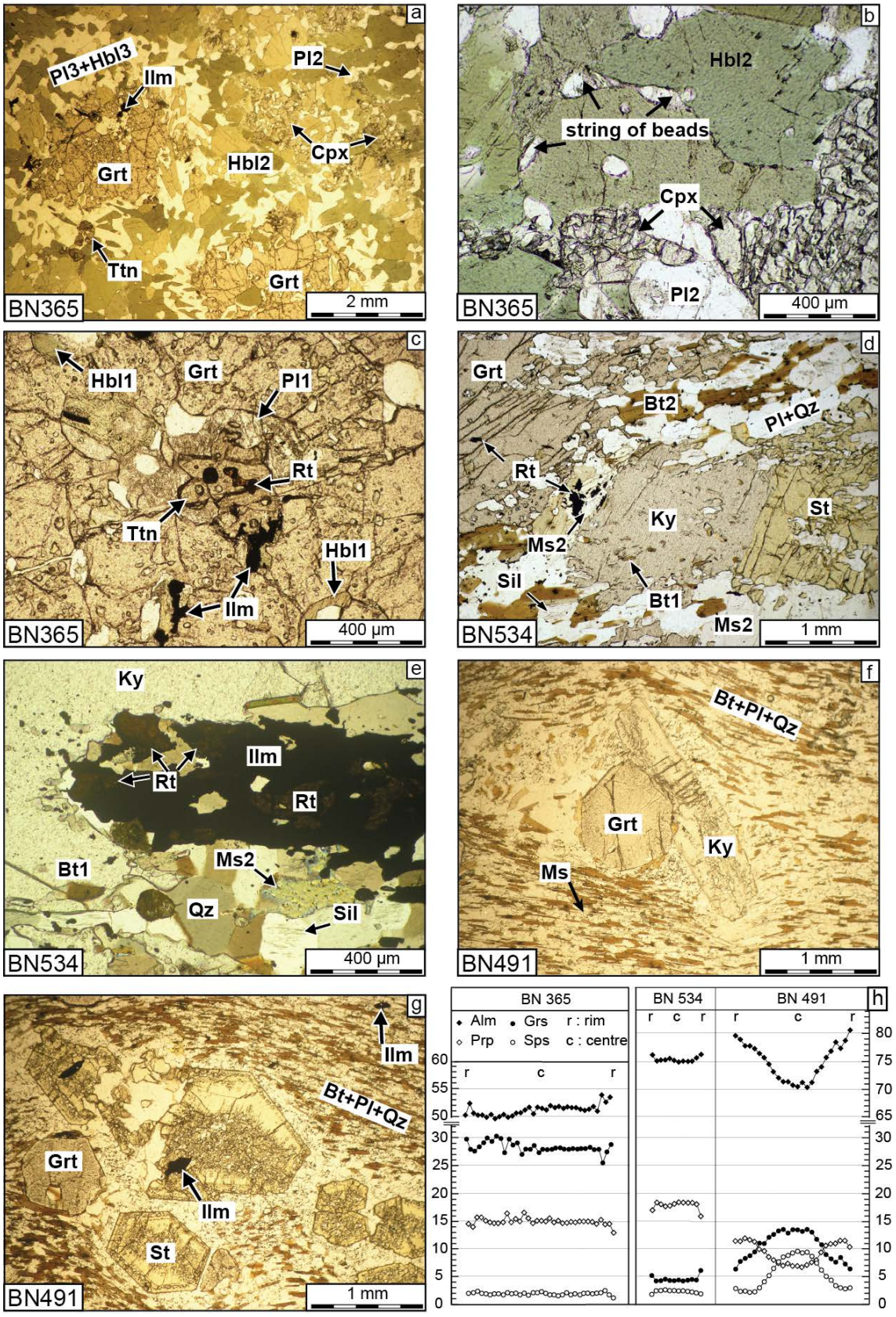

Fig. S1. *Photomicrographs of samples BN365 (a-c), BN534 (d-e) and BN491(f-g). (a) Grt porphyroblasts are partially resorbed and rimmed by euhedral Hbl3 and Pl3 grains. The rock matrix is dominated by Hbl2 and additionally contains Pl2 + Cpx + Ilm + Qz. (b) Hbl2 and Cpx in contact in the matrix. Grain boundaries occasionally contain Qz-Pl 'beads' which may represent melt relics. (c) Hbl1, Pl1 and Rt relics included in Grt. Rt is replaced by intergrown Ilm-Ttn. (d) Elongated Rt and*

Ms1 grains in Grt-Ky aggregates with Qz-Pl neosomes bounded by oriented Bt2 selvedges. (e) Poikiloblastic St and Ms2 overgrow the fabric defined by oriented Bt2. Fibrolite aggregates ~100µm wide are included in Qz. (f) Ky porphyroblast overgrows Grt and is rotated relative to oriented matrix Bt-Pl-Ms-Qz. Retrograde Ms develops at the expense of Ky. (g) Euhedral St overgrows the fabric. Qz-Ilm grains form concentric inclusion trails illustrating porphyroblast growth. (h) Chemical composition profiles across Grt porphyroblasts of samples BN365, BN534 and BN491.

Sample	**BN 365**							**BN 534**						**BN 491**						
Mineral	Grt	Cpx	Hbl1	Hbl3	Pl3	Pl1	Bt	Grt	Grt	St	Ms	Bt	Pl	Grt	Grt	St	St	Pl	Ms	Bt
position		matrix	Incl	rim	rim	Incl	matrix	core	margin	matrix	retrog.	matrix	matrix	core	rim	core	rim	matrix	matrix	matrix
SiO_2	38.9	52.2	44.1	46.6	58.0	58.3	34.4	37.5	37.5	27.3	46.2	37.1	60.9	37.2	37.6	28.6	28.7	61.7	46.4	36.8
TiO_2	0.05	0.12	1.10	0.82	b.d.l.	b.d.l.	1.94	0.05	b.d.l.	0.56	0.59	1.49	b.d.l.	b.d.l.	b.d.l.	0.70	0.63	0.04	0.81	2.51
Al_2O_3	21.4	2.6	11.9	10.5	26.7	27.1	16.7	21.9	21.9	53.3	36.3	19.3	24.8	21.1	21.3	53.3	54.1	24.1	36.3	19.6
Fetot as FeO	24.4	8.7	16.5	14.7	0.11	0.09	25	34.2	34.5	13.7	0.72	15.1	0.04	32.2	34.9	13.3	13.0	0.30	1.28	18.6
MnO	1.23	0.14	0.22	0.01	b.d.l.	b.d.l.	0.33	1.08	0.82	b.d.l.	b.d.l.	0.03	b.d.l.	3.89	1.01	0.07	b.d.l.	0.03	b.d.l.	0.15
MgO	4.13	12.7	10.3	11.5	b.d.l.	b.d.l.	9.29	4.65	4.05	1.72	0.45	12.42	b.d.l.	1.85	2.99	1.29	0.58	b.d.l.	0.39	9.40
CaO	10.5	23.1	11.6	12.0	9.13	6.91	0.07	1.49	2.14	b.d.l.	0.04	0.03	6.12	4.49	2.88	0.02	b.d.l.	5.61	b.d.l.	b.d.l.
Na_2O	b.d.l.	0.37	1.67	1.27	6.51	6.40	b.d.l.	b.d.l.	0.02	0.02	1.72	0.05	8.29	0.01	0.01	b.d.l.	b.d.l.	8.69	1.48	0.14
K_2O	b.d.l.	b.d.l.	0.30	0.24	0.05	1.06	7.11	0.01	b.d.l.		8.84	9.34	0.06	b.d.l.	b.d.l.			0.03	8.85	9.30
Cr_2O_3	0.02	0.11	0.06	0.17			0.10	b.d.l.	0.01	0.02	0.01	0.04		0.05	b.d.l.	b.d.l.	0.07		0.04	0.18
ZnO		b.d.l.	b.d.l.	b.d.l.			b.d.l.													
Total	100.6	100.0	97.7	97.8	100.5	99.9	94.9	100.8	100.9	97.0	94.9	94.8	100.2	100.8	100.7	97.6	97.3	100.5	95.5	96.8
Oxygen	12	6	23	23	32		22	12	12	46	22	22	32	12	12	46	46	32	22	22
Si	6.04	1.95	6.56	6.83	10.3	10.4	5.38	5.93	5.94	7.66	6.12	5.52	10.8	5.97	6.00	7.92	7.96	10.9	6.12	5.47
Al^{IV}	0.00	0.05	1.44	1.17	5.61	5.71	2.62	0.07	0.06	0.34	1.88	2.48	5.18	0.03	0.00	0.08	0.04	5.02	1.88	2.53
Al^{VI}	3.91	0.06	0.65	0.65			0.44	4.00	4.02	17.3	3.79	0.91		3.96	4.00	17.36	17.62		3.75	0.91
Fe^{3+}	0.00	0.01			0.02	0.00	0.00	0.09	0.07	0.59	0.02	0.00	0.01	0.09	0.00	0.50	0.23	0.04	0.03	0.00
Ti	0.01	0.00	0.12	0.09	0.00	0.00	0.23	0.01	0.00	0.12	0.06	0.17	0.00	0.00	0.00	0.15	0.13	0.01	0.08	0.28
Cr	0.00	0.00	0.01	0.02			0.01	0.00	0.00	0.00	0.00	0.01		0.01	0.00	0.00	0.01		0.00	0.02
Mg	0.96	0.70	2.28	2.52	0.00	0.00	2.16	1.10	0.96	0.72	0.09	2.76	0.00	0.44	0.71	0.53	0.24	0.00	0.08	2.08
Fe^{2+}	3.17	0.26	2.05	1.80	0.00	0.01	3.25	4.44	4.49	2.63	0.06	1.87	0.00	4.23	4.66	2.59	2.78	0.00	0.11	2.31
Mn^{2+}	0.16	0.00	0.03	0.00	0.00	0.00	0.04	0.15	0.11	0.00	0.00	0.00	0.00	0.53	0.14	0.02	0.00	0.00	0.00	0.02
Ca	1.75	0.92	1.85	1.88	1.75	1.33	0.01	0.25	0.36	0.00	0.01	0.01	1.16	0.77	0.49	0.00	0.00	1.06	0.00	0.00
Na	0.00	0.03	0.48	0.36	2.25	2.22	0.00	0.00	0.01	0.01	0.44	0.01	2.85	0.00	0.00	0.00	0.00	2.98	0.38	0.04
K	0.00	0.00	0.06	0.04	0.01	0.24	1.41	0.00	0.00		1.49	1.77	0.01	0.00	0.00			0.01	1.49	1.76
Zn		0.00								0.05	0.00	0.00				0.07	0.05		0.00	0.00
xPrp	0.16							0.18	0.16					0.07	0.12					
xAlm	0.53							0.75	0.76					0.71	0.78					
xSps	0.03							0.02	0.02					0.09	0.02					
xGrs	0.29							0.04	0.06					0.13	0.08					
xMg	0.23	0.73	0.53	0.58			0.40	0.20	0.18	0.21		0.60		0.09	0.13	0.17	0.08			0.47
xOr					0.00	0.06							0.00					0.00		
xAb					0.56	0.59							0.71					0.74		
xAn					0.44	0.35							0.29					0.26		

Table S1. *Representative compositions of minerals forming metamorphic assemblages used to constrain P-T conditions and P-T paths from pseudosections. b.d.l. = below detection limit.*

Sample BN491 (Garnet – kyanite – staurolite- bearing paragneiss)

Sample BN491 originates from the southern extremity of the Bole-Bulenga domain (Fig. 2). It is from a sub-solidus paragneiss separated by a NNE-striking high-strain zone from diatexites and metatexites represented by sample BN43. It comprises a matrix of oriented plagioclase, biotite, ilmenite, quartz + rare muscovite, and contains garnet, staurolite and kyanite porphyroblasts (Fig. S1f,g). Petrological relationships identify assemblages (A) to (C). Garnet is subhedral or partially replaced by biotite or staurolite. It displays a concentric zoning pattern typical of growth during prograde metamorphism. From core (garnet1) to rim (garnet2), it is Alm70-72 => 78-81, Prp6-8 => 11-12, Grs12-14 => 6-8, Sps9-10 => 2 (Fig. S1h). Retrograde re-equilibration of garnet2 margins is documented by the slight decrease of Prp to ~10 and an increase of Sps to 3. Garnet1 contains small (10-100µm) ilmenite and chlorite inclusions (#Mg = 42-45), which belong to a relict greenschist- to amphibolite-facies metamorphic assemblage (A): Grt1 + Chl + Ilm + Qz. Matrix biotite has a #Mg = 0.45-0.49, and Ti^{vi} = 0.12-0.19 a.p.f.u., plagioclase is An24-26, white mica has a muscovite composition with Pg~20, Si = 3.03-3.07 and Al^{vi} = 1.86-1.88. Syn-kinematic kyanite porphyroblasts overgrow garnet and are rotated in the metamorphic fabric (Fig. S1f). Kyanite belongs to assemblage (B): Grt2 + Ky + Bt + Pl + Ilm + Qz ± Ms, formed in the upper amphibolite-facies. Staurolite forms euhedral porphyroblasts that overgrow garnet and the metamorphic banding (Fig. S1g). It displays concentric growth patterns underlined by alternating inclusion-rich and inclusion-free domains. Staurolite #Mg is 16-18 => 8-10 from core to rim. Contact between staurolite rims, garnet2 and matrix minerals indicate the formation of amphibolite-facies assemblage (C): Grt2 + St + Bt + Pl + Ilm + Qz.

Results of *P–T* pseudosection construction.

Sample BN365 (migmatitic amphibolite gneiss)

The *P–T* pseudosection for sample BN365 is built by using the whole rock composition. It reveals that assemblage (A) Grt + Hbl1 + Pl1 + Cpx + Rt + Qz + Bt + L is stable at >10.0 kbar, 700-800°C (Fig. S2a), at the transition between the amphibolite and the high-pressure granulite facies. Calculated compositions indicate that garnet grew at 10.5-12.0 kbar, 720-750°C (Fig. S2b). These conditions overlap with the 10.0-11.0 kbar, 730-800°C conditions deduced from the compositions of clinopyroxene and plagioclase belonging to assemblage (B) (Fig. S2c). Increasing Ca/Na from hornblende1 to hornblend2 or 3 is consistent with decompression in the stability field of assemblage (B) and across reaction (R1) (Fig. S2b). The retrogression of rutile and ilmenite to titanite and the formation of assemblage (C) requires cooling in the amphibolite facies below 700°C at <9.0 kbar. Sample BN365 evolved along a clockwise *P–T* path. Melting above 10.5 kbar is followed by a limited decompression into the field of assemblage (B) at peak metamorphic temperatures of 730-800°C, at the transition between the high-pressure granulite- and amphibolite-facies. Susebquently the sample

records an amphibolite-f acies overprint. Peak metamorphic conditions correspond to a moderate apparent geothermal gradient of 15-20°C km^{-1}.

Sample BN534 (Garnet – kyanite-bearing migmatitic paragneiss)

The pseudosection used to constrain the prograde and peak *P–T* conditions is identical to that used for sample BN43 (Fig. 7), which is built with the composition of an average paragneiss. Isopleths of retrograde biotite are calculated from a pseudosection using the sample whole-rock composition (Table 2). The stability field of assemblage (A): Grt + Ky + Bt1 + Ms1 + Rt + Pl + Qz + L overlaps with the calculated conditions of garnet formation between 9.5-11.0kbar, 680-730°C. This indicates the rock crossed the solidus at > 9.5 kbar (Fig. S3a). The evolution from assemblage (A) to (B): Grt + Ky + Bt1 + Pl + Qz + L requires heating to about 750°C and/or decompression, in agreement with measured garnet and biotite compositions (Fig. S3b). Calculated plagioclase compositions in assemblage (B) (An 27-28) only partly match measured compositions (An 27-30), possibly due to local equilibria controlling plagioclase crystallisation from segregated melt in the leucosome. The crystallisation of retrograde sillimanite indicates that the rock crossed back below the solidus between 5.0 and 7.0 kbar. Assemblage (C): Grt + Bt2 + St + Ms2 + Pl + Ilm + Qz formed at 4.0-7.0 kbar, below 650°C. Sample BN534 records a clockwise *P–T* path. It crossed over the solidus above 9.5kbar and reached peak conditions of 9.5-11.0kbar, 680-730°C, that fit a moderate apparent geothermal gradient of 15-20°C km^{-1}, and that correspond to the transition between the amphibolite and high-P granulite facies. The rock then followed a decompression – cooling path back below the solidus and underwent a metamorphic overprint in the sub-solidus amphibolite facies.

Sample BN491 (Garnet – kyanite – staurolite- bearing paragneiss)

The *P–T* pseudosection (Fig. S3c,d) for sample BN491 uses the whole rock composition (Table 1). Intersecting isopleths corresponding to measured garnet1 and garnet2 compositions suggests a prograde evolution from 6.5-8.5 kbar, 520-550°C, to 7.0-9.0 kbar, 560-590°C (Fig. S3c). The crystallisation conditions of garnet1 correspond to the calculated stability field of assemblage Bt + Chl + Pg + Grt + Pl + Ilm + Qz. Compared to this, assemblage (A) Grt1 + Chl + Ilm + Qz lacks chlorite, paragonite and plagioclase, which were not preserved as inclusions in garnet1 or were destroyed during prograde metamorphism. Assemblage (B): Grt + Bt + Pl + Ky + Ms + Qz is predicted to form at 7.5-9.5 kbar, 610-650°C. Under these conditions, calculated plagioclase and biotite compositions show a good agreement with measured mineral compositions. The formation of assemblage (C): Grt + St + Bt + Pl + Ilm + Qz, with staurolite #Mg varying from 16-18 to 8-10 from core to rim, requires that the rock follows a decompression-cooling path from about 7.0 kbar, 610°C to 4.0 kbar, 550°C (Fig. S3c). The *P–T* conditions determined from the successive assemblages describe a clockwise *P–T*

path. Peak P and T are reached synchronously in the amphibolite facies and match a ~20°C km^{-1} apparent geotherm.

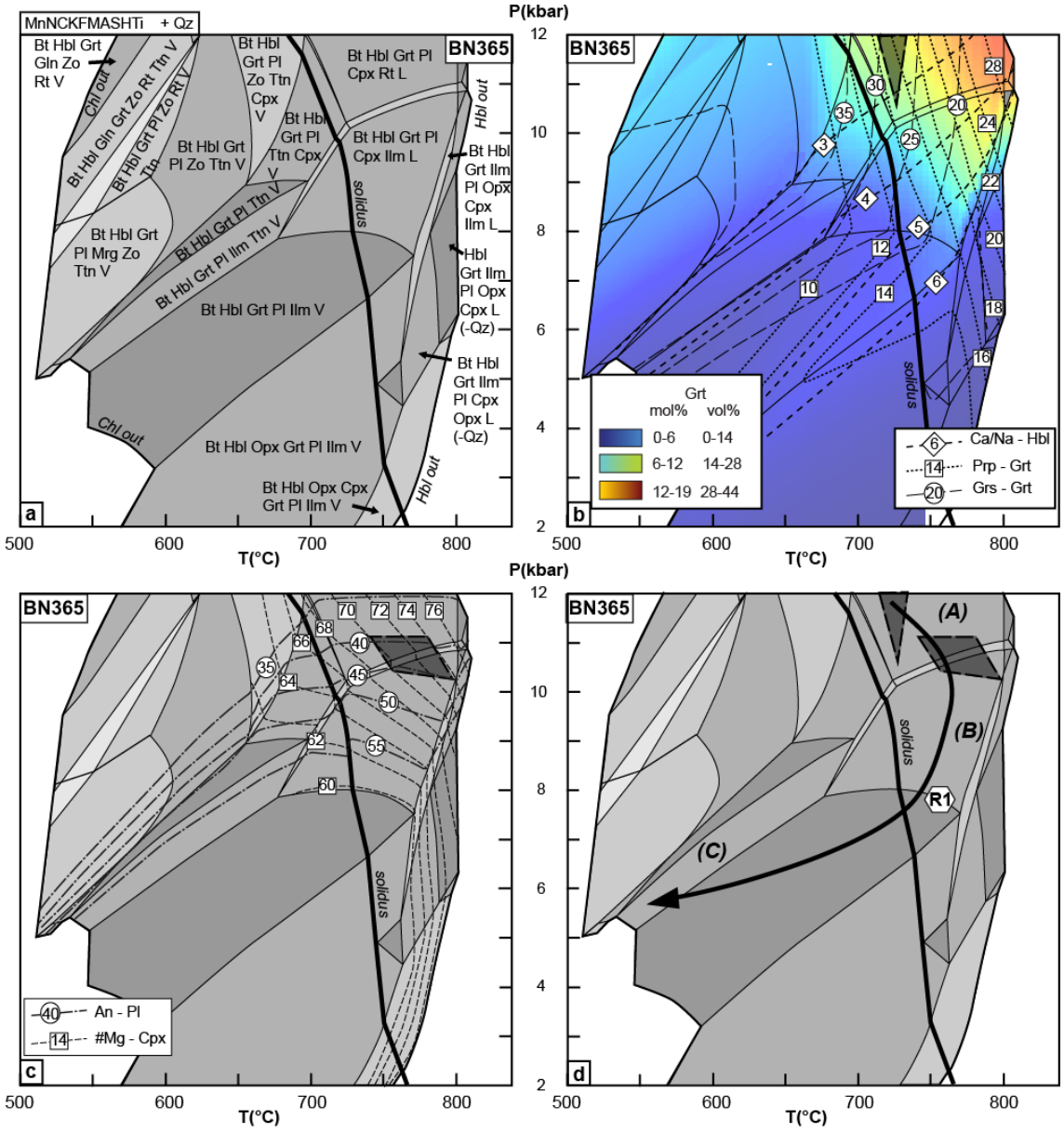

Fig. S2. *MnNCKFMASHT P–T pseudosections illustrating phase equilbria for amphibolite sample BN365. (a) Calculated stable assemblages. (b) Calculated Grt Prp and Grs content, and Ca/Na ratio in Hbl (black dotted lines, numbers in boxes, dashed lines, numbers in circles, and bold dashed lines, numbers in diamonds respectively) and Grt mode. The shaded domain is defined by the intersection of calculated Grt isopleths fitting measured compositions. (c) Calculated Pl An composition and Cpx #Mg (bold dashed and dotted line, number in circles; and dashed line, number in boxes, respectively). The shaded domain represents the intersection of calculated Pl and Cpx isopleths matching measured compositions. (d) (A-C) and (R1) refer to metamorphic assemblages identified in Appendix S1. A P–T path consistent with observations is drawn.*

APPENDIX S2: PSEUDOSECTION CALCULATIONS

Pseudosections were constructed using the Perple_X software (Connolly, 2005) updated in 2013 to version 6.6.8, and using the hp04 thermodynamic database of Holland & Powell (1998) updated in 2004. The solution models used for the pseudosection calculations are as follows : Bio(TCC) for biotite (Tajčmanová *et al.*, 2009), Chl(HP) for chlorite (Holland *et al.*, 1998), St(HP) for staurolite (Holland & Powell, 1998), Ctd(HP) for chloritoid (Holland & Powell, 1998), Amph(DPW) for hornblende (Dale *et al.*, 2005), oAmph(DP) for gedrite (Diener *et al.*, 2007), Gt(WPH) for garnet (White *et al.*, 2000), Ilm(WPH) for ilmenite (White *et al.*, 2000), hCrd for cordierite, Mica(CHA1) for titanium-bearing white mica (Coggon & Holland, 2002, Auzanneau *et al.*, 2010), Mica(M) for white mica in the muscovite-paragonite-margarite system (Massonne & Willner, 2008), melt(HP) (Holland & Powell, 1998, White et al., 2001), Pl(h) for plagioclase feldspar (Newton *et al.*, 1981), Kf/San for low/highT potassic feldspar (Waldbaum & Thompson, 1968), Opx(HP) for orthopyroxene (Holland & Powell, 1998), Omph(GHP2) for clinopyroxene (Green *et al.*, 2007; Diener & Powell, 2012), Act(M) for actinolite (Massonne & Willner, 2008). Pseudosections were built by using the whole rock composition obtained by XRF analysis for rocks displaying homogeneous mineralogy and modal compositions at sample scale. In the case of heterogeneous samples displaying large porphyroblasts or a compositional layering, whole rock compositions were recalculated based on average mineral compositions and modal proportions established by SEM mapping or image processing techniques. Ferric iron was approximated to 0 for all samples, based on results of T-XFe^3 pseudosections that failed to reproduce observed mineral assemblages for positive XFe^3 values. Ca concentration was corrected for apatite and carbonates when they are present in significant amounts.

BN43 & BN534

Sample BN43 and BN534 are migmatites concerned by melt loss and open-system behaviour. Their metamorphic *P–T* evolution was modelled by the complementary use of different pseudosections (White & Powell, 2002; Johnson *et al.*, 2008). The prograde evolution was investigated by constructing a *P–T* pseudosection in the MnNCKFMASHTi system using the average of 21 whole rock compositions of subsolidus metagreywacke samples from the study area obtained by XRF (e.g. Johnson & Brown, 2004; Table 2). H_2O content was constrained so that saturation conditions were met on the wet solidus at 10 kbar, which corresponds to about 1.15 wt%. Pseudosections built with the whole rock composition of the migmatite sample allowed to investigate the peak and post-peak metamorphic evolution. We suppose that the hand sample composition is valid to model phase relationships after hypothetical melt loss. Garnet core fractionation was ignored because it was found to have negligible effects, due to its minor modal proportion.

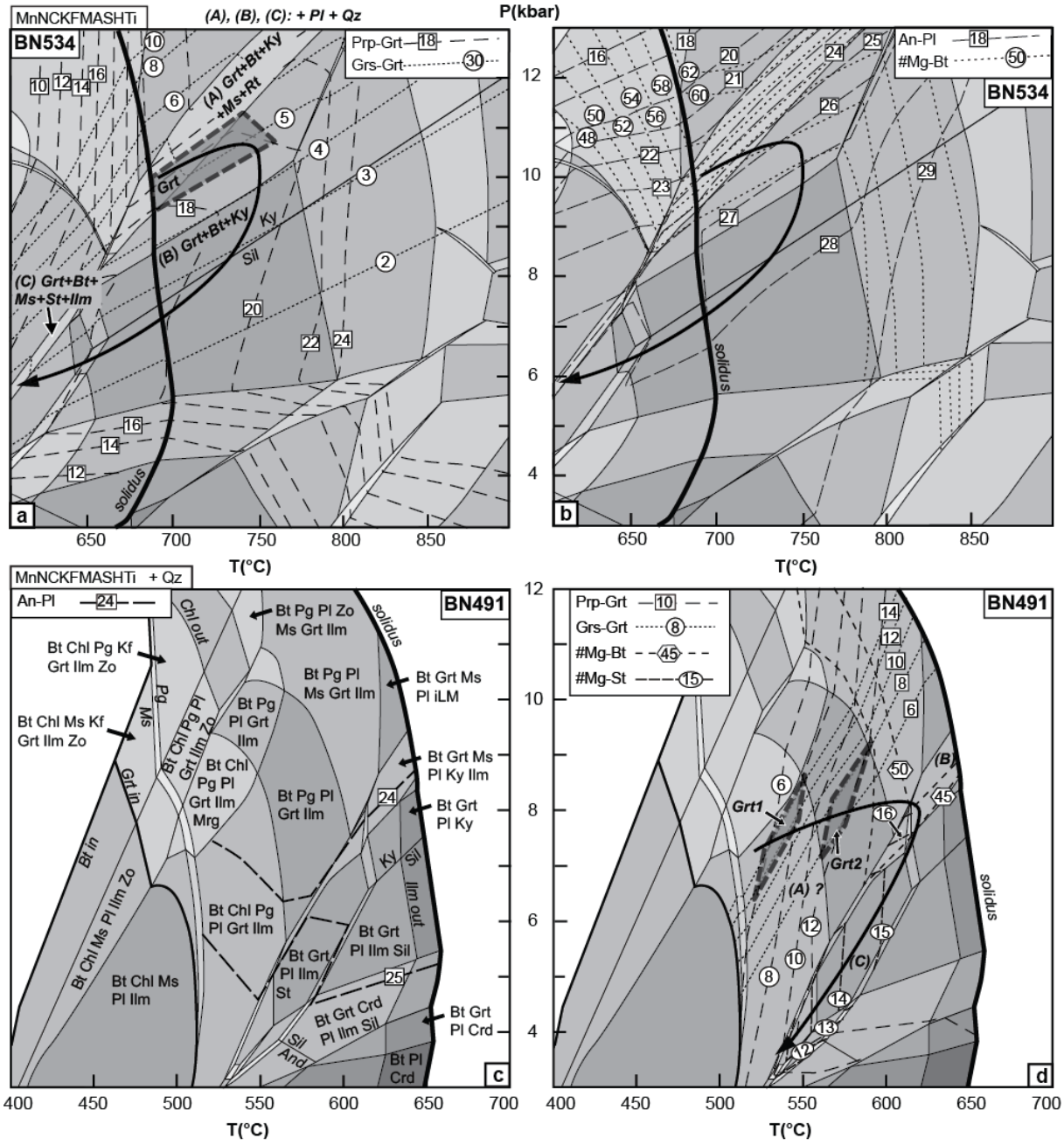

Fig. S3. *(a, b) MnNCKFMASHT P–T pseudosection calculated using the average paragneiss composition (similar to Fig. 7) used to determine the metamorphic evolution of migmatite sample BN534. (a) Calculated Grt Prp and Grs content (black dashed lines, numbers in boxes and dotted lines, numbers in circles, respectively). The shaded area is defined by the intersection of calculated Grt isopleths matching measured compositions. (b) Calculated Pl An content (similar to Fig. 7, dashed lines, numbers in boxes), and Bt #Mg (using the sample whole rock composition, dotted lines, numbers in circles). A-C refers to assemblages identified in Appendix S1, and a possible P–T path is shown. (c, d) MnNCKFMASHT pseudosections illustrating phase equilbria for paragneiss sample BN491. (c) Calculated stable assemblage and Pl isopleths matching measured Pl compositions. (d) Calculated garnet Prp (numbers in boxes) and Grs content (numbers in circles), along with the #Mg of Bt (numbers in diamonds) and St (numbers in ellipses). (A-C) indicates assemblages identified in Appendix S1, and a possible P–T path is shown.*

BN47 & BN491

P–T pseudosections were built in the MnNCKFMASHTi system. Because of the compositional layering inherited from the sedimentary protolith, large staurolite and kyanite porphyroblasts are distributed heterogeneously. The bulk rock chemistry used for modelling was recalculated to take into account local chemical heterogeneities, by evaluating the modal composition of the sample thin section. The isopleth intersect method was used to constrain the conditions of garnet growth, by comparing measured and calculated compositions. Chemically distinct cores represent small (max. 1 vol%) of the rock. Because of this low proportion, garnet fractionation was found to have insignificant effects.

BN436

Garnet fractionation was integrated to model the metamorphic evolution of sample BN436 (Marmo *et al.*, 2002; Evans, 2004). A first pseudosection was built with the whole rock composition obtained by XRF to model prograde evolution in the MnNCKFMASHTi system. A second pseudosection, suitable to interpret peak and post-peak *P–T* conditions, was constructed in the NCKFMASHTi system by fractionating garnet core. Ferric iron content was set to 0 based on results of T –XFe^3 pseudosections: observed assemblages were successfully modelled for $XFe^3 = 0$. As a consequence, epidote group minerals are represented by zoisite (Zo) in the P-T pseudosections.

BN365

Leucosomes in sampe BN365 represent small volumes and are not connected, suggesting that the rock experienced limited melt loss. Consequently, the pseudosection was constructed using the whole rock composition of the sample and H_2O was constrained to be saturated on the solidus at 10 kbar (i.e. 1.5 wt%).

APPENDIX S3: MULTI-EQUILIBRIA CALCULATIONS

Quartz-chlorite-phengite-H_2O thermobarometre

Multi-equilibria calculations were performed with Matlab© on the Chorite-Phengite-Quartz-H_2O assemblage, following a procedure detailed in Ganne *et al.* (2012). Multi-equilibria calculations were performed using the latest thermodynamic model for phengite (Dubacq *et al.*, 2010), which takes into account the T-dependent interlayer water content of dioctahedral mica. Calculations were carried out using the thermodynamic data of five chlorite and six phengite end-members. These end-members are Fe amesite (FeAm: $Si_2Al_4(Fe)_4O_{10}(OH)_8$), Mg amesite (MgAm: $Si_2Al_4(Mg)_4O_{10}(OH)_8$), clinochlore (Clin: $Si_3Al_2Mg_5O_{10}(OH)_8$), daphnite (Daph: $Si_3Al_2Fe_5O_{10}(OH)_8$) and sudoite (Sud:

$Si_3Al_4(Mg,Fe)_2O_{10}(OH)_8$ for chlorite; and muscovite (Ms: $Si_3Al_3KO_{10}(OH)_2$), pyrophyllite (Prl: $Si_4Al_2O_{10}(OH)_2$), hydrated pyrophyllite (Prl.H: $Si_4Al_2O_{10}(OH)_2.H_2O$), Fe celadonite (FeCel: $Si_4Al(Fe)KO_{10}(OH)_2$), Mg celadonite (MgCel: $Si_4Al(Mg)KO_{10}(OH)_2$) and phlogopite (Phl: $Si_3AlMg_3KO_{10}(OH)_2$ for phengite. *P–T* equilibrium conditions, as well as the Fe^{3+} content in chlorite and phengite and the water content of phengite were calculated to minimize the sum of the Gibbs free energy $\sum\Delta G^2$ of the following seven independent reactions:

- (1) 1 Sud + 15 Qtz + 10 FeCel + 2 MgAm > 4 Prl + 10 MgCel + 2 Daph

- (2) 6 MgCel + 7 Qtz + 4 FeAm + 4 H2O > 6 FeCel + 3 Sud + 2 Daph

- (3) 5 MgAm + 4 Daph > 5 FeAm + 4 Clin

- (4) 14 Qtz + 5 FeAm + 3 MgAm + 8 H_2O > 4 Daph + 6 Sud

- (5) 2 Sud + 4 Qtz + 4 Daph + 4 Ms > 2 Prl.H + 4 MgCel + 5 FeAm

- (6) 1 Prl + 1 H_2O > 1 Prl.H

- (7) 11 Qtz + 2 Ms + 1 Phl + 2 H_2O > 3 MgCel + 2 Prl

In theory, thermodynamic equilibrium is achieved if $\sqrt{(\sum\Delta G^2/nr)}$ is equal to 0 (nr = number of reactions considered). In practice, however, a deviation from 0 occurs because of analytical uncertainties. Equilibrium is considered to be achieved when $\sqrt{(\sum\Delta G^2/nr)} < 2400$ J. These values account for the analytical uncertainties and they were estimated after Monte Carlo simulations (Vidal *et al.*, 2006).

Quartz-chlorite-H_2O and quartz-phengite-H_2O thermometres

Multi-equilibria calculations were carried out on the Chorite-Quartz-H_2O assemblage, by assuming a water activity equal to unity. A Matlab© script built by Vincent de Andrade and the thermodynamic data of five chlorite end-members (Vidal *et al.*, 2001) was used: Fe amesite (FeAm: $Si_2Al_4(Fe)_4O_{10}(OH)_8$), Mg amesite (MgAm: $Si_2Al_4(Mg)_4O_{10}(OH)_8$), clinochlore (Clin: $Si_3Al_2Mg_5O_{10}(OH)_8$), daphnite (Daph: $Si_3Al_2Fe_5O_{10}(OH)_8$) and sudoite (Sud: $Si_3Al_4(Mg,Fe)_2O_{10}(OH)_8$. With these end members, four independent equilibria are considered.

- (1) 2 Clin + 3 Sud > 4 MgAm + 7 Qtz + 4 H_2O

- (2) 4 Clin + 5 FeAm > 4 Daph + 5 MgAm

- (3) 16 Daph + 15 Sud >20 FeAm + 6 Clin + 35 Qtz + 20 H_2O

- (4) 4 Daph + 6 Sud >5 FeAm + 3 MgAm + 14 Qtz + 8 H_2O

A minimum amount of Fe^{3+} in chlorite was estimated using the stoichiometric criteria given in Vidal *et al.* (2005), and Fe^{3+} content was iteratively modified to minimize $\sum\Delta G^2$ (Vidal *et al.,* 2006). Parra *et al.* (2002) calibrated a model for the phengite-quartz equilibrium, calculated from activities of chosen end-members, taking into account the non-ideal term of activity coefficients. Dubacq *et al.* (2010) extended this model to smectite, illite, interlayered smectite-illite and mica by considering the T–hydration relationship, pressure and the rock composition, using multi-equilibrium thermobarometry.

The model involves nine end-members: Muscovite (Ms: $Si_3Al_3KO_{10}(OH)_2$), Paragonite (Pg: $Na(Al_2)(Si_3Al)O_{10}(OH)_2$), Mg-celadonite (MgCel: $Si_4Al(Mg)KO_{10}(OH)_2$), Fe-celadonite (Fe-Cel: $Si_4Al(Fe)KO_{10}(OH)_2$), Phlogopite (Phl: $Si_3AlMg_3KO_{10}(OH)_2$), Annite (Ann: $K(Fe_3)(Si_2Al)O_{10}(OH)_2$), Pyrophyllite (Prl: $Si_4Al_2O_{10}(OH)_2$), hydrated Pyrophyllite (Prl.H_2O: $Si_4Al_2O_{10}(OH)_2.H_2O$) and Margarite (Mrg: $CaAl_2(Al_2Si_2)O_{10}(OH)_2$). Three independent equilibria - and their hydrated derivatives - can be written for the Phg-Qtz-water assemblage.

- (5) 3 MgCel.mH_2O + 2 Prl.$(m+1)H_2O$ >2 Musc.mH_2O + Phl.mH_2O + 11Qtz + $(2m+4)H_2O$

- (6) 3 FeCel.mH_2O + 2 Prl.$(m+1)H_2O$ > 2 Musc.mH_2O + Ann.mH_2O + 11Qz + $(2m+4)H_2O$

- (7) Prl.$(m+1)H_2O$nw > Prl.$(m'+1)$H2Onw + $(m-m')H_2O$

where (m+1) and (m'+1) are the maximum and minimum amount of water, with m and m' varying from 0 to 6 and 0 to 3 according to the water layers content (noted nw). Fe^{3+} is not taken into account by the model. The hydration state is modified iteratively to minimize $\sum\Delta G^2$. Calculations are carried out with Matlab© software using a script build by Benoit Dubacq.

The Quartz-Chlorite-Phengite-H_2O thermobarometre provided satisfactory results for sample BN185. 646 × 441 Ph/Chl microprobe point analyses were first filtered on the basis of the compositional criteria (Vidal & Parra, 2000). Calculations of *P–T* equilibrium conditions eventually involved 198 × 162 Ph/Chl analyses. Calculations for samples BN246 failed to fulfill strict equilibrium criteria by using the Quartz-Chlorite-Phengite-H_2O thermobarometre. *P–T* conditions were investigated independently by coupling the Quartz-Chlorite-H_2O and Quartz-Phengite-H_2O thermometres. Multi-equilibria calculations involved 19 chlorite analyses and 47 phengite analyses for sample BN246.

Table S2. (See attached .xls file). Composition and structural formulae of chlorite and white mica used for multi-equilibria calculations.

APPENDIX S4: U-PB DATING

SHRIMP II analytical techniques

Selected monazite crystals as small as 10 µm from samples BN43 and BN47 were dated using Sensitivity High Resolution Ion Microprobe (SHRIMP II). The selected crystals were cut it into 3 mm discs out from polished thin sections, and were later casted into an a 25mm epoxy disc and prepared for SHRIMP analysis as described by Rasmussen *et al.* (2010). Analytical conditions and procedures are given in Foster *et al.* (2000) and Rasmussen *et al.* (2001). Internal calibration was done using the standards GM3, IND and VK 1 (Rasmussen *et al.* 2002; Kennedy & Kinny, 2004; Schmitz *et al.*, 2009; Fletcher *et al.,* 2010; Ruschel *et al.,* 2012; Wingate & Kirkland, 2013).

LA-ICP-MS analytical techniques

Uranium, thorium and lead isotopes were analyzed using a ThermoScientific Element 2 sector field ICP-MS coupled to a Resolution M-50 (Resonetics) 193 nm ArF excimer laser (ComPexPro 102F, Coherent) system, using the procedures described by Gerdes & Zeh (2006, 2009) with modifications explained in Zeh & Gerdes (2012). During this study the unknown monazite grains were analysed together with the standard zircon GJ-1 (Jackson *et al.*, 2004), and with the standard monazites Moacir (Gasquet *et al.*, 2010) and Manangotry (Horstwood *et al.,* 2003). Most monazite grains (unknowns and standards) were ablated with a laser spot-size of 19 µm diameter, but for high-U monazite, a smaller spot size of 12 µm have been employed. Ablation was done with a repetition rate of 4 Hz, and ca. 2 J cm^{-2} laser energy. Particle transport was performed in a 0.63 l min^{-1} He stream, which was mixed directly after the ablation cell with 0.02 l min^{-1} N_2 and 0.83 l min^{-1} Ar prior to introduction into the Ar plasma of the SF-ICP-MS. Signal was tuned for maximum sensitivity for Pb and U while keeping oxide production, monitored as $^{254}UO/^{238}U$, below 0.2%. The sensitivity achieved was in the range of ca. 12900 cps/µg g^{-1} for ^{238}U with a 33 µm spot size, at 5.0 Hz and 5 J cm^{-2} laser energy (obtained on the standard zircon GJ1). Sample surfaces were cleaned directly before each analysis by three pulses pre-ablation. Raw data were corrected offline for background signal, common Pb, laser induced elemental fractionation, instrumental mass discrimination, and time-dependent elemental fractionation of Pb/U using an in-house MS Excel© spreadsheet program (Gerdes & Zeh, 2006, 2009). The common-Pb correction was carried out when the common-Pb uncorrected $^{207}Pb/^{206}Pb$ was significantly higher than the corrected $^{207}Pb/^{206}Pb$. For most analyses the common Pb level (quoted here as ^{206}Pb common of total ^{206}Pb) was below 0.2% (see Table 5). Common-Pb correction was carried out by using the $^{202,204}Hg$ interference- and background-corrected ^{204}Pb signal, and a model Pb composition (Stacey & Kramers, 1975). The interference of ^{204}Hg (ca. 250 cps; counts per second, during our sessions) on mass 204 was estimated using a $^{204}Hg/^{202}Hg$ ratio of 0.2299 and the measured ^{202}Hg. Laser induced elemental fractionation and instrumental mass discrimination were corrected by

normalization to the reference zircon GJ-1 (primary standard). Potential matrix effects were controlled by multiple measurements of the standard monazites Moacir and Managotry (secondary standards). Prior to the normalization, the drift in inter-elemental fractionation (Pb/U) during 21s of sample ablation was corrected for the individual analysis. The correction was done by applying a linear regression through all measured ratios, excluding the outliers (±2σ standard deviation; 2 SD), and using the intercept with the y-axis as the initial ratio (=intercept method). The total offset of the measured drift-corrected $^{206}Pb/^{238}U$ ratio from the"true" ID-TIMS value (0.0982±0.0004; ID-TIMS GUF-value) of the analyzed GJ-1 grain was about 11%. Reported uncertainties (2σ) of the $^{206}Pb/^{238}U$ ratio were propagated by quadratic addition of the external reproducibility (2 SD %) obtained from standard GJ-1 (n=11; 2 SD~1.23%) during the analytical session, and the within-run precision of each analysis (2 SE %; standard error). Reproducibility of the $^{207}Pb/^{206}Pb$ ratio depends strongly on counting statistic (see Gerdes & Zeh, 2009), as well as on the common-Pb content. To account for both, the uncertainty on $^{207}Pb/^{206}Pb$ signal were propagated by quadratic addition of the outlier corrected $^{207}Pb/^{206}Pb$ within-run precision (2 SE%), a ^{207}Pb signal dependent factor, and an factor which takes the amount of common-Pb, and the uncertainties of model Pb composition into account (Gerdes & Zeh, 2009). The $^{207}Pb/^{235}U$ ratio is derived from the normalized and error propagated $^{207}Pb/^{206}Pb$ and $^{206}Pb/^{238}U$ ratios, assuming a $^{238}U/^{235}U$ natural abundance ratio of 137.88 and the uncertainties of both ratios. The standard zircon GJ1 (n=11) measured during this study yield a Concordia ages of 604.1 ± 2.7 Ma (n=11, MSWD=0.55, Probability of fit = 0.95). Multiple measurements of the standard monazite Moacir yield a Concordia age of 500.7 ± 2.5 (n=11, MSWD=1.4, Probability of fit = 0.12) and of the standard monazite Manangotry a Concordia age of 552.3 ± 2.8 (n=11, MSWD=1.18, Probability of fit = 0.26) which are within error of published data (Horstwood *et al.*, 2003; Gasquet *et al.*, 2010). The data were plotted using the software ISOPLOT (Ludwig, 2001).

Results of U-Pb SHRIMP dating of monazite carried out at JLC, Perth

analysis	grain n°	location	U (ppm)	Th (ppm)	Th/U	$^{206}Pb^{a}$ / ^{238}U	±2s (%)	$^{207}Pb^{a}$ / ^{235}U	±2s (%)	$^{207}Pb^{a}$ / ^{206}Pb	±2s (%)	rho[b]	$^{206}Pb^{c}$ / ^{238}U	±2s (Ma)	^{207}Pb / ^{235}U	±2s (Ma)	$^{207}Pb^{c}$ / ^{206}Pb	±2s (Ma)	conc.[d] (%)
BN43																			
BN43D-4.1	4	leucosome	3429	22288	6.50	0.40	2.73	7.39	2.78	0.1334	0.52	0.98	2186	51	2159	25	2130	10	103
BN43D-5.1	5	bt selvedge	1750	28319	16.2	0.40	2.18	7.25	2.28	0.1331	0.67	0.95	2151	40	2142	20	2130	12	101
BN43D-6.1	6	leucosome	3350	11308	3.38	0.39	3.62	7.16	3.69	0.1325	0.74	0.98	2134	66	2131	32	2125	13	100
BN43D-6.2	6		4639	19138	4.13	0.40	2.82	7.33	2.85	0.1329	0.40	0.99	2169	52	2152	25	2132	7	102
BN43D-8A.1	8	leucosome	5299	23468	4.43	0.42	3.26	7.65	3.29	0.1337	0.41	0.99	2246	62	2191	29	2136	8	105
BN43D-8A.2	8	leucosome	7651	24518	3.20	0.43	2.61	7.92	3.56	0.1585	1.59	0.73	2326	51	2222	32	2124	42	110
BN43D-1.1	1	elongated in matrix	1666	26462	15.9	0.368	3.61	6.72	3.68	0.1333	0.67	0.98	2020	63	2076	32	2128	13	95
BN43D-1.2	1		1705	17983	10.5	0.340	3.58	6.24	5.43	0.1460	2.06	0.66	1887	59	2010	46	2135	71	88
BN43D-1.3	1		3327	17870	5.37	0.399	3.33	7.34	3.36	0.1334	0.46	0.99	2165	61	2154	30	2139	8	101
BN43D-10.1	10	bt selvedge	1255	39290	31.3	0.369	3.46	6.78	3.57	0.1336	0.86	0.97	2027	60	2083	31	2136	15	95
BN43D-22.1	22	bt selvedge	2679	11065	4.13	0.327	3.78	6.07	4.34	0.1383	1.60	0.87	1823	60	1986	37	2155	37	85
BN43D-26.1	26	matrix	1127	25646	22.8	0.398	3.47	7.39	3.57	0.1347	0.84	0.97	2162	64	2160	31	2154	15	100
BN43D-23.1	23	leucosome	3386	19158	5.66	0.402	3.33	7.34	3.37	0.1327	0.49	0.99	2178	62	2154	30	2127	9	102
BN43D-23.2	23	grt incl.	5193	21958	4.23	0.401	3.31	7.37	3.39	0.1333	0.74	0.98	2173	61	2157	30	2139	13	102
BN43D-23.3	23	grt incl.	2607	14741	5.66	0.393	3.38	7.25	3.46	0.1351	0.64	0.98	2139	62	2142	30	2142	13	100
BN43D-23.4	23	grt incl.	4025	16965	4.21	0.391	3.33	7.19	3.37	0.1339	0.48	0.99	2127	60	2135	30	2138	9	99
BN43D-11.1	11	bt selvedge	2324	27279	11.7	0.405	3.36	7.43	3.53	0.1336	1.06	0.95	2192	62	2164	31	2134	19	103
BN47																			
BN47-11.1	11	ky incl.	7568	29430	3.89	0.479	1.87	8.7	2.51	0.1337	0.84	0.75	2522	39	2304	23	2113	29	119
BN47-11.2	11	ky incl.	5358	27289	5.09	0.46	1.70	8.4	1.93	0.1329	0.86	0.88	2442	35	2270	17	2115	16	115
BN47-13.1	13	ky incl.	5225	19233	3.68	0.43	2.30	7.8	2.42	0.1321	0.74	0.95	2300	45	2208	22	2120	13	109
BN47-12.1	12	matrix	4399	21482	4.88	0.41	2.93	7.5	2.97	0.1320	0.44	0.99	2214	55	2167	26	2120	8	104
BN47-15.1	15	matrix	4923	24931	5.06	0.43	2.06	7.9	2.11	0.1340	0.42	0.97	2324	40	2224	19	2131	8	109
BN47-16.1	16	ky incl.	5479	20923	3.82	0.42	2.78	7.7	2.80	0.1325	0.38	0.99	2270	53	2197	25	2126	7	107
BN47-18.1	18	matrix	4969	22770	4.58	0.41	2.50	7.5	2.53	0.1325	0.40	0.99	2224	47	2175	22	2125	7	105
BN47-19.1	19	matrix	4635	22434	4.84	0.42	2.71	7.6	2.75	0.1326	0.42	0.99	2240	51	2182	24	2125	8	105
BN47-20.1	20	ky incl.	5733	27273	4.76	0.35	2.06	6.5	2.36	0.1369	0.71	0.87	1954	35	2040	21	2123	20	92
BN47-13.2	13	ky incl.	5036	20949	4.16	0.43	2.41	7.7	2.46	0.1330	0.44	0.98	2284	46	2202	22	2123	9	108
BN47-22.1	22	matrix bt	4603	22979	4.99	0.38	2.07	7.0	2.15	0.132	0.59	0.96	2098	37	2113	19	2124	10	99
BN47-24.1	24	matrix bt	3998	19788	4.95	0.389	2.13	7.1	2.16	0.133	0.38	0.98	2120	38	2130	19	2136	7	99
BN47-27.1	27	matrix bt	4504	21622	4.80	0.392	2.23	7.2	2.86	0.146	0.93	0.78	2132	40	2140	25	2143	31	99
BN47-29.1	29	matrix bt	4615	24236	5.25	0.392	1.49	7.2	1.53	0.132	0.38	0.97	2134	27	2133	14	2128	7	100
BN47-31.1	31	matrix	4976	26326	5.29	0.395	2.10	7.2	2.13	0.132	0.37	0.98	2147	38	2136	19	2121	7	101
BN47-26.1	26	matrix	2699	14999	5.56	0.329	1.18	6.0	1.60	0.135	0.96	0.74	1835	19	1979	14	2130	19	86
BN47-23.1	23	matrix	5589	28839	5.16	0.399	2.36	7.3	2.38	0.133	0.32	0.99	2164	43	2147	21	2127	6	102
BN47-28.1	28	matrix	6362	28692	4.51	0.396	1.55	7.2	1.59	0.132	0.31	0.98	2151	28	2139	14	2123	5	101

Errors are 2-sigma; Pb_c and Pb^* indicate the common and radiogenic portions, respectively.

Error in Standard calibration was 0.39% (not included in above errors but required when comparing data from different mounts).

[a] corrected for background

[b] rho is the $^{206}Pb/^{238}U/^{207}Pb/^{235}U$ error correlation coefficient.

[c] Common Pb corrected using measured ^{204}Pb.

[d] degree of concordance = $^{206}Pb/^{238}U$ age / $^{207}Pb/^{206}Pb$ age x 100

Table S3. *U–Pb isotopic data obtained by SHRIMP at JLC in Perth, Australia.*

REFERENCES

Auzanneaun, E., Schmidt, M.W., Vielzeuf, D. & Connolly, J.A.D., 2010. Titanium in phengite: a geobarometer for high temperature eclogites. *Contributions to Mineralogy and Petrology*, **159**, 1-24.

Coggon, R. & Holland, T.J.B., 2002. Mixing properties of phengitic micas and revised garnet-phengite thermobarometers. *Journal of Metamorphic Geology*, **20**, 683-96.

Connolly, J. A. D., 2005. Computation of phase equilibria by linear programming : A tool for geodynamic modeling and its application to subduction zone decarbonation. *Earth and Planetary Science Letters*, **236**, 524-541.

Dale, J., Powell, R., White, R.W., Elmer, F.L. & Holland, T.J.B. 2005. A thermodynamic model for Ca-Na clinoamphiboles in Na_2O-CaO-FeO-MgO-Al_2O_3-SiO_2-H_2O-O for petrological calculations. *Journal of Metamorphic Geology*, **23**, 771-91.

Diener, J. F. A., & Powell, R., 2012. Revised activity–composition models for clinopyroxene and amphibole. *Journal of Metamorphic Geology*, **30**, 2, 131-142.

Diener, J. F. A., Powell, R., White, R. W. & Holland, T. J. B., 2007. A new thermodynamic model for clino-and orthoamphiboles in the system Na_2O–CaO–FeO–MgO–Al_2O_3–SiO_2–H_2O–O. *Journal of Metamorphic Geology*, **25**, 6, 631-656.

Dubacq, B., Vidal, O. & De Andrade, V., 2010. Dehydration of dioctahedral aluminous phyllosilicates:thermodynamic modelling and implications for thermobarometric estimates. *Contributions to Mineralogy and Petrology*, **159**,159–174.

Evans, T. P., 2004. A method for calculating effective bulk composition modification due to crystal fractionation in garnetbearing schist: implications for isopleth thermobarometry. *Journal of Metamorphic Geology*, **22**, 547–557.

Fletcher, I. R., McNaughton, N. J., Davis, W. J. & Rasmussen, B., 2010, Matrix effects and calibration limitations in ion probe U–Pb and Th–Pb dating of monazite. *Chemical Geology*, **270**, 31-44.

Foster, G., Kinny, P., Vance, D., Prince, C. & Harris, N., 2000, The significance of monazite U-Th-Pb age data in metamorphic assemblages; a combined study of monazite and garnet chronometry. *Earth and Planetary Science Letters*, **181**, 327-340.

Ganne, J., De Andrade, V., Weinberg, R., Dubacq, B., Vidal, O. and Kagambega, N., Naba, S., Baratoux, L., Jessell, M. & Allibon, J., 2012. Modern-style plate subduction preserved in the Palaeoproterozoic West African Craton : *Nature Geoscience*, **5**, 60-65.

Gasquet, D., Bertrand, J. M., Paquette, J. L., Lehmann, J., Ratzov, G., Guedes, R. D. A. & Nomade, S., 2010. Miocene to Messinian deformation and hydrothermal activity in a pre-Alpine basement massif of the French western Alps: new U-Th-Pb and argon ages from the Lauzière massif. *Bulletin de la Société Géologique de France*, **181**, 227-241.

Green, E., Holland, T. & Powell, R., 2007. An order-disorder model for omphacitic pyroxenes in the system jadeite-diopside-hedenbergite-acmite, with applications to eclogitic rocks. *American Mineralogist*, **92**, 1181-1189.

Gerdes, A. & Zeh, A., 2009. Zircon formation versus zircon alteration—new insights from combined U–Pb and Lu–Hf in-situ LA-ICP-MS analyses, and consequences for the interpretation of Archean zircon from the Central Zone of the Limpopo Belt. *Chemical Geology*, **261**, 230-243.

Gerdes, A. & Zeh, A., 2006. Combined U–Pb and Hf isotope LA-(MC-) ICP-MS analyses of detrital zircons: comparison with SHRIMP and new constraints for the provenance and age of an Armorican metasediment in Central Germany. *Earth and Planetary Science Letters*, **249**, 47-61.

Holland, T. J. B. & Powell, R., 1998. An internally consistent thermodynamic data set for phases of petrological interest. *Journal of Metamorphic Geology*, **16**, 309-343.

Holland, T., Baker, J. & Powell, R., 1998. Mixing properties and activity-composition relationships of chlorites in the system MgO-FeO-Al_2O_3-SiO_2-H_2O. *European Journal of Mineralogy*, **10**, 395-406.

Horstwood, M. S., Foster, G. L., Parrish, R. R., Noble, S. R. & Nowell, G. M., 2003. Common-Pb corrected in situ U–Pb accessory mineral geochronology by LA-MC-ICP-MS. *Journal of Analytical Atomic Spectrometry*, **18**, 837-846.

Jackson, S. E., Pearson, N. J., Griffin, W. L. & Belousova, E. A., 2004. The application of laser ablation-inductively coupled plasma-mass spectrometry to in situ U–Pb zircon geochronology. *Chemical Geology*, **211**, 47-69.

Johnson, T. E., White, R. W. & Powell, R., 2008. Partial melting of metagreywacke: a calculated mineral equilibria study. *Journal of Metamorphic Geology*, **26**, 8, 837-853.

Johnson, T. & Brown, M., 2004. Quantitative Constraints on Metamorphism in the Variscides of Southern Brittany – a Complementary Pseudosection Approach. *Journal of Petrology*, **45**, 6. 1237-1259.

Kennedy, A. & Kinny, P. D., 2004 Identifying inter- and intra-laboratory SIMS monazite standards. SHRIMP workshop, Hiroshima, Japan, 11–14.

Ludwig, K.R., 2001. Isoplot/Ex, rev. 2.49: a geochronological toolkit for Microsoft Excel. *Berkeley Geochronology Center, Special Publication*, **4**, 55 p.

Marmo, B.A., Clarke, G.L. & Powell, R., 2002. Fractionation of bulk rock composition due to porphyroblast growth : effects on eclogite facies mineral equilibria, Pam Peninsula, New Caledonia. *Journal of Metamorphic Geology*, **20**, 151-165.

Massonne, H. J. & Willner, A. P., 2008. Phase relations and dehydration behaviour of psammopelite and mid-ocean ridge basalt at very-low-grade to low-grade metamorphic conditions. *European Journal of Mineralogy*, **20**, 867-879.

Parra, T., Vidal, O. & Agard, P., 2002. A Thermodynamic model for Fe-Mg dioctahedral K-white micas using data from phase equilibrium experiments and natural pelitic assemblages. *Contributions to Mineralogy and Petrology*, **143**, 706-732.

Rasmussen, B., Fletcher, I. R. & McNaughton, N. J., 2001, Dating low-grade metamorphic events by SHRIMP U-Pb analysis of monazite in shales. *Geology*, **29,** 963–966.

Rasmussen, B., Bengtson, S., Fletcher, I. R. & McNaughton, N. J., 2002, Discoidal Impressions and Trace-Like Fossils More Than 1200 Million Years Old. *Science*, **296**, 1112-1115.

Rasmussen, B., Fletcher, I. R., Muhling, J. R. & Wilde, S. A., 2010, In situ U–Th–Pb geochronology of monazite and xenotime from the Jack Hills belt: implications for the age of deposition and metamorphism of Hadean zircons. *Precambrian Research*, **180**, 26–46.

Ruschel, K., Nasdala, L., Kronz, A., Hanchar, J., Többens, D. M., Škoda, R., Finger, F. & Möller, A., 2012, A Raman spectroscopic study on the structural disorder of monazite–(Ce). *Mineralogy and Petrology*, **105**, 41-55.

Schmitz, S., Möller, A., Wilke, M., Malzer,W., Kanngiesser, B., Bousquet, R., Berger, A. & Schefer, S., 2009, Chemical U-Th-Pb dating of monazite by 3D-Micro X-ray fluorescence analysis with synchrotron radiation. *European Journal of Mineralogy*, **21**, 927–945.

Stacey, J. S. & Kramers, J.D., 1975. Approximation of terrestrial lead isotope evolution by a two-stage model. *Earth and Planetary Science Letters*, **26**, 207-221

Tajčmanová, L., Connolly, J.A.D. & Cesare, B. 2009. A thermodynamic model for titanium and ferric iron solution in biotite. *Journal of Metamorphic Geology*, **27**, 153-64.

Vidal, O. & Parra, T., 2000. Exhumation paths of high pressure metapelites obtained from local equilibria for chlorite-phengite assemblages. *Geological Journal*, **35**, 139-161.

Vidal, O., DeAndrade, V., Lewin, E., Munoz, M., Parra, T. & Pascarelli, S., 2006. P–T-deformation-Fe^{3+}/Fe^{2+} mapping at the thin section scale and comparison with XANES mapping. Application to a garnet-bearing metapelite from the Sambagawa metamorphic belt (Japan). *Journal of Metamorphic Geology*, **24**, 669–683.

Vidal, O., Parra, T. & Trotet, F., 2001. A thermodynamic model for Fe-Mg aluminous chlorite using data from phase equilibrium experiments and natural pelitic assemblages in the 100-600 °C, 1-25 kbar P-T range. *American Journal of Science*, **301**, 557-592.

Vidal, O., Parra, T. & Vieillard, P., 2005. Thermodynamic properties of the Tschermak solid solution in Fe-chlorite: Application to natural examples and possible role of oxidation. *American Mineralogist*, **90**, 347-358.

Waldbaum, D.R. & Thompson, J.B. 1968. Mixing Properties of Sanidine Crystalline Solutions .2. Calculations Based On Volume Data. *American Mineralogist*, **53.**

White, R. W. & Powell, R., 2002. Melt loss and the preservation of granulite facies mineral assemblages. *Journal of Metamorphic Geology*, **20**, 621–632.

White, R.W, Powell, R. & Holland, T.J.B., 2001. Calculation of partial melting equilibria in the system Na_2O–CaO–K_2O –FeO–MgO–Al_2O_3–SiO_2–H_2O (NCKFMASH). *Journal of Metamorphic Geology*, **19**, 139-153.

White, R.W., Powell, R., Holland, T.J.B. & Worley, B.A., 2000. The effect of TiO_2 and Fe_2O_3 on metapelitic assemblages at greenschist and amphibolite facies conditions: mineral equilibria calculations in the system K_2O-FeO-MgO-Al_2O_3-SiO_2-H_2O-TiO_2-Fe_2O_3. *Journal of Metamorphic Geology*, **18,** 497-511.

Wingate, M.T.D., Kirkland, C. L. & Bodorkos, S., 2010, Introduction to geochronology data released in 2013. *Geological Survey of Western Australia*, Perth.

Zeh, A. & Gerdes, A., 2012. U–Pb and Hf isotope record of detrital zircons from gold-bearing sediments of the Pietersburg Greenstone Belt (South Africa)—Is there a common provenance with the Witwatersrand Basin? *Precambrian Research*, **204**, 46-56.